Transport at Interfaces in Lipid Membranes and Enantiomer Separation

Dissertation zur Erlangung des akademischen Grades
Dr. rer. nat.

eingereicht an der
Mathematisch-Naturwissenschaftlich-Technischen Fakultät
der Universität Augsburg

von
Thomas Fraunholz

Augsburg, Oktober 2014

Erstgutachter	Prof. Dr. R. H. W. Hoppe, Universität Augsburg
Zweitgutachter	Prof. Dr. M. A. Peter, Universität Augsburg

Mündliche Prüfung	4. Dezember 2014

Preface

The title of this thesis corresponds to a project within the priority program 1506, organized and financed by the German Science Foundation, the support of which has made this research possible. Within this project we investigated the dynamics and formation of differently ordered phases in lipid layers, as well as the separation of chiral objects. This thesis is therefore separated into two parts, presenting results of research in these two fields of interest developed under my participation.

My special thanks go to Prof. Dr. Ronald H. W. Hoppe and Prof. Dr. Malte Peter for their constant support and encouragement in research. I was in the rare and fortunate position of having two advisors giving me help and guidance including discussions and beneficial hints. Not least, I thank them for proof-reading this dissertation. In particular, I want to thank Prof. Dr. Ronald H. W. Hoppe for introducing me to the field of adaptive finite elements and PDE constrained optimization. I am utterly grateful for all this.

Further, I say thanks to our cooperation partners at the chair of Experimental Physics I, namely Prof. Dr. Achim Wixforth, Dr. Thomas Franke (now at the University of Glasgow) and Stefan Burger for the long and fruitful interdisciplinary discussions.

In addition to this I want to thank Prof. Dr. Dietrich Braess for our joint work in the field of adaptive finite elements not reported here.

I thank my collegues at the Institute of Mathematics, who directly or indirectly contributed to the realization of this thesis and in particular to my office mate Dr. Christopher Linsenmann for the kind and pleasant atmosphere.

Last but not least I want to express my deepest gratitude to my beloved Michaela for always standing by my side over all the years.

Augsburg, October 2014 Thomas Fraunholz

Notation

For standard notation concerning Lebesgue and Sobolev space theory we refer to [Tar07]. Additional notations and definitions are given in place whenever possible for convenience. However, the inner product and norm on $L^2(\Omega)$ are denoted by $(\cdot,\cdot)_{0,\Omega}$ and $\|\cdot\|_{0,\Omega}$, respectively. We further refer to $H_0^k(\Omega)$ as the closure of $C_0^\infty(\Omega)$ with respect to the topology induced by $\|\cdot\|_{k,\Omega}$. In general $H^k(\Omega)$, $k \in \mathbb{N}$, denotes the Sobolev space equipped with the norm $\|\cdot\|_{k,\Omega}$ and the seminorm $|\cdot|_{k,\Omega}$.

We use different notations for scalar valued variables or functions and operators mapping into scalar valued spaces, sets or spaces consisting of such objects, and their vector- or matrix-valued counterparts which are denoted by bold symbols. Consequently, we write $A \in \mathbb{R}$, but $\boldsymbol{A} \in \mathbb{R}^{2\times 2}$. However, we treat multidimensional spatial coordinates as scalar variables by habit, i.e. $x \in \Omega$ with $\Omega \subset \mathbb{R}^2$. As an exception to the general rule, we use the non-bolded ∇-operator which actually returns vector- and matrix-valued results applied to multidimensional objects.

Besides the Euclidean product $(\cdot,\cdot)_2$ for vector-valued objects and the induced Euclidean norm $\|\cdot\|_2$, we further use the generalized inner product for matrix-valued variables $\boldsymbol{A}, \boldsymbol{B} \in \mathbb{R}^{n\times n}$ which is defined by $\boldsymbol{A} : \boldsymbol{B} = \sum_{ij} A_{ij} B_{ij}$. In case of vector-valued variables the generalized product equals the standard vector product, such that for $\boldsymbol{a}, \boldsymbol{b} \in \mathbb{R}^n$ there holds $\boldsymbol{a} : \boldsymbol{b} = (\boldsymbol{a}, \boldsymbol{b})_2$.

In addition to this we denote the equality of A and B up to terms of certain order by $A \simeq B$. When we give the value A up to certain precision as numerical value B, we write $A \approx B$. We further write $A \lesssim B$, if there exists a constant $C > 0$ not depending on a given triangulation such that $A \leq CB$.

Finally, physical constants, parameters and quantities are given in SI units, referred to by its French name *système international d'unités*. The system was originally introduced by the *Académie des sciences* at the end of the 18th century in Paris.

Contents

List of Figures

List of Tables

Part I

Phase Separation in Lipid Membranes

Chapter 1

Introduction

We address phenomena of phase separation in lipid membranes in this first part. The problem is investigated using a C^0-Interior Penalty Discontinuous Galerkin (C^0-IPDG) formulation of the Cahn–Hilliard equation. In this context we provide a residual-type a posteriori error estimator for the biharmonic problem including convergence analysis. Subsequently we will introduce our field of research in section 1.1 of this first chapter. In section 1.2, we present biophysical properties of phase separation in lipid membranes. Finally, in section 1.3, we describe our methods of choice and give an outline of the following chapters.

1.1 Issue and Motivation

We follow our introductory discussions in [BFL$^+$13] to give a short introduction to our topic of research. Phospholipids are built from nutrition by organisms. Their general availability makes them attractive to nature as a key building block of life. When exposed to water, phospholipids spontaneously form double layers. These immediately re-group into vesicles of certain size ($1 - 100$ μm). This dynamic plays an essential role in our life, because vesicles serve organisms as hulls for their eukaryotic cells. Membranes consisting of different lipids are non-trivial systems. This is especially true when we have to take into account interactions with additional components, e.g. cholesterol. Giant Unilamellar Vesicles (GUVs) are simplified systems. Their membrane consists of fewer types of lipids, without loosing characteristic behaviors. In this part we are especially interested in systems built of 1,2-Dipalmitoyl-sn-glycero-3-phosphocholine (DPPC), 1,2-Dioleoyl-sn-glycero-3-phosphocholine (DOPC) and Cholesterol. Depending on certain circumstances, lipids show different states or phases. Experiments show that these phases separate into distinct domains [VK02, VK05, BHW03b, BG00]. This phenomenon is an important subject of research, not least since [SI97, JMA07] suggested an

influence of the described phases on drug delivery into cells. Further experiments were conducted with multiple lipid compositions [VK03]. Thereby two qualitatively different forms of separation were observed: nucleation and spinodal decomposition. Research on phase separation has been a vivid topic over the past few years, not only in experiments but also in simulations [Möh95]. For a better understanding of this process numerical computations were performed both for mono- and bilayers. Electrostatic line integrals [MM88], Monte Carlo methods [MV97] or kinetic modeling [Ste09] were used for monolayers. For bilayers, Monte Carlo methods [JM95] or molecular dynamics simulations [BMVBT13] were chosen. However, all of these methods are of qualitative nature and lack quantitative comparisons. Only Krüger and Lösche [KL00] used Minkowski measures for this purpose. But they required rather restrictive assumptions. There are limitations in either the dimension or size; interaction between different lipid domains were accounted for in one-dimensional computations or two-dimensional computations were performed for isolated lipid domains. Their work provided new insights into this field of research. But their simulations do not cover real life experiments. We avoid these problems and decided to use the Cahn–Hilliard equation for our simulations. This is not a completely new approach. It was already suggested by [For05] and [FHH10] but with the afore-mentioned drawbacks in quantitative measurement. In contrast to the methods previously discussed, we perform long-time numerical studies for comparably large two-dimensional settings. Thereby our model allows interactions of different lipid domains including topological changes. Furthermore, we present a method for measuring domain sizes with a minimum effort. This allows us to perform not only qualitative but also quantitative comparisons of simulations and experiments.

1.2 Phase Separation in Vesicles

We give a short introduction to the basic biophysical properties of lipid molecules and lipid membranes. Our interest lies in a group of amphiphilic phospholipids, more precisely, phosphatidyl cholines (PC or lecithin). They consist of a hydrophilic phosphoric head and a hydrophobic hydrocarbon tail, as shown in Figure 1.1.

Figure 1.1: Phospholopid with hydrophilic head (red) and hydrophobic tail (black).

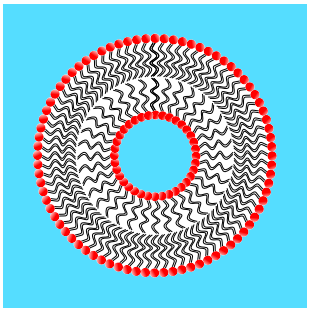

Figure 1.2: Phospholipids surrounded by water form liposomes.

The hydrophobic lipid tails avoid contact to water, due to their amphiphilic character. Once a system of lipid molecules is exposed to water, it shows spontaneous dynamics. The lipids hide their tails from water and form a double layer or bilayer. Then this bilayer further develops into vesicles as shown in Figure 1.2. This way the lipid tails are perfectly protected from contact with water. A special class of vesicles consisting of a small number of different types of lipids are Giant Unilamellar Vesicles (GUVs) which have diameters of up to 200 μm.

Lipids occur in different states, i.e. phases, in membranes. The states are characterized by the lateral mobility of the molecules and the orientation of the lipid tail. A survey of lipid phases is given in Figure 1.3. There are temperature-induced phase transitions. At very low temperatures, i.e. below approximately 21 °C, lipids show a crystalline order. The lipid layer is then in a so-called crystalline phase (L_c) and the molecules are in fixed positions. At higher temperatures lipid molecules show lateral diffusion on the membrane with diffusion rates depending on the given phases and temperatures. When the temperature is raised, a gel phase ($L_{\beta'}$) forms. The name is due to the glass-like behavior. Lipid tails are tilted but still have lateral order. A compound of lipid molecules in gel phase is rather rigid but ductile. At higher temperatures this gel phase evolves into a disordered phase (L_α) and the lipid tails lose their lateral order. The behavior of a compound of lipid molecules in liquid state is comparable to the behavior of liquids. Experiments suggest membranes of pure phases as special cases. In lipid membranes phases coexist, form structures and change in time. The described properties hold true for pressure induced phase transition. Here, the influence of pressure is inversely proportional to temperature. More details on this topic are given in section 6.1.

We want to analyze temperature-induced phase transition. A system relevant for biological processes [Edi03, Pik03, TPEMJ03, DLP02] consists of DOPC (1,2-Dioleoyl-sn-glycero-3-phosphocholine), DPPC (1,2-Dipalmitoyl-sn-glycero-3-phosphocholine) and cholesterol. Cholesterol attaches to saturated phospholipids (DPPC). Similar to the gel phase the tails are or-

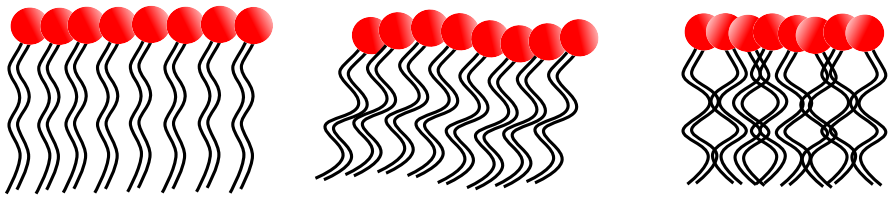

Figure 1.3: Phospholipids in crystalline phase L_c (left) gel phase $L_{\beta'}$ (middle) and disordered phase L_α (right).

dered but the cholesterol inhibits the tails from forming out lateral order. This is called liquid ordered phase. Unsaturated phospholipids (DOPC) attain a liquid disordered phase. Hence, GUVs consisting of DOPC and DPPC show liquid-gel-coexistence phases. For technical reasons electrically charged DPPG (1,2-Dipalmitoyl-sn-glycero-3-phospho-rac-(1-glycerol)) has to be added. Up to a certain concentration its influence can be neglected. Thus we use measurements from such systems in section 5.3 for validation. Non-negligible amounts of DPPG are discussed in section 6.2.

Now we begin with a homogeneous mixture of lipid components at a given temperature T that is above a characteristic temperature T_c. As the temperature exceeds this point the system has perfectly mixed binary phases in the beginning as described above. These phases start to separate into immiscible structures. This phase separation is observed on GUVs by fluorescence microscopy [DBV$^+$01, SMC01, VK02, VK03, BHW03a]. In practice, GUVs get supercooled above T_c and afterwards unfreezed by applying the heat of a microscope lamp. This way homogeneous mixtures are guaranteed in the beginning of the observation. In experiment, domains of saturated phospholipids (DPPC) appear dark, because cholesterol replaces the fluorescence marker. Examples for qualitatively different forms of phase separation are given in Figure 1.4. On one hand, we can see binodal decomposition. Here, lipid domains of circular shape grow by nucleation. On the other hand, we see spinodal decomposition. This process is characterized by its interconnected domains that grow by contraction in time. The qualitative differences are determined by lipid mixtures and temperatures indicated in Figure 1.5. Further details concerning possible causes of binodal and spinodal decomposition are given in section 2.1.

Phase separation results in domains of pure phases. The domains possess lateral mobility within the membrane. Both phases show diffusion rates different from their lipid molecules at corresponding liquid ordered and liquid disordered state. These domains relax over time, reduce their surface and take circular shape or try to reduce the surface line between the different phases. After phase separation the lipid domains still grow either by collision or contraction. In case of binodal decomposition collision of lipid domains is the main factor of growth. Here, two collided domains immediately relax into

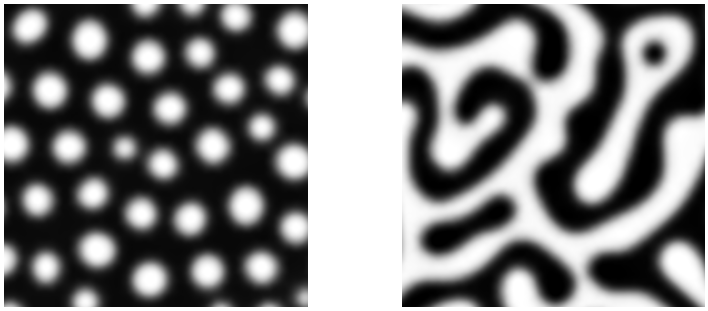

Figure 1.4: Binodal (left) and spinodal phase separation (right)

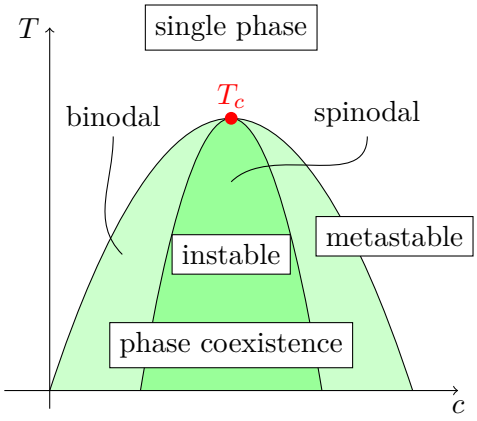

Figure 1.5: Phase diagram of a binary mixture.

a circular shape. By contrast in case of spinodal decomposition contraction is dominant which eventually results in domains of circular shape. Both processes tend to minimize phase boundaries. This suggests line tension as driving force of the system after separation. More information on phase separation in lipid membranes with respect to biophysics and experiments is given in [Lei08].

1.3 Methods and Outline

This thesis investigates phase separation in a qualitative and quantitative manner. Thereby we have to address several problems described below.

In the following chapter 2, we present a physical model for our problem. To this end we interpret the lipid membrane with its coexistent phases as a binary mixture. This allows us to adapt a physical model known for binary alloys. This model was developed by Cahn and Hilliard [CH58, Cah59, Cah61]. Their phase field model describes phase separation and allows topological changes in time. Following [MP96, EZ86, EG96] we give a mathematical formulation of the model, with focus on its boundary condition, and state results on existence and uniqueness of a solution.

Chapter 3 introduces the C^0-Interior Penalty Discontinuous Galerkin (C^0-IPDG) method for the biharmonic problem. This method was discussed for fourth order problems by [BS05, GH09]. We give a general DG approach for the biharmonic equation using the *Hellan–Herrmann–Johnson* (HHJ) method. So far this had been done for DG methods for second order elliptic problems by [ABCM02]. In this context we derive the C^0-IPDG method by opting for numerical fluxes. Afterwards we present a residual-type a posteriori error estimator for this method as we developed in [FHP14]. Adaptivity for C^0-IPDG methods and with special focus to the biharmonic problem has already been discussed in [BGS10, GHV11]. However, compared to [BGS10] we provide a convergence analysis for any polynomial order. In the spirit of [BN10] we show a contraction property for a weighted sum of the C^0-IPDG energy norm of the global discretization error and the estimator. The contraction property is demonstrated with the help of the reliability of the estimator, a quasi-orthogonality result, and an estimator reduction property. We give numerical results for high order approximations of the biharmonic problem. Thereby we achieve theoretically predicted quasi-optimal convergence rates. Later on, we apply the C^0-IPDG method for the biharmonic operator to the Cahn–Hilliard equation derived in chapter 2, in the spirit of [WKG06]. We discretize the nonlinear problem in space and time and formulate a Newton method for the resulting equation. Here, we discuss convergence with respect to the temporal resolution. Finally, we give an outlook on the further development of adaptive methods in space and time.

For a quantitative comparison of simulation and experiment we have

to analyze numerous images in an efficient way. Therefore, we present a structure factor method in chapter 4 which is motivated from crystallography. Here, interference patterns resulting from X-ray scattering are analyzed [Gui63]. We explain this method and show how to use it to measure domain sizes. Issues of application are discussed in a series of exemplary images. This proves the method to be an appropriate tool for automatic quantitative data evaluation.

We present our results in simulation and experiment from [BFL$^+$13] in chapter 5. Here, we focus on the evolution of the mean domain size in time. We investigate the sensitivity of the Cahn–Hilliard equation with respect to its parameters, i.e. diffusion, line tension and free energy for a physical range of parameters. Based on these results we evaluate experimental data on GUVs and compare it to simulations for a certain set of parameters. We make out intrinsic similarities in qualitative and quantitative manner in time. In this way we achieve fairly good results reflecting the nature of lipid membranes. Thus we found a numerically efficient way to simulate and evaluate phase separation in lipid membranes.

In chapter 6 we draw a final conclusion reflecting our results and give an outlook on possible future research. Thereby we show possibilities to extend our model in order to describe systems with charged lipids or lipid membranes on a Langmuir-Blodgett trough. Such extensions may lead to the simulation of chiral lipid domains.

Chapter 2

The Cahn–Hilliard Equation

In order to perform numerical simulations we have to derive a model first. Experimental observation described in section 1.2 suggests a model that reproduces phase decomposition and allows topological changes in time. We choose a phase field model for this purpose in section 2.1. We conduct mathematical analyses for the resulting nonlinear fourth order problem in section 2.2 with special attention to the boundary conditions. Furthermore we give basic results about existence and uniqueness of a solution of our problem.

2.1 Phase Field Model

Cahn and Hilliard introduced a phase field model for binary alloys [CH58, Cah59, Cah61]. Since then the method has successfully been used for various applications, amongst others, in astronomy [Tre03], image processing [BEG07] and simulation of microstructures [Che02]. The method is a promising candidate for us, because experiments suggest lipid phases to be a binary mixture as described in section 1.2. Following the ideas of Cahn and Hilliard we derive a model for our problem as we presented in [BFL$^+$13].

We define an order parameter c reflecting the mole fraction c of a certain lipid phase. This means $c = 0$ and $c = 1$ denote pure phases. This corresponds to the black and white regions shown in Figure 1.4. In order to gain regularity the gradient of the concentration $|\nabla c|$ has to be of the same order as the inverse of the distance between two lipid molecules. This guarantees continuous changes of c from one lipid phase to the other. The relation between the gradient of the concentration and the line tension is discussed later on.

Each lipid molecule belongs to a certain phase. Its free energy depends on its surroundings. Lipid molecules feel most comfortable with neighboring lipid molecules of the same phase which is why they accumulate with those. We introduce a local free energy f per area. It depends on the local phase

concentration c and its derivatives. In each instance the local free energy penalizes mixtures of phases. This corresponds to the afore-mentioned properties of lipid molecules. The local free energy f makes local concentrations of pure phases to be energetically favorable. Hence, it is the driving force of phase decomposition in regions with homogeneous mixtures.

Similar to the assumptions on the concentration c before, we assume f to be a continuous function with respect to its variables. Additionally, we assume c and its derivatives to be independent of each other. This allows us to apply Taylor series expansion and approximate f at the homogeneous concentration c_0. This leads to

$$\begin{aligned} f(c, \nabla c, \nabla^2 c, \ldots) = f(c_0) &+ \sum_i L_i(\partial c/\partial x_i) + \sum_{ij} \kappa_{ij}^{(1)}(\partial^2 c/(\partial x_i \partial x_j)) \\ &+ \frac{1}{2}\sum_{ij} \kappa_{ij}^{(2)}(\partial c/\partial x_i)(\partial c/\partial x_j) + \ldots, \end{aligned} \tag{2.1}$$

with coefficients given by

$$L_i = \left.\frac{\partial f(c)}{\partial(\partial c/\partial x_i)}\right|_{c_0}, \tag{2.2}$$

$$\kappa_{ij}^{(1)} = \left.\frac{\partial f(c)}{\partial(\partial^2 c/(\partial x_i \partial x_j)}\right|_{c_0}, \tag{2.3}$$

$$\kappa_{ij}^{(2)} = \left.\frac{\partial f(c)}{\partial(\partial c/\partial x_i)\partial(\partial c/\partial x_j)}\right|_{c_0}. \tag{2.4}$$

For symmetry reasons f does not depend on the orientation of ∇c. Hence, we only count even powers of the gradient such that the Taylor series (2.1) reduces to

$$f(c, \nabla c, \nabla^2 c, \ldots) = f(c_0) + \kappa_1 \nabla^2 c + \kappa_2 (\nabla c)^2 + \ldots, \tag{2.5}$$

with $\kappa_1 = (\partial f(c)/\partial \nabla^2 c)|_{c_0}$ and $\kappa_2 = (\partial^2 f(c)/(\partial |\nabla c|)^2)|_{c_0}$. Then the approximated total free energy F of a given domain Ω is given by the integration of (2.5), i.e.

$$F(c_0) \simeq \int_\Omega \left(f(c_0) + \kappa_1 \nabla^2 c + \kappa_2 (\nabla c)^2\right) \mathrm{d}x. \tag{2.6}$$

Integration by parts for the second term results in

$$\int_\Omega \kappa_1 \nabla^2 c \, \mathrm{d}x = -\int_\Omega \frac{\mathrm{d}\kappa_1}{\mathrm{d}c}(\nabla c)^2 \, \mathrm{d}x + \int_{\partial\Omega} (\kappa_1 \nabla c \cdot \boldsymbol{n}) \, \mathrm{d}s. \tag{2.7}$$

Here, mass conservation motivates us to impose

$$\nabla c \cdot \boldsymbol{n} = 0 \qquad \text{on } \partial\Omega. \tag{2.8}$$

By substituting (2.7) into (2.6) there holds

$$F(c_0) \simeq \int_\Omega \Big(\frac{\epsilon^2}{2} (\nabla c_0)^2 + f(c_0) \Big) \, \mathrm{d}x, \tag{2.9}$$

where

$$\frac{\epsilon^2}{2} := -\frac{d\kappa_1}{dc} + \kappa_2 = -\frac{\partial^2 f}{\partial c \, \partial \nabla^2 c}\Big|_{c_0} + \frac{\partial^2 f}{\partial (|\nabla c|)^2}\Big|_{c_0}. \tag{2.10}$$

We now extend the total free energy $F(c_0)$ by simply re-defining the local free energy $f(c_0)$ for inhomogeneous concentrations c. Therefore we introduce a double well potential, e.g. $f(c) := \varphi c^2 (c-1)^2$, depending only on the concentration c as a simple choice for our local free energy. Here, the parameter φ serves as a physical scaling parameter. More sophisticated versions are possible with respect to a given phase diagram as sketched in Figure 2.1.

We further discuss our approximated total free energy given by (2.9). Its first term $\frac{\epsilon^2}{2}(\nabla c)^2$ vanishes on regions with constant concentration whereas regions with phase boundaries give contributions to the total free energy. It is rather difficult to give a physical interpretation of the parameter ϵ^2. In connection to the total free energy F it can be interpreted as line tension. But this interpretation is only valid in a variational sense, see [RW82]. From a microscopic point of view it reflects the interaction of lipids of different phases. The second term connected to the local free energy $f(c)$ which is a double well potential in our case, is minimal at regions of pure lipid phases.

Nature tends to minimize its free energy. We analyse how this influences a lipid mixture over time. We start from a homogeneous mixture of lipid phases. In absence of phase boundaries, the local free energy is the driving force of our system in the beginning. Consequently, lipid phases separate and regions of pure phases occur. After a certain amount of time, lipid phases have separated completely. Now, the term connected to the line tension is dominant. This influences the domain structures, because lipid domains fuse and reduce their boundaries. We see that the behavior of our model is in agreement with experimental observations described in section 1.2.

Let us formalize this process in time by physical arguments. The chemical potential μ_{chem} can be defined by the variational derivative of the total free energy F, i.e.

$$\mu_{\text{chem}}(c) = \frac{\delta F}{\delta c}. \tag{2.11}$$

We further introduce a dynamical system using Fick's first law, such that the mass flow is prescribed by

$$\mathbf{J} = -M(c) \nabla \mu_{\text{chem}}, \tag{2.12}$$

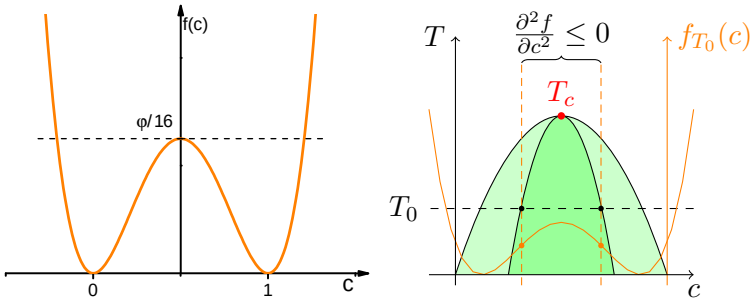

Figure 2.1: Local free energy $f(c)$ as double well potential (left) and matched to a binary mixture (right). [BFL$^+$13]

where $M(c)$ denotes the mobility of the lipids depending on their local concentration c. Again, mass conservation motivates us to imply the boundary condition

$$\mathbf{J} \cdot \boldsymbol{n} = 0 \qquad \text{on } \partial\Omega. \tag{2.13}$$

Then the change of concentration in time is given by

$$\frac{\partial c}{\partial t} = -\nabla \cdot \mathbf{J}(c), \tag{2.14}$$

so that conservation of mass is guaranteed. Altogether, we get the Cahn–Hilliard equation

$$\frac{\partial c}{\partial t} = \nabla \cdot (M(c)\, \nabla[f'(c) - \epsilon^2 \Delta c]), \tag{2.15}$$

with previously described boundary conditions. An exemplary choice for the mobility would be a linear combination of the diffusion constants D_0 and D_1 of the pure lipid phases at concentration $c = 0$ and $c = 1$, e.g. $M(c) = D_0(1 - c) + D_1(c)$. This may lead to degenerated mobilities which means the mobility vanishes for certain concentrations. However, in our case we use constant mobility $M_D = D$, assuming the phases to possess the same diffusion rates D, see [OWL05]. This leads to a simplified Cahn–Hilliard equation with three physical parameters D [m^2/s], φ [J/m^2] and ϵ^2 [J]. For further information on the resulting Cahn–Hilliard equation itself, its properties and its practical impact we refer to [Ell89] and [NC98].

2.2 Existence and Uniqueness

Following [MP96] we give a mathematical formulation for the Cahn–Hilliard equation (2.15) . For simplicity we assume a constant mobility $M_D = D$ with positive diffusion coefficient $D \in \mathbb{R}^+$. This is sufficient for our simulations in section 5.

So far we derived the Cahn–Hilliard equation (2.15) by physical arguments. This equation describes the change of concentration in time in a given domain Ω. By contrast, we present a mathematical approach with special focus on the boundary conditions here. To do so we go back to the total free energy (2.9) and derive the Cahn–Hilliard equation (2.15) from a mathematical point of view. However, once more we utilize the fact that nature tends to take energetically favorable states. In order to minimize the total free energy of our system depending on our concentration c, the concentration changes in time according to

$$\frac{\mathrm{d}c}{\mathrm{d}t}(t) = -\nabla F(c). \tag{2.16}$$

In doing so, we have to be aware to allow only mass conserving gradients of the total free energy with respect to our concentration c. Previously, we fulfilled this restriction by physical arguments. In this case conservation of mass allows only those gradients ∇F with

$$\int_\Omega \nabla F \, \mathrm{d}x = 0. \tag{2.17}$$

Consequently, the total concentration over the domain Ω is constant, since substituting our restriction (2.17) into (2.16) leads to

$$\int_\Omega \frac{\mathrm{d}c}{\mathrm{d}t}(t) \, \mathrm{d}x = 0. \tag{2.18}$$

From this we can see that there is a constant $C_{\mathrm{mean}} \in \mathbb{R}^+$ meaning that at any time t in the time interval $[0, T]$ there holds

$$\int_\Omega c(t) \, \mathrm{d}x = C_{\mathrm{mean}}. \tag{2.19}$$

In this case, the constant C_{mean} denotes the mean concentration over time. Now the gradient of the total free energy ∇F for a given concentration c at time $t \in [0, T]$ is connected to the change in time of the total free energy in the sense that

$$\frac{\mathrm{d}F}{\mathrm{d}t}(c(t)) = (\nabla F(c), \frac{\mathrm{d}c}{\mathrm{d}t}(t))_H, \tag{2.20}$$

where we have to appropriately choose H regarding mass conservation of our concentration c. Nevertheless, by substituting (2.16) into (2.20) we get

$$\frac{\mathrm{d}F}{\mathrm{d}t}(c(t)) = -\|\frac{\mathrm{d}c}{\mathrm{d}t}(t)\|_H^2 \leq 0. \tag{2.21}$$

Thus the total free energy F minimizes over time once more. However, we still have to look for an appropriate Hilbert space H in order to guarantee

the afore-mentioned mass conservation of the concentration c. Therefore, we define

$$\bar{H}^{-1}(\Omega) := \{v \in L^2(\Omega) \,|\, \int_\Omega v \, \mathrm{d}x = 0\} \subset H^{-1}(\Omega). \tag{2.22}$$

Accordingly we receive the following result for elements in $\bar{H}^{-1}(\Omega)$ [MP96].

Lemma 2.1. *$v \in \bar{H}^{-1}$ if and only if the Neumann boundary value problem*

$$-\nabla \cdot M_D \nabla \Phi_v = v, \quad \text{in } \Omega, \tag{2.23}$$

$$\frac{\partial \Phi_v}{\partial \boldsymbol{n}} = 0, \quad \text{on } \Gamma, \tag{2.24}$$

has a unique solution $\Phi_v(x)$ satisfying $\int_\Omega \Phi_v(x) \; dx = 0$.

Here we introduce the constant mobility M_D in equation (2.23). This makes sense, as the equation represents the diffusion of our concentration on Ω. We therefore call it gradient flow in $\bar{H}^{-1}(\Omega)$. Using equation (2.24) we also impose the normal derivatives of our concentration c to vanish on the boundary $\Gamma := \partial\Omega$. This way we avoid an additional entry of concentration from the boundary. Let $v_1, v_2 \in \bar{H}^{-1}$, and Φ_{v_1}, Φ_{v_2} their corresponding solutions according to Lemma 2.1. Thus we define

$$(v_1, v_2)_{\bar{H}^{-1}} := (M_D \nabla \Phi_{v_1}, \nabla \Phi_{v_2})_{0,\Omega}. \tag{2.25}$$

Consequently $\bar{H}^{-1}$ combined with the scalar product (2.25) is a scalar product space and for $v \in \bar{H}^{-1}$. Furthermore, we have equivalent norms $\|v\|_{H^{-1}}$ and $\|v\|_{\bar{H}^{-1}}$ on $\bar{H}^{-1}$ [MP96]. Overall, we can guarantee mass conservation for $\nabla F \in \bar{H}^{-1}$. For $v \in \bar{H}^{-1}$ the mass conservative directional derivative in time of the total free energy is given by

$$\frac{\mathrm{d}F}{\mathrm{d}t}(c + tv)|_{t=0} = (\nabla F(c), v)_{0,\Omega}. \tag{2.26}$$

For our total free energy (2.9) there holds

$$\nabla F(c) = f'(c) - \epsilon^2 \Delta c. \tag{2.27}$$

By substituting (2.27) into (2.26) we obtain

$$\frac{\mathrm{d}F}{\mathrm{d}t}(c + tv)|_{t=0} = (f'(c) - \epsilon^2 \Delta c, v)_{0,\Omega}, \quad \forall v \in \bar{H}^{-1}. \tag{2.28}$$

According to Lemma 2.1 there exists a solution Φ_v for $v \in \bar{H}^{-1}$ such that

$$-\nabla \cdot M_D \nabla \Phi_v = v. \tag{2.29}$$

Thus for (2.28) there holds

$$\frac{\mathrm{d}F}{\mathrm{d}t}(c+tv)|_{t=0} = (f'(c) - \epsilon^2\Delta c, -\nabla \cdot M_D \nabla \Phi_v)_{0,\Omega}. \tag{2.30}$$

Then integration by parts yields

$$\frac{\mathrm{d}F}{\mathrm{d}t}(c+tv)|_{t=0} = (M_D \nabla (f'(c) - \epsilon^2\Delta c), \nabla \Phi_v)_{0,\Omega}. \tag{2.31}$$

Here, we assume on our boundary Γ that

$$\frac{\partial}{\partial \boldsymbol{n}}(f'(c) - \epsilon^2\Delta c) = 0, \tag{2.32}$$

and we find a $\tilde{v} \in \bar{H}^{-1}$ according to Lemma 2.1 such that

$$\tilde{v} := -\nabla \cdot M_D \nabla \Phi_{\tilde{v}} = -\nabla \cdot M_D \nabla (f'(c) - \epsilon^2\Delta c). \tag{2.33}$$

Using the equivalence of scalar products (2.25), (2.31) reads as follows

$$\frac{\mathrm{d}F}{\mathrm{d}t}(c+tv)|_{t=0} = (M_D \nabla \Phi_{\tilde{v}}, \nabla \Phi_v)_{0,\Omega} = (\tilde{v}, v)_{\bar{H}^{-1}}. \tag{2.34}$$

When we compare (2.31) to (2.26) we see that

$$\nabla_{\bar{H}^{-1}} F(c) := -\nabla \cdot M_D \nabla (f'(c) - \epsilon^2\Delta c). \tag{2.35}$$

Finally, we substitute (2.35) into (2.16) and obtain the Cahn–Hilliard equation with mass preserving boundary conditions:

$$\frac{\partial c}{\partial t} = \nabla \cdot M_D \nabla (f'(c) - \epsilon^2\Delta c), \quad \text{in } \Omega, \tag{2.36}$$

$$\frac{\partial c}{\partial n} = \frac{\partial}{\partial n}(f'(c) - \epsilon^2\Delta c) = 0, \quad \text{on } \Gamma. \tag{2.37}$$

Considering existence and uniqueness we cite the following result according to [EZ86].

Theorem 2.2. *Let $\Omega \subset \mathbb{R}^n, n \leq 3$ be a domain with sufficiently smooth boundary $\Gamma = \partial\Omega$, ϵ^2, $M_D \in \mathbb{R}^+$ and $f'(c) = c - \gamma_1 c^2 - \gamma_2 c^3$, with $\gamma_1 \in \mathbb{R}$, $\gamma_2 \in \mathbb{R}^+$. Then for any initial data $c_0 \in H^2_E(\Omega)$, with*

$$H^2_E(\Omega) := \{v \in H^2(\Omega) \,|\, \frac{\partial v}{\partial \boldsymbol{n}} = 0 \text{ on } \Gamma\}, \tag{2.38}$$

there exists a unique solution $c = c(t,x)$ of the Cahn–Hilliard equation (2.36) *with mass preserving boundary conditions* (2.37) *for a given time interval $(0,T)$, $T \in \mathbb{R}^+$ in*

$$\begin{aligned} H^{4,1}(\Omega \times (0,T)) = \{v(t,x) \,|\, & \quad v \in L^2((0,T), H^4(\Omega)), \\ & \frac{\partial v}{\partial t} \in L^2((0,T), L^2(\Omega))\}. \end{aligned} \tag{2.39}$$

This result covers our set of application. For further information, for example on degenerated mobilities and different forms of local free energies f, we refer to [EG96].

Chapter 3

C^0-Interior Penalty Discontinuous Galerkin Methods

First in section 3.1 we introduce *continuous/discontinuous Galerkin* (CDG) methods with special focus on fourth order problems. In particular, we derive a *C^0-interior penalty discontinuous Galerkin* (C^0-IPDG) method for the biharmonic problem known from [BS05]. Further, in section 3.2 we develop an adaptive finite element method for this formulation and provide a convergence analysis as we presented in [FHP14]. Using this C^0-IPDG formulation for the biharmonic problem, in section 3.3 we derive a C^0-IPDG method of the Cahn–Hilliard equation (2.36) – (2.37), in the spirit of [WKG06].

3.1 Continuous/Discontinuous Galerkin Methods

Continuous Galerkin (CG) methods for fourth order problems require C^1 elements [AFS68, BFS65, DJDPS79]. These conforming approximations of the Cahn–Hilliard equation (2.36) – (2.37) are computationally expensive. We therefore look for a nonconforming approach. Reed and Hill [RH73] introduced a *Discontinuous Galerkin* (DG) method for solving hyperbolic equations. Since then, various DG methods have been developed for different types of problems. A unified analysis of discontinuous Galerkin methods for elliptic problems is given in [ABCM02]. We refer to this source as a general introduction to DG methods. Regarding fourth-order problems there are nonconforming approaches, for example [Bak77]. A convenient approach is to use standard C^0 or Lagrange elements known from CG methods for second order elliptic problems. The development of such *continuous/discontinuous Galerkin* (CDG) methods for two-dimensional problems goes back to [BZ73]. It can be seen as a hybrid approach combining CG and DG methods. CDG methods for fourth order problems methods were proposed by [EGH$^+$02]

and [WGM04]. In the spirit of the unified analysis of DG methods for second order elliptic equations presented in [ABCM02], we present a unified approach for the biharmonic equation, an exemplary fourth order problem. In this context, the C^0-IPDG method suggested in [BS05] turns out to be a symmetric interior penalty DG method characterized by the choice of numerical fluxes. We follow our work presented in [FHP14] to show this result and introduce the C^0-IPDG method to the biharmonic equation by the Hellan-Herrmann-Johnson (HHJ) approach [Hel67, Her67, Vis69, Joh73].

Let $\Omega \subset \mathbb{R}^2$ be a bounded polygonal domain with boundary $\Gamma = \partial\Omega$ and $f \in L^2(\Omega)$. The biharmonic problem is given by

$$\Delta^2 u = f \quad \text{in } \Omega, \tag{3.1}$$

$$u = \frac{\partial u}{\partial \boldsymbol{n}} = 0 \quad \text{on } \Gamma. \tag{3.2}$$

A weak formulation of (3.1) – (3.2) is to find a solution $u \in V := H_0^2(\Omega)$ such that

$$a(u, v) = (f, v)_{0,\Omega}, \quad v \in V, \tag{3.3}$$

where the bilinear form $a(\cdot, \cdot)$ is defined by

$$a(v, w) := (D^2 v, D^2 w)_{0,\Omega} := \sum_{|\beta|=2} (D^\beta v, D^\beta w)_{0,\Omega}, \quad v, w \in V. \tag{3.4}$$

The bilinear form is bounded and V-elliptic. Thus, the Lax–Milgram lemma guarantees the existence and uniqueness of a weak solution.

The regularity requires us to use C^1 elements rather than C^0 elements in order to get a conforming numerical approximation. Instead we apply the Hellan–Herrmann–Johnson (HHJ) method and reformulate the biharmonic problem (3.1) – (3.2) into a system of second order equations, such that

$$\boldsymbol{p} - D^2 u = 0, \tag{3.5}$$

$$\nabla \cdot (\nabla \cdot \boldsymbol{p}) = f. \tag{3.6}$$

We further define the matrix-valued function space

$$\begin{aligned} \boldsymbol{Q}(\mathrm{div}; \Omega) := \{\boldsymbol{p} = (\boldsymbol{p}_1, \boldsymbol{p}_2)^T \,|\, \boldsymbol{p}_i \in \boldsymbol{H}(\mathrm{div}; \Omega), 1 \le i \le 2, \\ \nabla \cdot \boldsymbol{p} \in \boldsymbol{H}(\mathrm{div}; \Omega)\}. \end{aligned} \tag{3.7}$$

Here, we used $(\nabla \cdot \boldsymbol{p})_i := \sum_{j=1}^2 \partial \boldsymbol{p}_{ij}/\partial x_j, 1 \le i \le 2$, together with the vector-valued space

$$\begin{aligned} \boldsymbol{H}(\mathrm{div}; \Omega) := \{\boldsymbol{v} = (v_1, v_2)^T \,|\, v_i \in L^2(\Omega), 1 \le i \le 2, \\ \nabla \cdot \boldsymbol{v} \in L^2(\Omega)\}. \end{aligned} \tag{3.8}$$

Now, we use the fact that $D^2u = \nabla \cdot (\nabla u)$ and apply integration by parts. Then the weak formulation of (3.5) – (3.6) is to find a pair $(\boldsymbol{p}, u) \in \boldsymbol{Q}(\mathrm{div}; \Omega) \times H_0^2(\Omega)$, such that

$$\int_\Omega \boldsymbol{p} : \boldsymbol{q} \, \mathrm{d}x + \int_\Omega \nabla u \cdot \nabla \cdot \boldsymbol{q} \, \mathrm{d}x = 0 \,, \qquad \boldsymbol{q} \in \boldsymbol{Q}(\mathrm{div}; \Omega), \tag{3.9}$$

$$\int_\Omega \boldsymbol{p} : D^2 v \, \mathrm{d}x = \int_\Omega f v \, \mathrm{d}x, \quad v \in H_0^2(\Omega). \tag{3.10}$$

Let us discretize our system of equations (3.9) – (3.10) and introduce a geometrically conforming simplicial triangulation $\mathcal{T}_h$ of Ω. Let further $P_k(T)$, $k \in \mathbb{N}$, $k \geq 2$, be the linear space of polynomials of degree less or equal k on a triangle $T \in \mathcal{T}_h$. The lower restriction on the polynomial degree is due to the second order derivatives in (3.10). This guarantees nonzero polynomials after differentiation. According to [BS08], the space of Lagrangian finite elements of type k is given by

$$V_h := \{v_h \in C_0^0(\Omega) \mid v_h|_T \in P_k(T), \; T \in \mathcal{T}_h\}. \tag{3.11}$$

Furthermore, we define the matrix-valued function space $\boldsymbol{Q}_h$ by

$$\begin{aligned} \boldsymbol{Q}_h := \{\boldsymbol{q}_h \in C^0(\Omega)^{2\times 2} \mid \boldsymbol{q}_h = (q_{ij})_{i,j=1}^2, \; 1 \leq i, j \leq 2, \\ q_{ij}|_T \in P_k(T), \; T \in \mathcal{T}_h\}. \end{aligned} \tag{3.12}$$

Then the discretized version of our weak formulation (3.9) – (3.10) is to find a pair $(\boldsymbol{p}_h, u_h) \in \mathbf{Q}_h \times V_h$, such that for $\boldsymbol{q}_h \in \boldsymbol{Q}_h$ and $v_h \in V_h$ there holds

$$\begin{aligned} \sum_{T\in\mathcal{T}_h} \int_T \boldsymbol{p}_h : \boldsymbol{q}_h \, \mathrm{d}x + \sum_{T\in\mathcal{T}_h} \int_T \nabla u_h \cdot \nabla \cdot \boldsymbol{q}_h \, \mathrm{d}x \\ - \sum_{T\in\mathcal{T}_h} \int_{\partial T} \hat{\boldsymbol{u}}_h \cdot \boldsymbol{q}_h \boldsymbol{n}_{\partial T} \, \mathrm{d}s = 0, \end{aligned} \tag{3.13}$$

$$\sum_{T\in\mathcal{T}_h} \int_T \boldsymbol{p}_h : D^2 v_h \, \mathrm{d}x - \sum_{T\in\mathcal{T}_h} \int_{\partial T} \hat{\boldsymbol{p}}_h \cdot \nabla v_h \, \mathrm{d}s = \sum_{T\in\mathcal{T}_h} \int_T f v_h \, \mathrm{d}x. \tag{3.14}$$

Here, $\hat{\boldsymbol{u}}_h$ and $\hat{\boldsymbol{p}}_h$ denote numerical fluxes over the edges of our triangulation $\mathcal{T}_h$. The fluxes can be seen as numerical approximations of the normal derivatives of u and $\boldsymbol{p}$ arising from the integration by parts per element $T \in \mathcal{T}_h$ of the system of equations (3.5) – (3.6). However, these derivatives do not exist for u_h and $\boldsymbol{p}_h$ in a global context. The derivatives are not-well defined on the edges of the triangulation $T \in \mathcal{T}_h$. Here we remember that V_h and $\boldsymbol{Q}_h$ are C^0 element spaces. The specific choice of the fluxes will be discussed later. For now, we mention that they influence the stability and the accuracy of the resulting method. For the moment it is enough to know that the fluxes $\hat{\boldsymbol{u}}_h$ and $\hat{\boldsymbol{p}}_h$ are defined by jumps and averages of normal derivatives of u_h and $\boldsymbol{p}_h$ on the edges of our triangulation $\mathcal{T}_h$. We

remark that the normal derivatives of $\boldsymbol{p}_h$ are directly related to the normal derivatives of u_h by the equation (3.5). Here, we have nonzero jumps of the normal derivatives of both u_h and $\boldsymbol{p}_h$, because despite our restriction to polynomial degrees, the discretized spaces V_h and $\boldsymbol{Q}_h$ consist of C^0 elements. Unlike for C^1 elements the normal derivatives are not continuous over edges. Consequently, we cannot expect vanishing jumps of any normal derivatives. Thus we have a nonconforming approximation (3.13) – (3.14) of our weak formulation (3.3) because $V_h \not\subset H_0^2(\Omega)$.

Nevertheless we use the occurring jumps for our purpose. To do so in our nonconforming approximation (3.13) – (3.14) we transform sums over triangles into sums over edges for those terms where the boundary integral of a triangle T is evaluated. It is clear that every boundary integral is evaluated twice on every interior edge, because every interior edge $E \in \mathcal{E}_h^\Omega$ belongs to two triangles. Thus we define averages and jumps over edges and introduce a fixed numbering to our triangles $T \in \mathcal{T}_h$. This allows us to introduce unique jumps and averages. Now an interior edge $E \in \mathcal{E}_h^\Omega$ is defined by $E := T_i \cap T_j$, $i > j$, and the associated triangles are uniquely defined as $T_E^+ := T_i$, $T_E^- := T_j$. The set of boundary edges is denoted by $\mathcal{E}_h^\Gamma$. Then the total set of edges is defined by $\mathcal{E}_h := \mathcal{E}_h^\Omega \cup \mathcal{E}_h^\Gamma$. The unit normal vector $\boldsymbol{n}$ on $E \in \mathcal{E}_h^\Omega$ points from T_E^- to T_E^+. For $E \in \mathcal{E}_h^\Gamma, E = T_\ell \cap \Gamma$, we set $T_E := T_\ell$ and refer to $\boldsymbol{n}$ as the exterior unit normal vector for $E \in \mathcal{E}_h^\Gamma$. Further, we refer to $\boldsymbol{t}$ as the unit tangential vector for $E \in \mathcal{E}_h$ defined by the $\pi/2$ counterclockwise rotation of $\boldsymbol{n}$. Finally, for first and second order derivatives, $1 \le \nu \le 2$, averages and jumps are uniquely determined by

$$\{\!\{\frac{\partial^\nu v_h}{\partial \boldsymbol{n}^\nu}\}\!\} := \begin{cases} \frac{1}{2}\frac{\partial^\nu v_h}{\partial \boldsymbol{n}^\nu}|_{E\cap T_E^+} + \frac{1}{2}\frac{\partial^\nu v_h}{\partial \boldsymbol{n}^\nu}|_{E\cap T_E^-} \ , \ E \in \mathcal{E}_h^\Omega, \\ \frac{\partial^\nu v_h}{\partial \boldsymbol{n}^\nu}|_{E\cap T_E} \ , \ E \in \mathcal{E}_h^\Gamma, \end{cases} \tag{3.15}$$

$$[\![\frac{\partial^\nu v_h}{\partial \boldsymbol{n}^\nu}]\!] := \begin{cases} \frac{\partial^\nu v_h}{\partial \boldsymbol{n}^\nu}|_{E\cap T_E^+} - \frac{\partial^\nu v_h}{\partial \boldsymbol{n}^\nu}|_{E\cap T_E^-} \ , \ E \in \mathcal{E}_h^\Omega, \\ \frac{\partial^\nu v_h}{\partial \boldsymbol{n}^\nu}|_{E\cap T_E} \ , \ E \in \mathcal{E}_h^\Gamma. \end{cases} \tag{3.16}$$

Let us choose the numerical fluxes over $E \in \mathcal{E}_h$ according to

$$\hat{\boldsymbol{u}}_h := \{\!\{\frac{\partial u_h}{\partial \boldsymbol{n}}\}\!\}\boldsymbol{n} + \{\!\{\frac{\partial u_h}{\partial \boldsymbol{t}}\}\!\}\boldsymbol{t}, \tag{3.17}$$

$$\hat{\boldsymbol{p}}_h := \{\!\{\frac{\partial^2 u_h}{\partial \boldsymbol{n}^2}\}\!\}\boldsymbol{n}_{\partial T} + \frac{\alpha}{h_E}[\![\frac{\partial u_h}{\partial \boldsymbol{n}}]\!]\boldsymbol{n}_{\partial T}, \tag{3.18}$$

where h_E denotes the length of the edge E and $\alpha \in \mathbb{R}$, $\alpha > 1$, is an appropriately chosen penalty parameter. On one hand, we want to penalize occurring jumps and on the other hand, we want to have a symmetric formulation regarding jumps and averages of trial and test functions. It is essential that due to the choice of the numerical fluxes (3.17), (3.18) the dual variable $\boldsymbol{p}_h$ can be eliminated from the system (3.13) – (3.14). By substituting (3.13) into (3.14), transforming the sums over triangles into sums over edges and

using our previously chosen numerical fluxes (3.17) and (3.18), we get the C^0-IPDG method for our biharmonic problem (3.3). Altogether we have to find a solution $u_h \in V_h$, such that

$$a_h^{IP}(u_h, v_h) = (f, v_h)_{0,\Omega}, \quad v_h \in V_h, \tag{3.19}$$

where the mesh-dependent bilinear form $a_h^{IP}(\cdot,\cdot) : V_h \times V_h \to \mathbb{R}$, is given by

$$\begin{aligned} a_h^{IP}(u_h, v_h) := &\sum_{T\in\mathcal{T}_h} (D^2 u_h, D^2 v_h)_{0,T} + \sum_{E\in\mathcal{E}_h^{\bar{\Omega}}} (\{\!\!\{ \frac{\partial^2 u_h}{\partial \boldsymbol{n}^2} \}\!\!\}, [\![\frac{\partial v_h}{\partial \boldsymbol{n}}]\!])_{0,E} \\ &+ \sum_{E\in\mathcal{E}_h^{\bar{\Omega}}} ([\![\frac{\partial u_h}{\partial \boldsymbol{n}}]\!], \{\!\!\{ \frac{\partial^2 v_h}{\partial \boldsymbol{n}^2} \}\!\!\})_{0,E} + \alpha \sum_{E\in\mathcal{E}_h^{\bar{\Omega}}} h_E^{-1} ([\![\frac{\partial u_h}{\partial \boldsymbol{n}}]\!], [\![\frac{\partial v_h}{\partial \boldsymbol{n}}]\!])_{0,E}. \end{aligned} \tag{3.20}$$

Now, we have a nonconforming method for our biharmonic problem (3.3) using C^0 elements instead of C^1 elements required for conforming approximations of fourth order problems. We already mentioned the occurring jumps over edges using C^0 elements due to their reduced regularity. The jumps and averages are part of the numerical fluxes. Their choice was actually free but however motivated by the afore-mentioned goals. In fact, we defined the fluxes similarly to the fluxes used for the symmetric interior penalty method for second order elliptic equations shown in [ABCM02]. Therein the choice of fluxes was motivated by the same goals. This analogy suggests that other fourth order formulations can be derived using similar fluxes known from other DG methods for second order elliptic problems.

A closer look at the bilinear form (3.20), especially its terms related to the edges, reveals its improper definition for $v, w \in V$. We fix this problem by introducing a lifting operator $\boldsymbol{L} : L^2(\mathcal{E}_h)^2 \to \boldsymbol{Q}_h$. This operator is known from DG approximations of second order problems [HSW04, HSW07] or for IPDG approximations of the biharmonic problem [GHV11]. The lifting operator is defined by

$$(\boldsymbol{L}(\boldsymbol{v}), \boldsymbol{q}_h)_{0,\Omega} := \sum_{E\in\mathcal{E}_h} ([\![\boldsymbol{n} \cdot \boldsymbol{v}]\!]_E, \{\!\!\{ \boldsymbol{n} \cdot \boldsymbol{q}_h \boldsymbol{n} \}\!\!\}_E)_{0,E}, \quad \boldsymbol{q}_h \in \boldsymbol{Q}_h. \tag{3.21}$$

Using this, we define our bilinear form $a_h^{IP}(\cdot,\cdot)$ for elements of $V + V_h$ by

$$\begin{aligned} a_h^{IP}(v, w) := &\sum_{T\in\mathcal{T}_h} (D^2 v, D^2 w)_{0,T} + \sum_{T\in\mathcal{T}_h} (\boldsymbol{L}(\nabla w), D^2 v)_{0,T} \\ &+ \sum_{T\in\mathcal{T}_h} (\boldsymbol{L}(\nabla v), D^2 w)_{0,T} + \alpha \sum_{E\in\mathcal{E}_h} h_E^{-1} ([\![\frac{\partial v}{\partial \boldsymbol{n}}]\!]_E, [\![\frac{\partial w}{\partial \boldsymbol{n}}]\!]_E)_{0,E}. \end{aligned} \tag{3.22}$$

In doing so, we have to mention that we reused the notation of our original bilinear form $a_h^{IP}(\cdot,\cdot) : V_h \times V_h \to \mathbb{R}$. We further define the mesh-dependent C^0-IPDG norm on $V + V_h$ by

$$\|v\|_{2,h,\Omega}^2 := \sum_{T\in\mathcal{T}_h} |v|_{2,T}^2 + \sum_{E\in\mathcal{E}_h} \frac{\alpha}{h_E} \| [\![\frac{\partial v}{\partial \boldsymbol{n}}]\!]_E \|_{0,E}^2, \quad v \in V + V_h, \tag{3.23}$$

with

$$|\cdot|_{2,T}^2 := \sum_{|\beta|=2} \|D^\beta \cdot\|_{0,T}^2, \quad T \in \mathcal{T}_h. \tag{3.24}$$

This allows us to give some a priori estimates proved in [BS05], showing our bilinear form $a_h^{IP}(\cdot,\cdot)$ to be elliptic and bounded. Firstly, for sufficiently large penalty parameter α there exists a positive constant $\gamma < 1$, such that

$$a_h^{IP}(v,v) \geq \gamma \|v\|_{2,h,\Omega}^2, \quad v \in V + V_h. \tag{3.25}$$

Moreover, there exists a constant $C_1 > 1$ such that for any penalty parameter $\alpha \geq 1$ there holds

$$a_h^{IP}(v,v) \leq C_1 \|v\|_{2,h,\Omega}^2, \quad v \in V + V_h. \tag{3.26}$$

Finally, from the ellipticity (3.25) and the boundedness (3.26) of our bilinear form $a_h^{IP}(\cdot,\cdot)$ we deduce the existence and uniqueness of a solution $u_h \in V_h$ for our C^0-IPDG method (3.19). Further details including an a priori error analysis are given in [BS05].

3.2 Convergence Analysis of an Adaptive Method

In this section, we derive an *adaptive finite element method* (AFEM) based on a residual-type a posteriori error estimator for our previously presented C^0-IPDG method (3.19) for the biharmonic problem (3.1) – (3.2). Further, we present results on a convergence analysis for any polynomial order. The results presented are excerpts from our work published in [FHP14]. As an introductory source to this field of interest we refer to literature on AFEMs for second order elliptic boundary value problems, e.g. [AO00, BS01, BR03, EEHJ95, NR04, Ver96].

3.2.1 A Residual-type A Posteriori Error Estimator

An a posteriori error analysis considering the C^0-IPDG method (3.19) in case $k = 2$ was first given in [BGS10]. For $k \geq 2$, we introduce the residual-type a posteriori error estimator

$$\eta_h := \Big(\sum_{T \in \mathcal{T}_h} \eta_T^2 + \sum_{E \in \mathcal{E}_h^\Omega} \eta_E^2 \Big)^{1/2}, \tag{3.27}$$

with element residuals η_T and edge residuals η_E defined by

$$\eta_T^2 := h_T^4 \|f - \Delta^2 u_h\|_{0,T}^2, \quad T \in \mathcal{T}_h, \tag{3.28}$$

$$\eta_E^2 := h_E \|[\![\frac{\partial^2 u_h}{\partial \boldsymbol{n}^2}]\!]_E\|_{0,E}^2 + h_E^3 \|[\![\frac{\partial}{\partial \boldsymbol{n}} \Delta u_h]\!]_E\|_{0,E}^2, \quad E \in \mathcal{E}_h^\Omega. \tag{3.29}$$

The consistency error is given by

$$\inf_{v_h \in V_h^c} a_h^{IP}(u_h - v_h, u_h - v_h). \tag{3.30}$$

Here, $V_h^c \subset H_0^2(\Omega)$ denotes a C^1 conforming finite element space used for conforming approximations as mentioned in section 3.1. Such a space can be built using the so-called Argyris elements described in [AFS68]. Another possibility is to construct a posteriori a conforming approximation using the enrichment operator $E_h : V_h \to V_h^c$ presented in [BS05]. Let p be a nodal point of V_h^c and let us further define the associated patch of triangles ω_h^p,

$$\omega_h^p := \bigcup \{T \in \mathcal{T}_h(\Omega) \mid \{p\} \cap \mathcal{N}_h(T) \neq \emptyset\}. \tag{3.31}$$

Now, the value $N(E_h v_h)$ of any nodal variable of $E_h v_h$ at the nodal point p is defined by averaging over the patch ω_h^p, i.e.

$$N(E_h v_h) := |\omega_h^p|^{-1} \sum_{T \in \omega_h^p} (|T| \; N(v_h|_T)), \quad v_h \in V_h. \tag{3.32}$$

According to the mapping properties of E_h shown in [BS05], there exists a constant $C_{nc} > 0$ depending only on the local geometry of $\mathcal{T}_h$ such that

$$\begin{aligned} \inf_{v_h \in V_h^c} a_h^{IP}(u_h - v_h, u_h - v_h) &\leq a_h^{IP}(u_h - E_h(u_h), u_h - E_h(u_h)) \\ &\leq C_{nc} \eta_{h,c}^2, \end{aligned} \tag{3.33}$$

where the consistency error related estimator $\eta_{h,c}$ is given by

$$\eta_{h,c} := \Big(\sum_{E \in \mathcal{E}_h} \eta_{E,c}^2 \Big)^{1/2}, \quad \eta_{E,c}^2 := h_E^{-1} \| [\![\frac{\partial u_h}{\partial \boldsymbol{n}}]\!]_E \|_{0,E}^2. \tag{3.34}$$

Together with our previously defined estimators (3.27) – (3.29) we get the following reliability result [FHP14]:

Theorem 3.1. *Let $u \in V$ and $u_h \in V_h$ be the unique solution of* (3.3) *and* (3.19)*, and let η_h and $\eta_{h,c}$ be given by* (3.27) – (3.29) *and* (3.34)*. Then, there exists a constant $C_r > 0$, depending only on the local geometry of $\mathcal{T}_h$ and on k, such that*

$$a_h^{IP}(u - u_h, u - u_h) \leq C_r \Big(\eta_h^2 + \alpha \eta_{h,c}^2 \Big). \tag{3.35}$$

For sufficiently large penalty parameter α it can be shown that $\alpha \eta_{h,c}^2$ is bounded by η_h^2 [FHP14].

Theorem 3.2. *Let η_h and $\eta_{h,c}$ be given by* (3.27) – (3.29) *and* (3.34)*. Then, there exists a constant $C_J > 0$, depending only on the shape regularity of $\mathcal{T}_h$ and on k, such that for $\alpha \geq 2C_J/\gamma$ there holds*

$$\alpha \eta_{h,c}^2 \leq 2 \frac{C_J}{\gamma} \eta_h^2. \tag{3.36}$$

Finally, this results in the improved reliability [FHP14]:

Corollary 3.3. *Let $u \in V$ and $u_h \in V_h$ be the unique solution of* (3.3) *and* (3.19)*, and let η_h be the residual error estimator as given by* (3.27) – (3.29)*. Then, there holds*

$$a_h^{IP}(u - u_h, u - u_h) \leq C_R \eta_h^2, \tag{3.37}$$

where $C_R := C_r(1 + 2\gamma^{-1} C_J)$.

3.2.2 Contraction Property

A convergence analysis for conforming discretizations of the Poisson equation was first performed by [Dör96]. In this context, we also have to mention the salient achievements shown by [CKNS08]. For nonconforming discretizations based on the lowest order Crouzeix–Raviart elements we refer to [CH06]. In the spirit of the results on a convergence analysis for Interior Penalty Discontinuous Galerkin (IPDG) methods presented by [BN10], our goal is to demonstrate a contraction property. More precisely, we show that the discretization error in the $a_h^{IP}(\cdot,\cdot)$-induced norm together with its estimator on a fine mesh $\mathcal{T}_h$ can be bounded from above by their values on the antecedent and coarser mesh $\mathcal{T}_H$.

For adaptive mesh refinement we use Dörfler marking, see [Dör96] using the error estimator η_h

$$\eta_h = \Big(\sum_{T \in \mathcal{T}_h(\Omega)} \hat{\eta}_T^2 \Big)^{1/2}, \tag{3.38}$$

with element residuals $\hat{\eta}_T$

$$\begin{aligned} \hat{\eta}_T^2 := h_T^4 \| f - \Delta^2 u_h \|_{0,T}^2 + \frac{1}{2} \sum_{E \in \mathcal{E}_h(\partial T \cap \Omega)} \Big(h_E \| [\![\frac{\partial^2 u_h}{\partial \boldsymbol{n}^2}]\!]_E \|_{0,E}^2 \\ + h_E^3 \| [\![\frac{\partial}{\partial \boldsymbol{n}} \Delta u_h]\!]_E \|_{0,E}^2 \Big). \end{aligned} \tag{3.39}$$

For a constant $0 < \Theta < 1$, we put the worst elements $T \in \mathcal{T}_h$, i.e. the triangles T with highest values of $\hat{\eta}_T$, into the set $\mathcal{M}$ until there holds

$$\Theta \, \eta_h^2 \leq \sum_{T \in \mathcal{M}} \hat{\eta}_T^2. \tag{3.40}$$

Once we have chosen such a set $\mathcal{M}$ the elements therein are refined by newest vertex bisection. In doing so, we have to guarantee certain conditions given in [CKNS08, BN10].

As a first step, we show quasi-orthogonality of our C^0-IPDG method using the following mesh perturbation result [FHP14].

Lemma 3.4. *Let $\mathcal{T}_h$ be a simplicial triangulation obtained by the aforementioned refinement of $\mathcal{T}_H$. Then, there exists a constant $C_P > 0$, depending only on the local geometry of the triangulations and on k, such that for any $\varepsilon > 0$ and $v \in V + V_H$ there holds*

$$a_h^{IP}(v,v) \leq (1+\varepsilon)\ a_H^{IP}(v,v) + \frac{C_P}{\gamma\varepsilon}\Big(\eta_{h,c}^2 + \eta_{H,c}^2\Big). \tag{3.41}$$

Such mesh perturbation results play an essential role in the convergence analysis to derive quasi-orthogonality results, e.g. [BN10, HKW09, KP07]. To get quasi-orthogonality in our case, we further have to use the following result demonstrated in [FHP14] for the conforming approximations $u_H^c \in V_H^c, u_h^c \in V_h^c$ of (3.3) given by

$$a(u_H^c, v_H^c) = (f, v_H^c), \quad v_H^c \in V_H^c, \tag{3.42}$$

$$a(u_h^c, v_h^c) = (f, v_h^c), \quad v_h^c \in V_h^c. \tag{3.43}$$

Lemma 3.5. *Let $\mathcal{T}_h$ be a simplicial triangulation obtained by the aforementioned refinement of $\mathcal{T}_H$, and let $u_h \in V_h,\ u_H \in V_H$ and η_h, η_H be the C^0-IPDG solutions of* (3.19) *and error estimators, respectively. Moreover, let $u_h^c \in V_h^c$ and $u_H^c \in V_H^c$ be the conforming approximations of* (3.3) *according to* (3.42) – (3.43)*. Then, for $u_h^{nc} := u_h - u_h^c$ and $u_H^{nc} := u_H - u_H^c$ there holds*

$$\|u_h^{nc} - u_H^{nc}\|_{2,h,\Omega}^2 \leq \frac{4\ C_J C_{nc}}{\gamma^2\alpha}\Big(\eta_h^2 + \eta_H^2\Big), \tag{3.44}$$

where C_{nc} and C_J are the constants from (3.33) *and* (3.36)*.*

Using this result, we get quasi-orthogonality [FHP14].

Theorem 3.6. *Let $\mathcal{T}_h$ be a simplicial triangulation obtained by the aforementioned refinement of $\mathcal{T}_H$, and let $u_h \in V_h,\ u_H \in V_H$ and η_h, η_H be the associated C^0-IPDG solutions of* (3.19) *and error estimators, respectively. Further, let $e_h := u - u_h$ and $e_H := u - u_H$ be the fine and coarse mesh errors. Then, for any $0 < \varepsilon < 1$ there exists a constant $C_Q > 0$, depending on $\gamma, C_1, C_J, C_{nc}, C_P$, such that there holds*

$$\begin{aligned} a_h^{IP}(e_h,e_h) \leq (1+\varepsilon)\ a_H^{IP}(e_H,e_H) - \frac{\gamma}{2}\|u_h - u_H\|_{2,h,\Omega}^2 \\ + \frac{C_Q}{\alpha\varepsilon}\Big(\eta_h^2 + \eta_H^2\Big). \end{aligned} \tag{3.45}$$

As a final element for the contraction property we have to state an estimator reduction property [FHP14].

Lemma 3.7. *Let $\mathcal{T}_h$ be a simplicial triangulation obtained by the aforementioned refinement of $\mathcal{T}_H$, let $u_h \in V_h, u_H \in V_H$, and η_h, η_H be the associated C^0-IPDG solutions and error estimators, respectively, and let $\Theta > 0$*

be the universal constant from (3.40)*. Then, for any* $\tau > 0$ *there exists a constant* $C_\tau > 1$*, depending only on the local geometry of the triangulations and on* k*, such that for* $\kappa(\Theta) := (1+\tau)(1-2^{-1/2})\Theta$ *there holds*

$$\eta_h^2 \leq \kappa(\Theta)\ \eta_H^2 + C_\tau \|u_h - u_H\|_{2,h,\Omega}^2. \tag{3.46}$$

Then the contraction property is derived by combining the estimator reduction property (3.46), the quasi-orthogonality (3.45), and the reliability (3.37), see [FHP14].

Theorem 3.8. *Let* $u \in H_0^2(\Omega)$ *be the unique weak solution of* (3.3)*. Further, let* $\mathcal{T}_h$ *be a simplicial triangulation obtained by the afore-mentioned refinement of* $\mathcal{T}_H$*, and let* $u_h \in V_h$*,* $u_H \in V_H$ *and* η_h, η_H *be the* C^0*-IPDG solutions of* (3.19) *and error estimators, respectively. Then, there exist constants* $0 < \delta < 1$ *and* $\rho > 0$*, depending only on the local geometry of the triangulations, the parameter* Θ *from the Dörfler marking, and on* k*, such that for sufficiently large penalty parameter* α *the fine mesh and coarse mesh discretization errors* $e_h := u - u_h$ *and* $e_H = u - u_H$ *satisfy*

$$a_h^{IP}(e_h, e_h) + \rho\ \eta_h^2 \leq \delta\Big(a_H^{IP}(e_H, e_H) + \rho\ \eta_H^2\Big). \tag{3.47}$$

3.2.3 Numerical Results

We implemented the presented C^0-IPDG AFEM using the programming language *Python* [vRdB91] and different libraries, particularly *NumPy* and *SciPy* [Oli07], *FEniCS* [LMWea12] and *matplotlib* [Hun07]. The numerical performance of the improved adaptive C^0-IPDG method is demonstrated for polynomial degrees $2 \leq k \leq 6$ using the following example taken from [BGS10]:

Let $\Omega := (-1,+1)^2 \setminus ([0,1) \times (-1,0])$ be a bounded L-shaped domain and let further f be the right hand-side of the biharmonic problem (3.1) – (3.2) such that $u(r,\varphi)$ is the exact solution (in polar coordinates) given by

$$u(r,\varphi) = \Big(r^2\cos^2\varphi - 1\Big)^2\Big(r^2\sin^2\varphi - 1\Big)^2 r^{1+z} g(\varphi), \tag{3.48}$$

with

$$\begin{aligned} g(\varphi) := \Big(\frac{1}{z-1}\sin(\frac{3(z-1)\pi}{2}) - \frac{1}{z+1}\sin(\frac{3(z+1)\pi}{2})\Big) \\ \cdot\Big(\cos((z-1)\varphi) - \cos((z+1)\varphi)\Big) \\ -\Big(\frac{1}{z-1}\sin((z-1)\varphi) - \frac{1}{z+1}\sin((z+1)\varphi)\Big) \\ \cdot\Big(\cos(\frac{3(z-1)\pi}{2}) - \cos(\frac{3(z-1)\pi}{2})\Big), \end{aligned} \tag{3.49}$$

where $z \approx 0.54448$ is a non-characteristic root of

$$\sin^2(\frac{3z\pi}{2}) = z^2 \sin^2(\frac{3\pi}{2}). \tag{3.50}$$

In this context we note that the computation of the residuals is delicate for elements having the origin, the singularity of the problem, as a vertex. The numerical integration is not trivial for such elements. However, the collapsed Gauss–Jacobian-type quadrature formula from [KS99] provides good results.

The penalty parameter α directly influences the numerical solution of our problem. This is a standard observation for IPDG methods. However, the rule $\alpha = 2.5(k+1)^2$ provides stability, and the descent slopes of the error shows optimal convergence rates for any polynomial degree. Concerning a priori optimal convergence rates suggested by [BS05] for $h_T := \operatorname{diam}(T)$, $T \in \mathcal{T}_h$, there holds

$$a_h^{IP}(u-u_h, u-u_h)^{1/2} \lesssim \Big(\sum_{T\in\mathcal{T}_h} h_T^{2\min(\alpha(T),k-1)} |u|^2_{2+\alpha(T),T} \Big)^{1/2}, \tag{3.51}$$

where $\alpha(T)$, $T \in \mathcal{T}_h$, is the local index of elliptic regularity. Now for elements T having a vertex at the origin we get $\min(\alpha(T), k-1) = z \approx 0.544$ and for elements elsewhere, we get $\min(\alpha(T), k-1) = k-1$. Thus, the optimal convergence rates for $k = 2$, 4 and 6 are slightly below 0.5, 1.5 and 2.5. In Figure 3.1, the convergence histories show these optimal convergence rates to be asymptotically achieved by the adaptive algorithm. In addition to this, we see that the Dörfler marking related parameter Θ influences the convergence rates, just as it does in the case of other IPDG methods for second order elliptic boundary value problems [HKW09] and H-IPDG methods for Maxwell's equations [CHSW11]. The increased convergence rates for higher polynomial degrees are reflected in the enhanced resolution of the singularity located at the reentrant corner of the domain Ω by the adaptively refined meshes shown in Figure 3.2.

Further, in Figure 3.3 we can see the reduction of the estimator as proposed by Lemma 3.7. However, we see in Figure 3.4 that the computed effectivity indices increase for higher polynomial degrees.

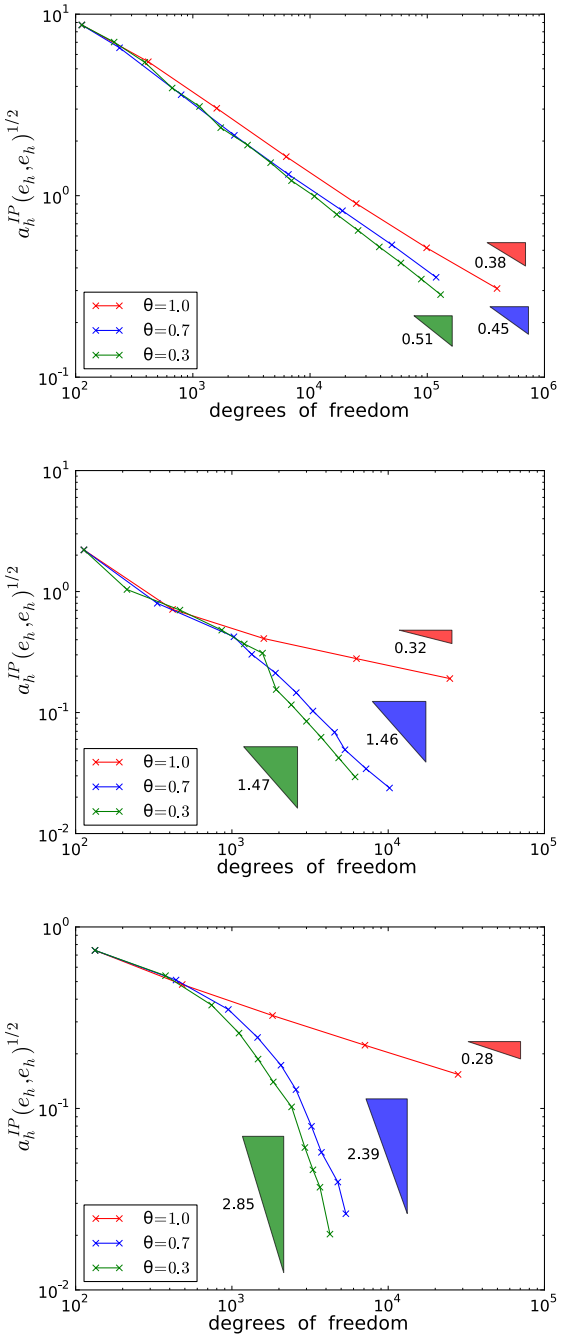

Figure 3.1: Convergence histories in terms of the bilinear form $a_h^{IP}(\cdot,\cdot)$ induced norm of the error $a_h^{IP}(u-u_h,u-u_h)^{1/2}$ as a function of the total number of degrees of freedom (DOF) on a double logarithmic scale for uniform refinement and adaptive refinement with $\Theta = 0.7$ and $\Theta = 0.3$ in the Dörfler marking for $k = 2$ (top), 4 (middle) and 6 (bottom). [FHP14]

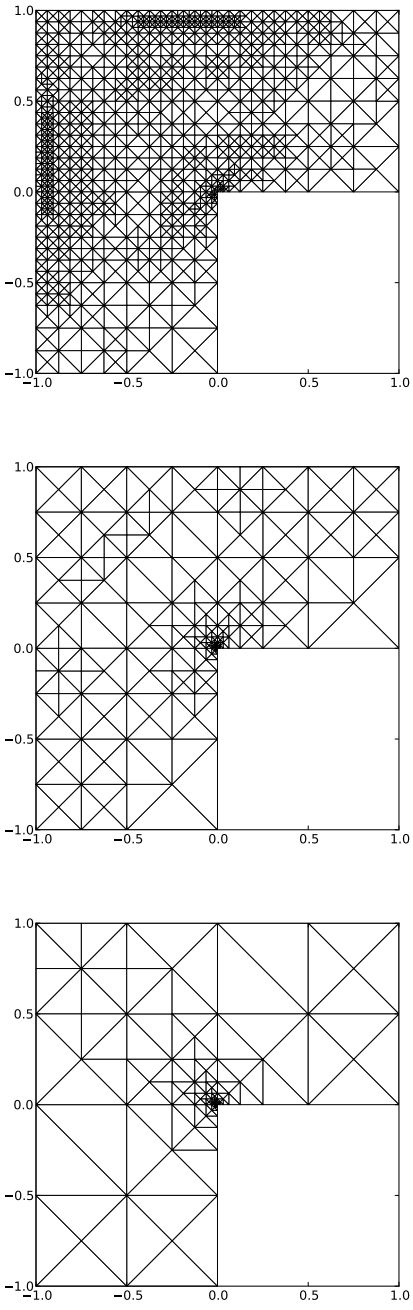

Figure 3.2: Adaptive refined meshes after 10 cycles with $\Theta = 0.3$ in the Dörfler marking for $k = 2$ (top), 4 (middle) and 6 (bottom). [FHP14]

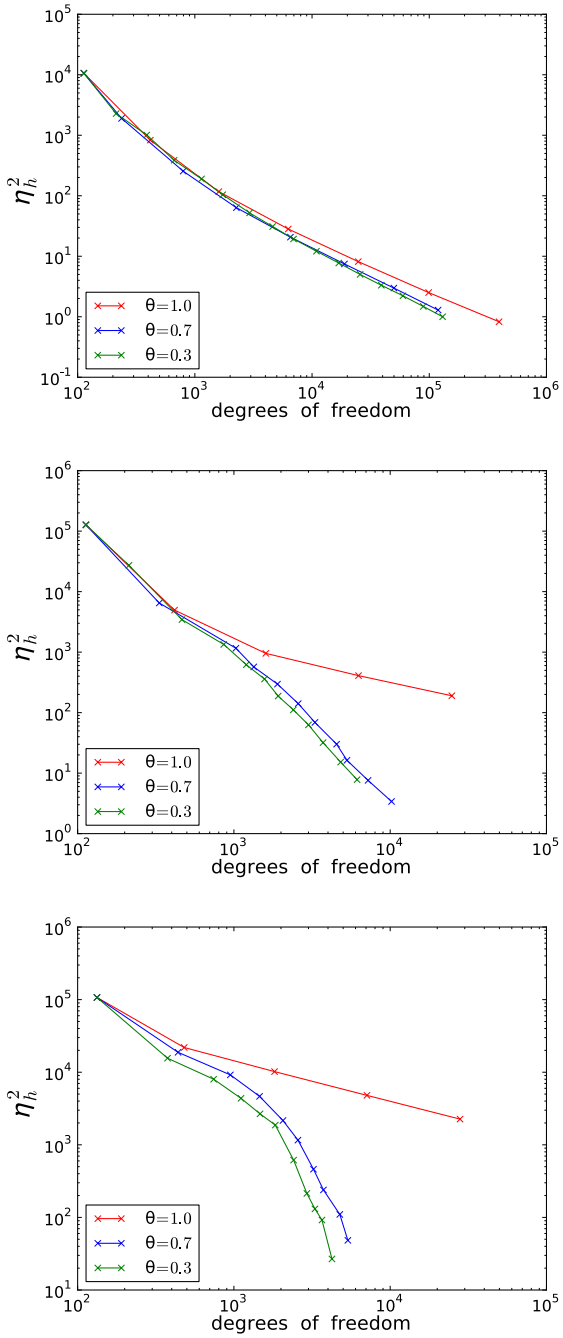

Figure 3.3: Estimator reduction as a function of the total number of degrees of freedom (DOF) on a double logarithmic scale for uniform refinement and adaptive refinement with $\Theta = 0.7$ and $\Theta = 0.3$ in the Dörfler marking for $k = 2$ (top), 4 (middle) and 6 (bottom). [FHP14]

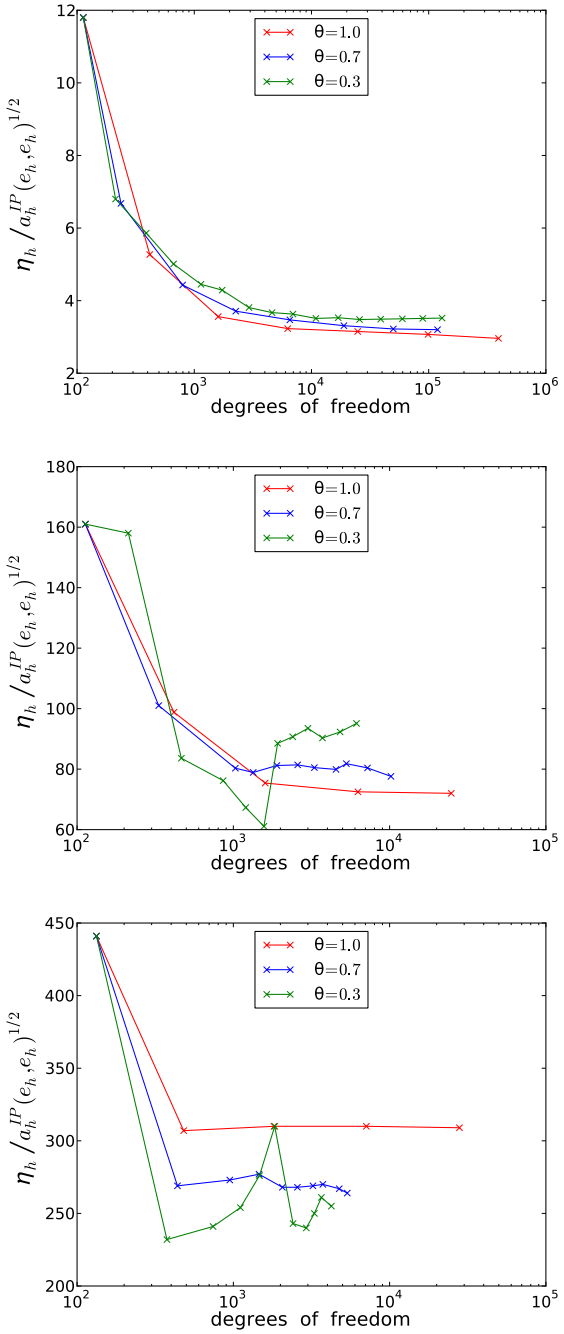

Figure 3.4: Effectivity indices $\eta_h / a_h^{IP}(u - u_h, u - u_h)^{1/2}$ as a function of the total number of degrees of freedom (DOF) on a logarithmic scale for uniform refinement and adaptive refinement with $\Theta = 0.7$ and $\Theta = 0.3$ in the Dörfler marking for $k = 2$ (top), 4 (middle) and 6 (bottom). [FHP14]

3.3 Application to the Cahn–Hilliard Equation

The biharmonic problem (3.1) – (3.2) and the Cahn–Hilliard equation (2.36) – (2.37) have fourth order derivatives. Analogous to the biharmonic problem in section 3.1, there exist conforming approximations using C^1 finite elements [EZ86, EF89] or, respectively, mixed finite element methods [BF91] for discretization with corresponding drawbacks. Consequently, we introduce a C^0-IPDG method for the Cahn–Hilliard equation (2.36) – (2.37) in the spirit of [WKG06]. Let us recall the biharmonic problem,

$$\Delta^2 u = f \quad \text{in } \Omega, \tag{3.52}$$

$$u = \frac{\partial u}{\partial \boldsymbol{n}} = 0 \quad \text{on } \Gamma. \tag{3.53}$$

Further, we defined the standard C^0 Lagrange finite element space V_h according to

$$V_h := \{v_h \in C_0^0(\Omega) \mid v_h|_T \in P_k(T),\ T \in \mathcal{T}_h\}. \tag{3.54}$$

Using the mesh-dependent bilinear form $a_h^{IP}(\cdot,\cdot) : V_h \times V_h \to \mathbb{R}$ defined by

$$\begin{aligned} a_h^{IP}(u_h, v_h) := &\sum_{T\in\mathcal{T}_h} (D^2 u_h, D^2 v_h)_{0,T} + \sum_{E\in\mathcal{E}_h^{\bar{\Omega}}} (\{\!\{\frac{\partial^2 u_h}{\partial \boldsymbol{n}^2}\}\!\}, [\![\frac{\partial v_h}{\partial \boldsymbol{n}}]\!])_{0,E} \\ &+ \sum_{E\in\mathcal{E}_h^{\bar{\Omega}}} ([\![\frac{\partial u_h}{\partial \boldsymbol{n}}]\!], \{\!\{\frac{\partial^2 v_h}{\partial \boldsymbol{n}^2}\}\!\})_{0,E} + \alpha \sum_{E\in\mathcal{E}_h^{\bar{\Omega}}} h_E^{-1} ([\![\frac{\partial u_h}{\partial \boldsymbol{n}}]\!], [\![\frac{\partial v_h}{\partial \boldsymbol{n}}]\!])_{0,E}. \end{aligned} \tag{3.55}$$

the C^0-IPDG approximation of the biharmonic problem (3.52) – (3.53) is to find a $u_h \in V_h$ such that

$$a_h^{IP}(u_h, v_h) = (f, v_h)_{0,\Omega}, \quad v_h \in V_h. \tag{3.56}$$

Now we adapt this result to the Cahn–Hilliard equation (2.36) – (2.37),

$$\frac{\partial c}{\partial t} = \nabla \cdot M_D \nabla (f'(c) - \epsilon^2 \Delta c) \quad \text{in } \Omega, \tag{3.57}$$

$$\frac{\partial c}{\partial \boldsymbol{n}} = \frac{\partial}{\partial \boldsymbol{n}} (f'(c) - \epsilon^2 \Delta c) = 0 \qquad \text{on } \Gamma. \tag{3.58}$$

Here we also assume constant mobility $M_D = D$. Different from the biharmonic problem (3.52) – (3.53), we have boundary conditions allowing nonzero concentrations. Therefore we introduce a modified C^0 Lagrange finite element space W_h

$$W_h := \{v_h \in C^0(\Omega) \mid v_h|_T \in P_k(T),\ T \in \mathcal{T}_h\}. \tag{3.59}$$

We discretize the fourth order terms of the Cahn–Hilliard equation (3.57) – (3.58) by the bilinear form $a_h^{IP}(\cdot,\cdot) : W_h \times W_h \to \mathbb{R}$ defined by (3.55). Further, we define a nonlinear form $b_h(\cdot,\cdot) : W_h \times W_h \to \mathbb{R}$,

$$b_h(c_h, w_h) := (\nabla f'(c_h), \nabla w_h)_{0,\Omega}. \tag{3.60}$$

The C^0-IPDG approximation is to find a solution $c_h \in W_h$, such that

$$-M_D^{-1}(\frac{dc_h}{dt}, w_h)_{0,\Omega} = \epsilon^2 a_h^{IP}(c_h, w_h) + b_h(c_h, w_h), \quad w_h \in W_h. \tag{3.61}$$

Assuming constant mobility note that the bilinear form is the same even for the different boundary conditions.

We discretize the resulting C^0-IPDG approximation (3.61) in time using the backward Euler scheme. Let $[0,T]$, $T \in \mathbb{R}^+$, be the time interval and let us introduce a time step size $\tau := T/N_\tau$, $N_\tau \in \mathbb{N}$. The concentration at time $t = n_\tau \tau$, $0 \le n_\tau \le N_\tau$, is denoted by $c_h^{n_\tau} \in W_h$. Given a concentration $c_h^{n_\tau}$, $0 \le n_\tau \le N_\tau - 1$, we compute the concentration $c_h^{n_\tau+1}$ by solving the nonlinear equation

$$-(M_D\tau)^{-1}(c_h^{n_\tau+1} - c_h^{n_\tau}, w_h)_{0,\Omega} = \epsilon^2 a_h^{IP}(c_h^{n_\tau+1}, w_h) + b_h(c_h^{n_\tau+1}, w_h) \tag{3.62}$$

for all $w_h \in W_h$.

Further, we introduce an algebraic version of the nonlinear approximation (3.62). Let V_h be spanned by the standard Lagrange basis functions $\phi_h^{n_h}$, $1 \le n_h \le N_h$, where $N_h \in \mathbb{N}$ denotes the number of degrees of freedom of W_h. Then the linear mass and stiffness matrices $\boldsymbol{M}(\tau), \boldsymbol{A} \in \mathbb{R}^{N_h \times N_h}$ are defined by

$$\boldsymbol{M}(\tau)_{ij} := -(M_D\tau)^{-1}(\phi_h^i, \phi_h^j)_{0,\Omega}, \quad 1 \le i,j \le N_h, \tag{3.63}$$

$$\boldsymbol{A}(\epsilon)_{ij} := \epsilon^2 a_h^{IP}(\phi_h^i, \phi_h^j), \quad 1 \le i,j \le N_h, \tag{3.64}$$

with corresponding vector $\boldsymbol{c}^{n_\tau} \in \mathbb{R}^{N_h}$ for the concentration $c_h^{n_\tau}$. Thereby, the entry $\boldsymbol{c}_{n_h}^{n_\tau}$ is connected to $\phi_h^{n_h}$, $1 \le n_h \le N_h$, such that

$$c_h^{n_\tau} = \sum_{n_h=1}^{N_h} \boldsymbol{c}_{n_h}^{n_\tau} \phi_h^{n_h}. \tag{3.65}$$

In addition to this, we define the nonlinear mapping $\boldsymbol{B} : \mathbb{R}^{N_h} \to \mathbb{R}^{N_h}$, such that

$$\boldsymbol{B}_i(\boldsymbol{c}^{n_\tau}) := b_h(c_h^{n_\tau}, \phi_h^i) = (\nabla f'(c_h^{n_\tau}), \nabla \phi_h^i)_{0,\Omega}, \quad 1 \le i \le N_h. \tag{3.66}$$

Then the algebraic form of the nonlinear equation (3.62) is given by

$$\boldsymbol{M}(\tau)\boldsymbol{c}^{n_\tau+1} - (\boldsymbol{A}(\epsilon)\boldsymbol{c}^{n_\tau+1} + \boldsymbol{B}(\boldsymbol{c}^{n_\tau+1})) = \boldsymbol{M}(\tau)\boldsymbol{c}^{n_\tau}. \tag{3.67}$$

Aiming at a Newton method, we introduce the nonlinear function $\boldsymbol{G}^{n_\tau+1} : \mathbb{R}^{N_h} \to \mathbb{R}^{N_h}$ depending on a given concentration $\boldsymbol{c}_h^{n_\tau}$ such that

$$\boldsymbol{G}^{n_\tau+1}(\boldsymbol{c}) = \boldsymbol{M}(\tau)\boldsymbol{c} - \big(\boldsymbol{A}(\epsilon)\boldsymbol{c} + \boldsymbol{B}(\boldsymbol{c})\big) - \boldsymbol{M}(\tau)\boldsymbol{c}^{n_\tau}. \tag{3.68}$$

Now solving the nonlinear algebraic system (3.67) for $\mathbf{c}^{n_\tau+1}$ corresponds to finding a root $\boldsymbol{c} \in \mathbb{R}^{N_h}$ of $\boldsymbol{G}^{n_\tau+1}$. Therefore we have to solve the nonlinear algebraic system

$$\boldsymbol{G}^{n_\tau+1}(\boldsymbol{c}) = 0. \tag{3.69}$$

This system is solved by an ordinary Newton method. We denote the Newton iterates by $\boldsymbol{c}^{(k)} \in \mathbb{R}^{N_h}$, $k \in \mathbb{N}_0$, and take the previous solution $\boldsymbol{c}^{(0)} = \mathbf{c}^{n_\tau}$ as an initial guess. Then the solution $\boldsymbol{c}^{n_\tau+1}$ of the nonlinear system (3.67) is given by iteration according to

$$\mathbf{G}'(\boldsymbol{c}^{(k)})\Delta\boldsymbol{c}^{(k)} = -\mathbf{G}^{n_\tau+1}(\boldsymbol{c}^{(k)}, \tau), \tag{3.70}$$

$$\boldsymbol{c}^{(k+1)} = \boldsymbol{c}^{(k)} + \Delta\boldsymbol{c}^{(k)}. \tag{3.71}$$

The Jacobian $\boldsymbol{G'}(\boldsymbol{c}^{(k)}) \in \mathbb{R}^{N_h \times N_h}$ is given by

$$\boldsymbol{G}'(\boldsymbol{c}^{(k)}) = \boldsymbol{M}(\tau) - \big(\boldsymbol{A}(\epsilon) + \boldsymbol{B}'(\boldsymbol{c}^{(k)})\big), \tag{3.72}$$

where $\boldsymbol{B}'(\boldsymbol{c}^{(k)})$ denotes the Jacobian of $\boldsymbol{B}(\boldsymbol{c}^{(k)})$. The resulting iteration is performed until a given tolerance is reached. Thereby, the Jacobian (3.72) is computed automatically by a computer algebra system. Details about the software used for this task are given in section 5.1.

The choice of the initial guess $\boldsymbol{c}^{(0)}$ and of the time step size τ is important for the convergence of the Newton method (3.70) – (3.71). This especially holds true in the very beginning of the simulation, when nonlinear terms of the local free energy dominate the Cahn–Hilliard equation (3.57) – (3.58). This behavior is discussed in section 2.1. However, similarly to [HL12], we expect the existence of upper bounds for the time step size τ, so that our previously derived Newton method (3.70) – (3.71) converges. Such a result would allow us to set maximum time step sizes without loss of stability. Furthermore, we already presented an adaptive C^0-IPDG method in space for the biharmonic problem (3.52) – (3.53) in section 3.2. We use the same bilinear form $a_h^{IP}(\cdot,\cdot)$ for fourth order terms in the Cahn–Hilliard equation (3.57) – (3.58). These terms are connected to the lipid phases boundaries as described in section 2.1. An adaptive method with respect to the boundaries would reduce computational efforts, because the boundaries reduce over time. For this purpose the additional nonlinear terms have to be taken into account. This complex analysis goes beyond the scope of this thesis and is left for future research.

Chapter 4

Image Processing

We have to find methods that allow us to compare experiments and simulations not only in a qualitative but also in a quantitative sense. Therefore, in section 4.1 we begin by discussing relevant properties of phase separation and possibilities for their measurement. Afterwards, in section 4.2 we explain the most promising attempt, the structure factor method. Using this method, we address practical issues in section 4.3.

4.1 Quantitative Measurements

Data from experiments and simulation are given as series of images. At first glance, we see obvious qualitatively different processes of phase separation, like binodal and spinodal decomposition, as described in section 1.2. Such qualitative differences can be determined by the observer. But for further details, we have to evaluate images not only in a qualitative but also in a quantitative sense. For this purpose, we discuss an exemplary set of gray value images, shown in Figure 4.1, to determine interesting details and possibilities for their quantitative measurements. This series starts with an almost homogeneous grey image, indicating virtually mixed phases. Afterwards, we observe decomposition of the initial distribution into distinct black and white regions. At the same time, the structures initially appear to be of a certain size and form. In the next images, we see how these structures further coarsen over time by collision and diffusion.

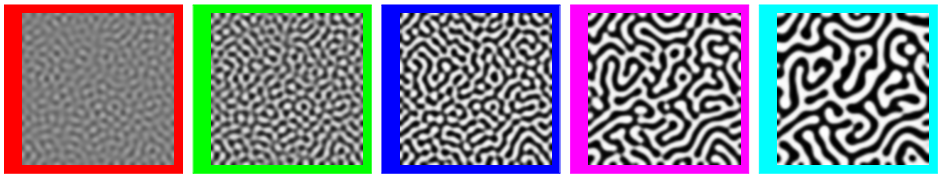

Figure 4.1: Series of images showing spinodal decomposition.

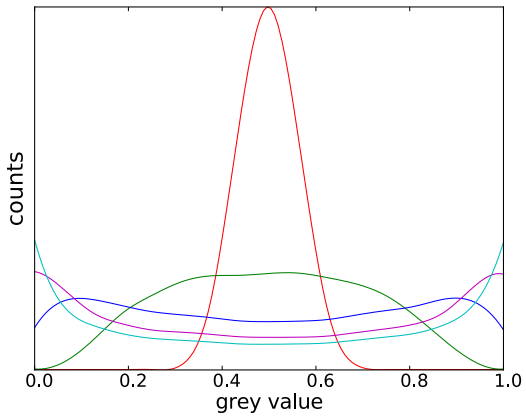

Figure 4.2: Histograms of grey values (0/1 equals black/white) related to the series of images as displayed in Figure 4.1.

Throughout this process, we are interested in the development of structures. Here, we are especially interested in how long the formation of initial structures takes and how fast the resulting domains grow in time. Therefore, we discuss two methods used in [Lei08] for exemplary series of experimental images. Our method of choice for image processing underlies certain restrictions. On one hand, it has to be numerically efficient, but on the other hand, it has to give interpretable results. Only such a method is able to evaluate extensive amounts of image data in a time-efficient and user-friendly way.

One possibility for quantitative measurement is to observe the development of the grey values over time. Therefore, we perform histograms of image pixel values as shown for the afore-mentioned exemplary series of images in Figure 4.2. Starting from an almost homogeneous mixture, we only have contributions from a small range of grey value. When separation sets in, we see different forms of distributions over time until there are almost exclusively black and white pixels left in the image. After separation, only smooth phase transitions give contributions to intermediate values. This method can automatically be applied to a series of images at a reasonable numerical effort. But we have to ensure certain quality standards for experimental image series, especially when we compare different series of experimental images. Here, the camera may not perform auto corrections regarding brightness and contrast. Ideally, brightness and contrast are fixed and normalized over time for all experiments, in order to prevent shifts or jumps in the histogram. In practice, however, this can not be guaranteed due to various technical difficulties. Even if this was possible, the method would only give us reliable information until the phases separated and would lack to measure domain sizes.

When we consider domain sizes as another possibility for measurement,

we have to specify this quantity. In case of binodal decomposition, as described in section 1.2, the domains size is obviously given by the diameter of the circular shape. Their manual measurement may be acceptable for a small number of images and domains. However, manual measurements are influenced by subjective criteria, for example, where to draw the phase boundary due to the smooth phase transitions. Even if this problem was solved there still would be the case of spinodal decomposition. Here it is hard to define a practicable value for the size of interconnected domains. Consequently, we look for a method performing automatic, objective, comparable measurements of domain sizes for lipid decomposition in experiments and simulations under the restriction of numerical efficiency. For this purpose, we present the structure factor method in the following section. The method analyses images with regard to their mean structure size reflecting the actual domain sizes. Issues of application are described later in section 4.3.

4.2 Structure Factor

The structure factor is a common method for measurements of structures in X-ray scattering experiments. As a general source of information we refer to [Gui63]. The method needs Fourier transformed image data. The Fourier transformation $\hat{f}$ at point $\xi \in \mathbb{R}$ of a continuous scalar function f is defined by

$$\hat{f}(\xi) := \int_{-\infty}^{+\infty} f(x) e^{-2\pi i x \xi} \, \mathrm{d}x, \tag{4.1}$$

whereas its backward transformation is given by

$$f(x) := \frac{1}{2\pi} \int_{-\infty}^{+\infty} \hat{f}(\xi) e^{-2\pi i x \xi} \, \mathrm{d}\xi. \tag{4.2}$$

From here on until the end of this section i denotes the imaginary unit.

However, in our case we have digital images in experiments and simulation, which means the images consist of discrete points called pixels. Therefore, we have to apply a *discrete Fourier transformation* (DFT) in order to apply this method. DFT is a demanding task concerning computational costs. Consequently, we have to reduce these costs when analyzing a series of images. Therefore, we use the *Fast Fourier Transformation* (FFT), an optimized version of the DFT regarding numerical efforts. For simplicity we describe the structure factor method using DFT. For more details on DFT and FFT we refer to [BH95]. Despite this fact, our description is close to our implementation used for evaluation of images resulting from experiment and simulation presented in the subsequent chapter 5.

Let Ω be a square domain of given side length l representing a subset of

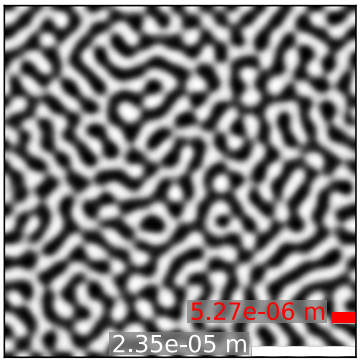

Figure 4.3: Exemplary image showing spinodal decomposition with scale bar (white) and its mean wavelength (red).

the lipid membrane either in experiment or simulation, such that

$$\Omega := \{(x_1, x_2) \in \mathbb{R}^2 \mid -\frac{l}{2} \leq x_j \leq +\frac{l}{2},\ 1 \leq j \leq 2\}. \tag{4.3}$$

Here, we neglect the absolute position of the domain, because we assume the process of decomposition to be uniform in the membrane. Further, we assume our domain Ω to be flat even for experimental images. This is a simplification regarding lipid vesicles described in section 1.2. But their curvature can be neglected in our case when we assume the evaluated domain Ω to be small compared to the vesicles surface. An exemplary mixture of lipid phases showing spinodal decomposition is given in Figure 4.3. This image will be further used for demonstration purposes of the following steps.

Optoelectronical observation or simulation of the given domain Ω results in digital image data. This data is a discrete set of grey values representing a certain mixture of lipid phases. More precisely, we introduce a discretization of our domain Ω. Here, we assume our image to have equal spatial resolution. Thus, we define a uniform grid spacing $\Delta x = l/n$, $n = 2^N$, $N \in \mathbb{N}$, and get the following set of grid points:

$$\begin{aligned} \Omega_h := \{(x_{l_1}, x_{l_2}) \in \mathbb{R}^2 \mid x_{l_j} = l_j \Delta x,\ l_j \in \mathbb{Z}, \\ -\frac{n}{2} + 1 \leq l_j \leq \frac{n}{2},\ j = 1, 2\}. \end{aligned} \tag{4.4}$$

This defines a chessboard structure in our domain Ω illustrated in the image of Figure 4.4. The resulting chess squares are called pixels $p_{l_1 l_2}$, $-n/2+1 \leq l_1, l_2 \leq n/2$. Their number is a power of 2, because we have chosen $n = 2^N$. The area $\sigma_{l_1 l_2}$ of the domain Ω covered by the pixel $p_{l_1 l_2}$ is defined by

$$\boldsymbol{\sigma}_{l_1 l_2} := \{(x_1, x_2) \in \mathbb{R}^2 \mid 0 \leq x_j - x_{l_j} \leq \Delta x,\ j = 1, 2\}. \tag{4.5}$$

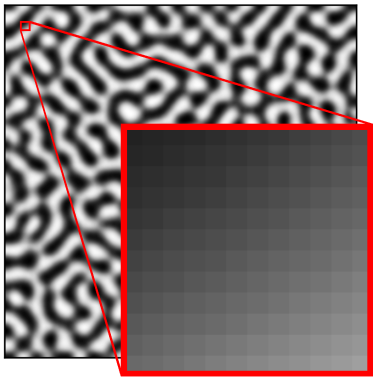

Figure 4.4: Enlarged selection of the exemplary image shown in Figure 4.3 revealing the discrete nature of the digital image.

Our defined pixels $p_{l_1 l_2}$ admit 8-bit grey values which means $0 \leq p_{l_1 l_2} \leq 255$, $p_{l_1 l_2} \in \mathbb{N}_0$. Here, the values 0 and 255 represent black and white, i.e. pure lipid phases. Consequently, we define a digital image P as an ordered two-dimensional set of $n \times n$ pixels, such that

$$\mathcal{P} := (p_{l_1 l_2})_{l_1, l_2 = -n/2+1}^{n/2}. \tag{4.6}$$

A corresponding discretization of our exemplary image shown in Figure 4.3 is given in Figure 4.4. Here, we have to point out subtle differences regarding pixels resulting from experiment and simulation. In experimental images, pixel values are condensed information about the lipid mixture within the pixel area, because it was taken by a CCD camera collecting emitted photons from this area. In images of simulation, pixel values represent the lipid mixture at a certain point, e.g. we take the lower left corner of each pixel square. In addition to this, the computational data has to be interpolated to the discrete 8-bit set of grey values.

Using this discrete setting we apply a DFT to our image $\mathcal{P}$. To this end, we define a frequency grid spacing $\Delta\omega = 1/l$ and introduce a set of spatial frequencies

$$\begin{aligned} \Lambda_h := \{(\omega_{k_1}, \omega_{k_2}) \in \mathbb{R}^2 \,|\, \omega_{k_j} = k_j \Delta\omega,\ k_j \in \mathbb{Z}, \\ -\frac{n}{2} + 1 \leq k_j \leq \frac{n}{2},\ j = 1, 2\}. \end{aligned} \tag{4.7}$$

We use this set for the DFT and thus get the spatial frequency weights

$$q_{k_1 k_2} := \frac{l^2}{n^2} \sum_{l_1, l_2 = -n/2+1}^{n/2} p_{l_1 l_2} e^{-2\pi i \, (x_{l_1} \omega_{k_1} + x_{l_2} \omega_{k_2})}. \tag{4.8}$$

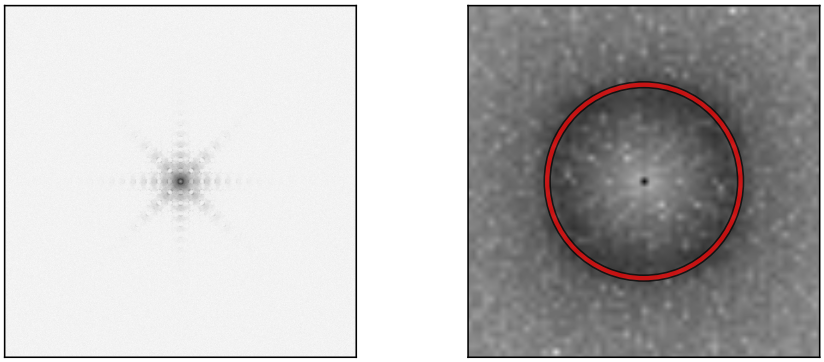

Figure 4.5: DFT of the image shown in Figure 4.3 (left) and enlarged center (right) with red marked frequencies related to the mean structure factor marked in Figure 4.6.

Consequently, we define the DFT of our image $\mathcal{P}$ as two dimensional set

$$\mathcal{Q} := (q_{k_1 k_2})_{k_1,k_2=-n/2+1}^{n/2}. \tag{4.9}$$

The DFT of our exemplary image shown in Figure 4.3 is given in Figure 4.5. According to our definition of the set of spatial frequencies Λ_h, the frequency weights related to lower frequencies are centered in $\mathcal{Q}$ now.

Let us now reveal the link between the Fourier transformed image $\mathcal{Q}$ and the structure sizes of the lipid domains in our original image $\mathcal{P}$. The frequencies belonging to a given frequency weight $q_{k_1 k_2}$ are interpreted as a combined vector of frequencies

$$\boldsymbol{\omega}_{k_1 k_2} := \begin{pmatrix} \omega_{k_1} \\ \omega_{k_2} \end{pmatrix}, \quad k_j \in \mathbb{Z},\ -\frac{n}{2}+1 \leq k_j \leq \frac{n}{2},\ j = 1,2. \tag{4.10}$$

We define spatial vectors of grid points in the same fashion

$$\boldsymbol{x}_{l_1 l_2} := \begin{pmatrix} x_{l_1} \\ x_{l_2} \end{pmatrix}, \quad l_j \in \mathbb{Z},\ -\frac{n}{2}+1 \leq k_j \leq \frac{n}{2},\ j = 1,2, \tag{4.11}$$

where we used bold notation for spatial coordinates. This allows us to rewrite our frequency weights $q_{k_1 k_2}$, $-n/2+1 \leq k_j \leq n/2$, $j = 1,2$, see (4.8), according to

$$q_{k_1 k_2} = \frac{l^2}{n^2} \sum_{l_1,l_2=-n/2+1}^{n/2} p_{l_1 l_2} e^{-2\pi i\, \boldsymbol{x}_{l_1 l_2} \cdot \boldsymbol{\omega}_{k_1 k_2}}. \tag{4.12}$$

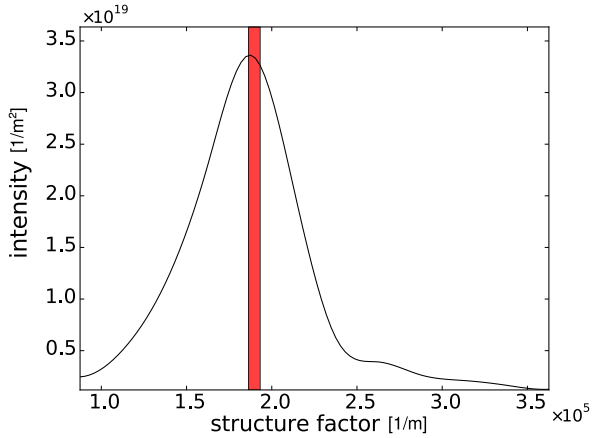

Figure 4.6: The power spectrum of the DFT image shown in Figure 4.5 with red marked condensed frequencies related to the mean structure factor.

Consequently, we interpret $q_{k_1k_2}$ as a measure for periodic patterns of wavelength $1/\|\boldsymbol{\omega}_{k_1k_2}\|_2$ in the direction of $\boldsymbol{\omega}_{k_1k_2}$. When we want to measure all periodicities of a certain wavelength in our original image $\mathcal{P}$, we have to define a reduced set of frequencies for our Fourier transformed image $\mathcal{Q}$ by

$$\lambda_h := \{\omega_k \in \mathbb{R} \mid \omega_k = k\Delta\omega,\ k \in \mathbb{Z},\ 0 \leq k \leq \frac{n}{2}\}. \tag{4.13}$$

Hence, we condense frequency weights of similar wavelength and thus define the structure factor s_k, $0 \leq k \leq n/2$, by

$$s_k := \sum_{\omega_k \leq \|\boldsymbol{\omega}_{k_1k_2}\| \leq \omega_{k+1}} q_{k_1k_2}, \quad k_j \in \mathbb{Z},\ -\frac{n}{2}+1 \leq k_j \leq \frac{n}{2},\ j = 1, 2. \tag{4.14}$$

Consequently, the structure factor measures periodic patterns of similar wavelength independent of its direction. The red marked frequency weights of our DFT in the right image of Figure 4.5 belong to the exemplary structure factor marked in Figure 4.6. The complete set of structure factors define the power spectrum $\mathcal{S}$ of our original image $\mathcal{P}$ by

$$\mathcal{S} := (s_k)_{k=0}^{n/2}. \tag{4.15}$$

The power spectrum of our exemplary image shown in Figure 4.3 is given in Figure 4.6.

The power spectrum reveals detailed information about structure sizes of images. However, it is impractical to evaluate series of images from experiment and simulation in such detail , see Figure 4.7. Instead, it is sufficient to know their dominant wavelengths, reflecting the dominant size of lipid

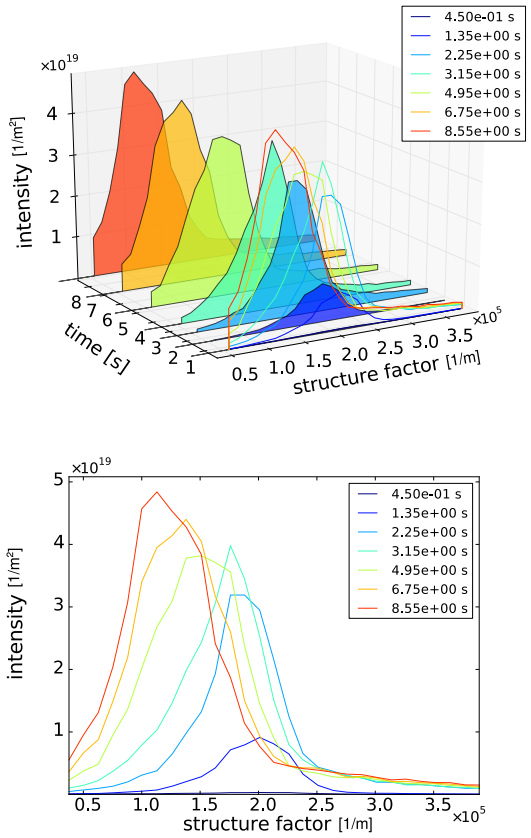

Figure 4.7: Series of power spectrums of an exemplary spinodal decomposition as 3D (top) and 2D plot (bottom) showing the characteristic evolution in time.

domains. Hence, we define the mean structure factor $\bar{s}$ by

$$\bar{s} := \sum_{s_k \in \mathcal{S}} (s_k q_k) / \sum_{s_k \in \mathcal{S}} s_k. \tag{4.16}$$

In practice, the mean structure factor is computed for a subset $\hat{\mathcal{S}}$ of $\mathcal{S}$. We address this issue in section 4.3. Now, the mean structure factor $\bar{s}$ and the structure size, respectively, the mean wavelength $1/\bar{s}$, represent the mean size of structures in our original image $\mathcal{P}$. The resulting mean wavelength $1/\bar{s}$ is demonstrated in our exemplary image shown in Figure 4.3. The resulting mean structure factor is marked in its power spectrum shown in Figure 4.6. Further, we marked the related DFT frequencies in Figure 4.5. All in all, we finally derived a measurement method for the domain sizes observed in experiments and simulations.

4.3 Application Issues

In the previous section 4.2, we proposed the structure factor as a measure for structure sizes of a given image. In this section, we further discuss the method in application and address non-obvious problems. We are especially interested in establishing whether this method allows comparison of different series of images and whether the mean structure size reflects the actual domain sizes.

We mentioned in the previous section that the Fourier transformation and its discrete counterpart reveal periodic structures. For this purpose we extend bounded finite domains by tiling in theory. But this procedure results in intrinsic problems at image boundaries. Unlike in simulation, where we can enforce periodicity by boundary conditions, this is not possible in our experiments. Here, we see jumps at the image border as shown in Figure 4.8. This results in very high frequency weights for frequencies connected to the image size, because the DFT tries to capture these jumps as shown in Figure 4.8. We solved this problem by using a method described by [Moi11] which smoothes image boundaries. This way we remove disturbing effects without changing the characteristic distribution of relevant frequency weights. The method works fine for nonperiodic data sets as shown in Figure 4.9.

Another influencing factor is the choice of the spatial frequencies Λ_h and its reduced set of frequencies λ_h. As described in the previous section we used a uniform grid of frequencies, more precisely $n \times n$ frequencies resulting in the frequency spacing $\Delta w = 1/l$, where n is the number of pixels in x- or y-direction and l the physical size of the image domain. Consequently, our spatial frequencies Λ_h are determined by the original image $\mathcal{P}$ and its physical length l. In order to get a sufficient number of frequencies or wavelengths of interest, we have to guarantee a minimum image resolution. If this is not achieved, it is impossible to reveal certain structure sizes and their change in time. Moreover, when we compare series of images produced in experiment and simulation, their resolution and physical length l should ideally match. This way we guarantee equal frequency weights and thus identically weighted information of structure sizes. This especially holds true when we use low numbers of frequencies. Nevertheless, the mean structure factor shows to be stable using different image resolutions using the same evaluated wavelengths, as shown in Figure 4.10.

At last, we address the mean structure factor $\bar{s}$ and the resulting mean wavelength $1/\bar{s}$. It was said to be a practicable measure, however, it differs from the actual mean domain size. This is a direct consequence of its definition (4.16). It averages over all frequencies and thus shifts $\bar{s}$ from its maximum, even or especially when we compute the mean structure factor for a subset $\hat{\mathcal{S}}$ of $\mathcal{S}$. This phenomenon is illustrated in Figure 4.11. However, we can still use the mean structure factor $1/\bar{s}$ as a measure for the quantitative development of the structure size in time as long as we evalu-

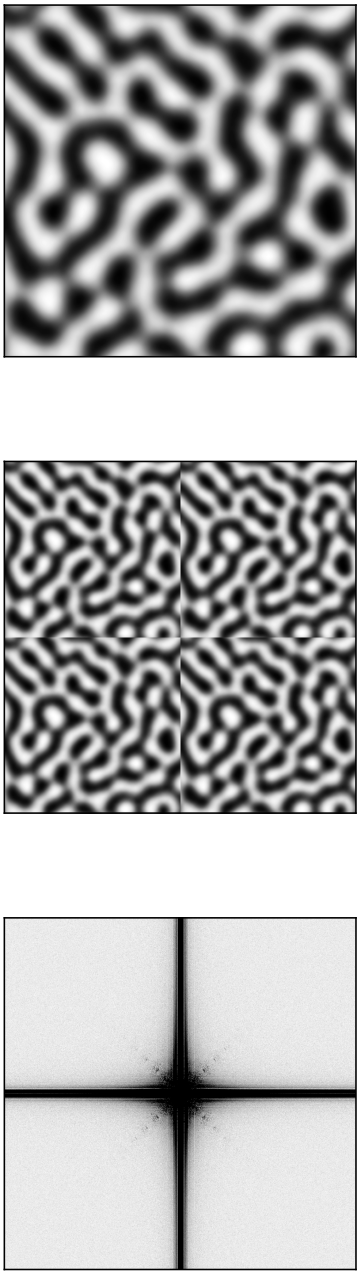

Figure 4.8: Exemplary image with nonperiodic boundaries (left), together with its tiling (middle) and DFT image (right).

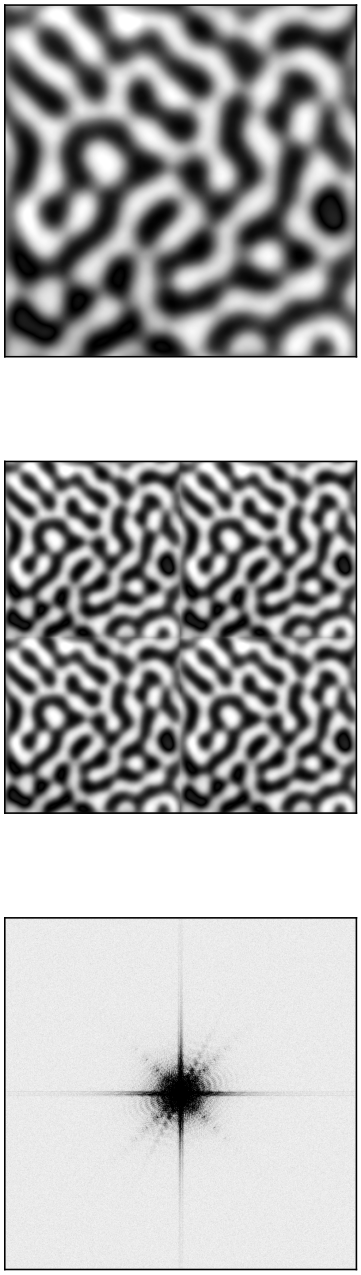

Figure 4.9: Exemplary image shown in Figure 4.8 with smoothed boundaries (left), together with its tiling (middle) and DFT image (right).

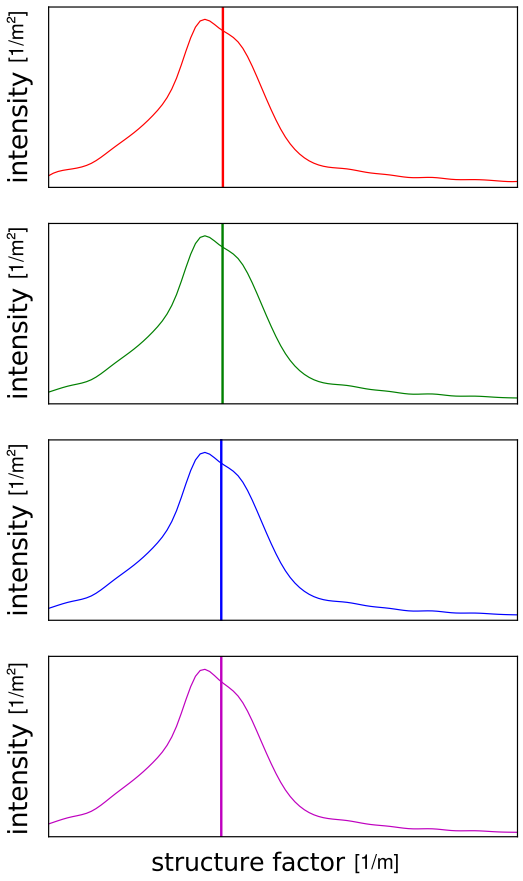

Figure 4.10: Power spectrum with mean structure factor — evaluated wavelengths $8.79 \cdot 10^{+4} - 3.77 \cdot 10^{+5}$ m — using the exemplary image shown in Figure 4.5 with following resolutions: 512x512 (red), 256x256 (green), 128x128 (blue), 64x64 (magenta). The virtually identical lines are plotted separately to allow a graphic representation.

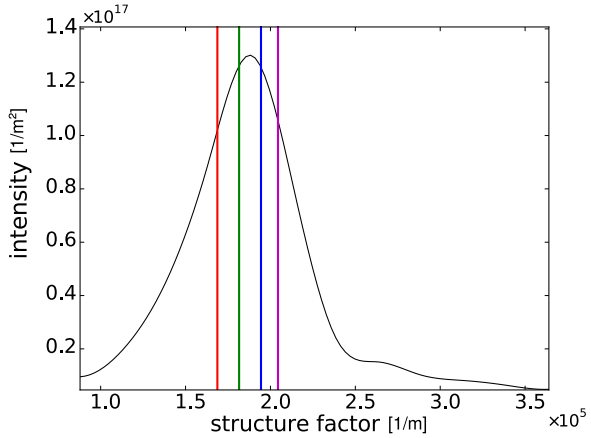

Figure 4.11: Power spectrum of the DFT image shown in Figure 4.5 with the mean structure factor for different sets of evaluated wavelengths: $8.8 \cdot 10^{+4} - 2.1 \cdot 10^{+5}$ m (red), $8.8 \cdot 10^{+4} - 2.8 \cdot 10^{+5}$ m (green), $8.8 \cdot 10^{+4} - 4.4 \cdot 10^{+5}$ m (blue), $8.8 \cdot 10^{+4} - 7.5 \cdot 10^{+5}$ m (magenta)

ate matching sets of wavelengths for the computation of the mean structure factor. Otherwise, we experience shifts of the the mean structure factor $1/\bar{s}$.

Despite the problems addressed, we found an efficient quantitative measurement method for domain sizes which allows us to evaluate and compare series of images from experiment or simulation.

Chapter 5

Simulation Results

In section 5.1, we simulate lipid decomposition using the C^0-IPDG approximation of the Cahn–Hilliard equation. Subsequently, we study the sensitivity of the Cahn–Hilliard equation to its parameters in section 5.2. In section 5.3, we compare series of images taken in simulation and experiment using a physical set of parameters. Most of the results have been published in [BFL$^+$13].

5.1 Implementation Issues

We implemented the afore-mentioned C^0-IPDG finite element method for the Cahn–Hilliard equation with constant mobility using the programming language *Python* [vRdB91] and different libraries, particularly the mathematical libraries *NumPy* and *SciPy* [Oli07], the finite element library *FEniCS* [LMWea12], the *Python Imaging Library* (PIL), and the plotting library *matplotlib* [Hun07].

We discretized our computational domain $\Omega := (-l/2, +l/2)^2$, with domain length l, by a uniform spatial discretization. This is based upon a uniform grid with square cells of side length h. These cells are further split into triangles. We used crossed cells, i.e. a cell is split into four triangles induced by its diagonals, in order to avoid artificial effects of broken symmetry as shown in Figure 5.1. We further used standard Lagrange elements with polynomial degree $p = 2$ and the backward Euler scheme in time with constant time step size τ. The resulting nonlinear equation was solved by a Newton method described in section 3.3.

For numerical reasons we used a dimensionless form of the Cahn–Hilliard equation (2.15). This has shown to be sufficiently stable for the set of physical parameters chosen in section 5.2 and section 5.3. Given a physical length L we introduce dimensionless spatial coordinates $\hat{x} = x/L$ where x denotes the original spatial coordinates. Thus we get the dimensionless operator $\hat{\nabla} = L\nabla$ and the dimensionless Cahn–Hilliard equation is then

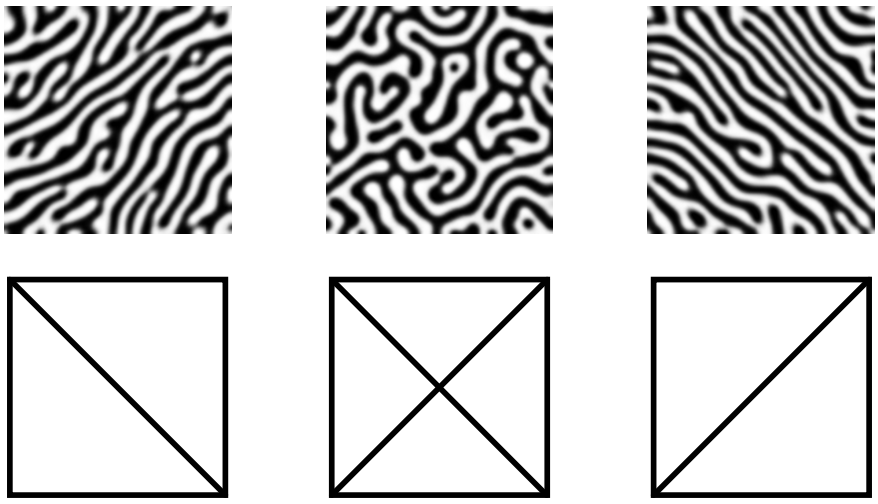

Figure 5.1: Spinodal decomposition (top) using identical initial conditions but different FEniCS's grid structure options of square cells (bottom): *left* (left), *crossed* (middle) and *right* (right).

given by

$$\frac{\partial c}{\partial t} = \hat{\nabla} \cdot \frac{M_D}{L^2} \hat{\nabla} \left(f'(c) - \frac{\epsilon^2}{L^2} \hat{\Delta} c \right). \tag{5.1}$$

We further use the notation from section 3.3 and omit the hats assuming non-dimensional operators. Using the backward Euler scheme in time, the resulting C^0-IPDG formulation of the dimensionless Cahn–Hilliard equation (5.1) is to find a solution $c_h^{n_\tau+1} \in W_h$ for a given concentration $c_h^{n_\tau} \in W_h$ such that for any $w_h \in W_h$ there holds

$$\begin{aligned} &-\Big(\sum_{T\in\mathcal{T}_h} (w_h, c_h^{n_\tau+1})_{0,T} - \sum_{T\in\mathcal{T}_h} (w_h, c_h^{n_\tau})_{0,T} \Big) \\ &= \hat{\tau} \sum_{T\in\mathcal{T}_h} (\nabla w_h, \nabla f'(c_h^{n_\tau+1}))_{0,T} + \hat{\epsilon}^2 \Big(\sum_{T\in\mathcal{T}_h} (D^2 w_h, D^2 c_h^{n_\tau+1})_{0,T} \\ &+ \sum_{E\in\mathcal{E}_h^{\bar{\Omega}}} (\llbracket \frac{\partial w_h}{\partial \boldsymbol{n}} \rrbracket, \{\!\{ \frac{\partial^2 c_h^{n_\tau+1}}{\partial \boldsymbol{n}^2} \}\!\})_{0,E} + \sum_{E\in\mathcal{E}_h^{\bar{\Omega}}} (\{\!\{ \frac{\partial^2 w_h}{\partial \boldsymbol{n}^2} \}\!\}, \llbracket \frac{\partial c_h^{n_\tau+1}}{\partial \boldsymbol{n}} \rrbracket)_{0,E} \\ &+ \alpha \sum_{E\in\mathcal{E}_h^{\bar{\Omega}}} h_E^{-1} (\llbracket \frac{\partial w_h}{\partial \boldsymbol{n}} \rrbracket, \llbracket \frac{\partial c_h^{n_\tau+1}}{\partial \boldsymbol{n}} \rrbracket)_{0,E} \Big), \end{aligned} \tag{5.2}$$

with the dimensionless time step size $\hat{\tau} = \tau M_D / L^2$ and the dimensionless line tension related parameter $\hat{\epsilon}^2 = \tau \epsilon^2 / L^2$. Numerical constants and parameters used for simulations are given in Table 5.1.

Name	Symbol	Unit	Value
Length Scaling	L	m	$1.0 \cdot 10^{-4}$
Length	l	m	$8.0 \cdot 10^{-5}$
Grid Size	h	m	$1.2 \cdot 10^{-6}$
Time Step Size	τ	s	$5.0 \cdot 10^{-2}$
Penalty Parameter	α		$1.2 \cdot 10^{+1}$

Table 5.1: Constants and parameters for Cahn–Hilliard simulations.

We implemented the described dimensionless C^0-IPDG method for the dimensionless Cahn–Hilliard equation (5.2) for the afore-mentioned domain using periodic boundary conditions. This differs from our setting described in section 2.2 and makes considerations concerning boundary conditions obsolete. The choice of flat domains with periodic boundary conditions is motivated by experimental data where only parts of the vesicle surface are observed and evaluated. Thus we can neglect the vesicles curvature described in section 1.2, because the evaluated domain is small compared to the total vesicle surface. Furthermore, experiments suggest homogeneous phase separation on the entire membrane. Thus we can expect information passing the boundary at one side of the domain to be replaced by corresponding information on the opposite boundary. In this case, information means lipid mixture in equal state of decomposition as described in section 1.2. Hence, the choice of periodic boundary conditions is justified. The condition is implemented by identifying the degrees of freedom lying on opposite sides of the boundary in x- and y-direction.

5.2 Parameter Study

Using the previously described dimensionless Cahn–Hilliard equation (5.2), we perform simulations of phase separation in order to pursue studies related to the relevant parameters of the model. When we assume constant mobility $M_D = D$, the Cahn–Hilliard equation reads

$$\frac{\partial c}{\partial t} = \nabla \cdot M_D \nabla (f'(c) - \epsilon^2 \Delta c). \tag{5.3}$$

Consequently, it depends on the diffusion rate D, the free energy parameter φ scaling the double well potential, and the line tension related parameter ϵ^2. Further details about these parameters are given in section 2.1. In short, the free energy is the dominant part of the Cahn–Hilliard equation at the beginning of the decomposition whereas line tension is dominant at the end. So far we have not discussed the influence of the diffusion rate. We can expect that higher values accelerate the phase separation in time. For a detailed quantitative analysis, we present a parameter study that

we published in [BFL$^+$13]. This study shows the sensitivity of the Cahn–Hilliard equation (5.3) with respect to its parameters. Thereby we used a set of physically reasonable parameters.

As reference system we take the following set of parameters for lipid membranes:

$$D = 1.0 \ \frac{\mu \mathrm{m}^2}{\mathrm{s}}, \quad \varphi = 4.0 \ \frac{\mathrm{J}}{\mathrm{m}^2}, \quad \epsilon^2 = 1.0 \cdot 10^{-12} \ \mathrm{J}. \tag{5.4}$$

In all simulations we start at homogeneous lipid mixtures and vary our parameters separately by an appropriate value. Then the series of images is evaluated using the structure factor method presented in section 4.2. The resulting mean structure sizes are given in Figure 5.2. As already suggested, the diffusion parameter D scales the resulting curves in time. The higher the diffusion, the faster the decomposition takes place. Other characteristics are unaffected, especially the resulting mean structure size after separation. This property is changed by the line tension related parameter ϵ^2. Here, higher values results in larger domains. A view on the total free energy explains this behavior, because larger domains form out less boundaries compared to its lipid phase volume. This parameter also influences the onset of phase decomposition in time. The lower ϵ^2, the sooner the phase separation begins. An equivalent effect is achieved by changing the free energy parameter φ. Here, higher values of φ shift phase separation into an earlier point in time. This is in accordance with our argumentation in section 2.1. The parameter determines the inner height of the double well potential and thus makes homogeneous mixtures even more unattractive when it is augmented. Consequently, the system decomposes earlier for higher values of φ in order to reduce its total free energy sooner.

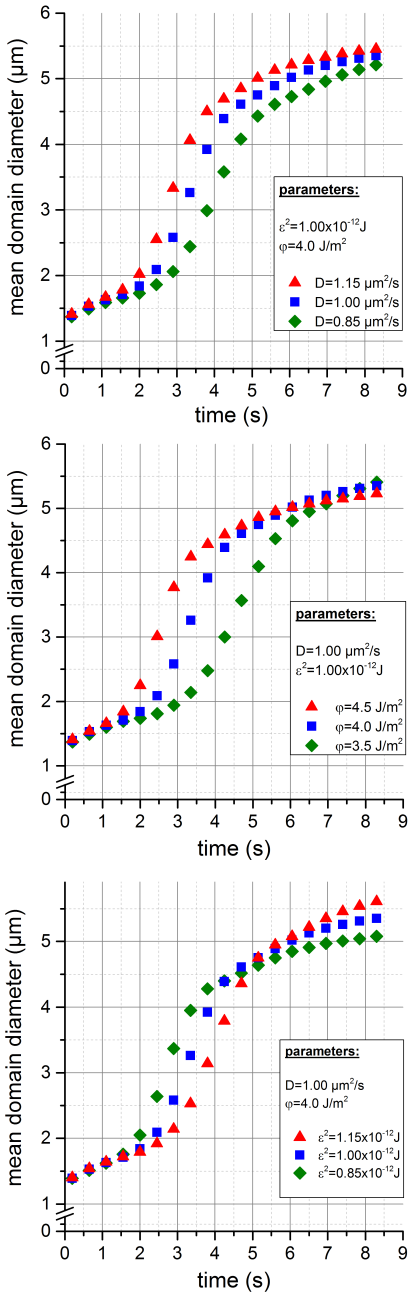

Figure 5.2: Parameter study of the Cahn–Hilliard equation. The blue graph shows the reference case with unchanged parameters. [BFL+13]

5.3 Comparison to Experiments

We validate our model by experimental data of phase separation in GUVs, as presented in [BFL$^+$13]. The vesicles consist of DOPC:DPPC:DPPG in a mixture of 5:4:1 enriched with cholesterol. Here, charged DPPG lipids are used for electroformation of GUVs as described in [ASM$^+$92] and not relevant in this experimental setting as previously explained in section 1.2. The resulting vesicles show diameters of up to 200μm. For details concerning lipids, fluorescent markers and fabrication we refer to [BFL$^+$13].

After assembly the GUVs are supercooled and show stable homogeneous mixtures. Then phase separation is induced by light. Using a microscope lamp, the cooled GUVs are re-heated to temperatures at a certain level which allows phase separation but still are below the critical temperatures of separation. A series of images of a typical experiment is given in Figure 5.3. We observe three different stages of phase separation that can be compared to other experiments of phase separation in GUVs. The top image shows blurred phases at the beginning of the decomposition. The next stage shown in the middle reveals first interconnected domains. At the bottom image, we see the final stage during which domains further form into sharply bounded separated phases of circular shape. Here, the domain growth is driven by coalescence and fused domains further relax to circular shape. The series of images from this experiment is evaluated for their mean structure sizes using the structure factor method explained in section 4.2. The resulting curve is shown in Figure 5.4. Parts of the curve belonging to the afore-mentioned three qualitatively different stages are separately marked by straight lines. Their gradient corresponds to the average slope of the curve.

We performed numerical simulations to match characteristic properties of the experiment, for example the mean structure sizes over time with special respect to the last stage. For that purpose we used our previously chosen reference set of parameters for the Cahn–Hilliard equation (5.3):

$$D = 1.0 \ \frac{\mu\mathrm{m}^2}{\mathrm{s}}, \quad \varphi = 4.0 \ \frac{\mathrm{J}}{\mathrm{m}^2}, \quad \epsilon^2 = 1.0 \cdot 10^{-12} \ \mathrm{J}. \tag{5.5}$$

This reference set from our parameter study in section 5.2 fulfills our afore-mentioned requirements and the simulation shows good agreement to the experiment in quality and quantity. The diffusion rate D is at the lower limit suggested for lipid bilayers. Here, diffusion rates of $1-20 \ \mu\mathrm{m}^2/\mathrm{s}$ are proposed in [KS06]. This guess is supported by multiple measurements with different techniques for comparable systems [DBV$^+$01, FOL04, OWL05, KSB$^+$03, KS06]. However, not all parameters can be physically motivated. Regarding our choice of the additional parameters φ and ϵ^2, we are free to some extent. For instance, ϵ^2 is connected to the line tension only in a variational sense as mentioned in section 2.1.

Let us now compare simulation and experiment in detail. Again we

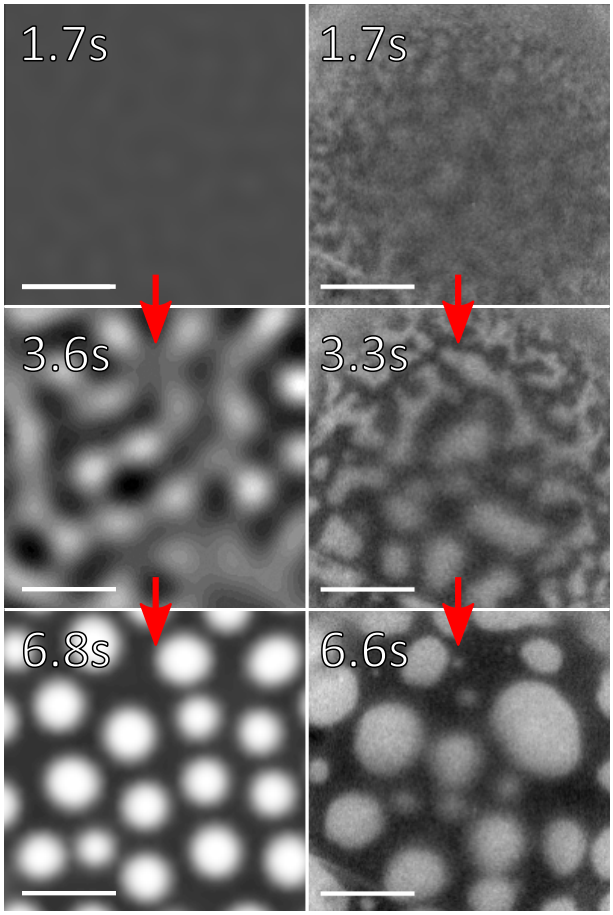

Figure 5.3: Evolution in time of phase separation in simulation (left) and experiment (right). The bar represents 10 μm. [BFL$^+$13]

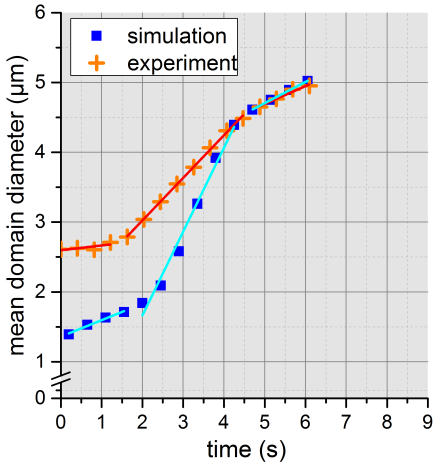

Figure 5.4: Comparison of mean domain size over time in experiment and simulation according to [BFL+13].

divide the evolution of the mean structure sizes in simulation into three different stages marked by straight lines with averaged slopes as we did for the experimental curve shown in Figure 5.4.

At the initial stage, both the simulation ($0.0 - 2.0$ s) and the experiment ($0.0 - 1.5$ s) start from a rather homogeneous concentration and qualitatively show the same decomposition in the top images of Figure 5.3. However, their measured absolute mean structure sizes differ. The size in the simulation is higher than it is in the actual experiment. Furthermore, the slope obtained by simulation (0.24 μm/s) is steeper than the one obtained by experiment (0.06 μm/s). The cause for this offset may be due to imperfect initial mixture of phases at the beginning of the experiment. Such perturbations of regular comparable big size structures shift the mean structure size to higher values. More physical arguments including technical details are given in [BFL+13]. As described by our parameter study in section 5.2, simulations show no parameters that influence the initial mean domain size. Fortunately the offset vanishes in time and thus supports our argumentation.

The second stage of the experiment ($1.5 - 4.5$ s) and the simulation ($2.0 - 4.0$ s) is characterized by an accelerated growth of the mean structure sizes shown in Figure 5.3. The slope obtained in the simulation is 1.2 μm/s and 0.6 μm/s in the experiments. When we compare the images in the middle of Figure 5.3, we observe qualitatively similar patterns of coalescence. While this form of growth is dominant in the experiment, it does not show in the simulation at this stage. Here, further decomposition takes place at the same time.

During the last stage starting at 4.5 s in the simulation and the experiment we see identical mean structure sizes and slopes (0.2 μm/s). Now,

domain growth decelerates and lipid domains form circular shapes. This is shown in the lower images of Figure 5.3. Coalescence is the dominant factor of growth in both the experiment and the simulation. However, this is less likely with incresing time, because the distance between the domains grows.

We made out three different stages in the experiment and the simulation. At all stages, we see good agreement of their characteristics supported by a qualitative discussion of the images and a quantitative evaluation of the mean structure sizes. Consequently, the Cahn–Hilliard equation has shown to be an appropriate model for phase separation in lipid membranes reflecting physical properties.

Chapter 6

Conclusion and Outlook

In the first part of this thesis, we introduced an adaptive C^0-IPDG method for the biharmonic problem based on a residual-type a-posteriori error estimator. Furthermore, we presented a contraction property in form of a weighted sum of the C^0-IPDG energy norm of the global discretization error and the estimator for any polynomial order.

In addition to this we implemented a C^0-IPDG method for the Cahn–Hilliard equation and introduced the structure factor method as a measure of structure sizes. This method has shown to be a competitive method for model validation and enables us to analyze numerous series of images. We further discussed the sensitivity of the Cahn–Hilliard equation to its intrinsic parameters. Consequently, we simulated phase separation in GUV and our results show good agreement to experiments in qualitative, i.e. phenomenological, and quantitative manner. These results were achieved either by directly comparing images or analyzing their structure factor. Overall, we proved the Cahn–Hilliard equation to be an appropriate model for lipid systems and derived a numerically efficient way to simulate and evaluate phase separation in vesicles using the C^0-IPDG formulation of the Cahn–Hilliard equation and the structure factor method. Nevertheless, we address fields of possible future research in the following sections.

6.1 Mechanical Forces

Langmuir–Blodgett troughs induce phase separation in lipid monolayers by means of the pressure. A schematic description of this setting is given in Figure 6.1. Phase separation induced by compression on a Langmuir–Blodgett trough differs from the phase separation in vesicles described in section 1.2. An exemplary series of images is given in Figure 6.2. This problem goes beyond the scope of this thesis. However, it is the main topic of the second funding period of the priority program 1506. Therefore, the model presented in section 2.1 has to be extended such that mechanical forces can

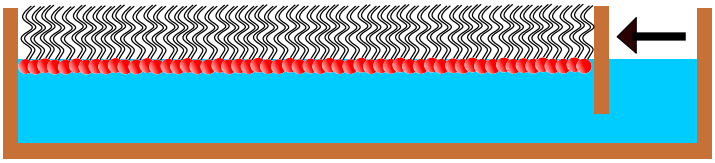

Figure 6.1: Schematic illustration of a Langmuir–Blodgett trough with a lipid monolayer. In typical experiments the thickness of the lipid monolayer is about 5 nm, whereas the height of the water volume is about 1 mm.

be taken into account. Mechanical stress influences the surface tension of the membrane over time. This is caused by the compression rate of the trough barrier acting on the membrane. Hence, viscoelasticity has to be incorporated. The resulting equations feature an additional strain energy function. When Maxwell viscoelasticity is assumed, as proposed in our renewal proposal for the SPP 1506, a strain energy density function $W(c, \boldsymbol{\varepsilon}(\boldsymbol{u}))$ consisting of elastic and viscous parts has to be used, depending on the local phase concentration c and the linearized strain tensor $\boldsymbol{\varepsilon}$. The tensor itself depends on the mechanical displacement $\boldsymbol{u}$ of the membrane. Assuming quasistatic elasticity when the mechanical effects influence lipid phases immediately, i.e. when we observe spontaneous relaxation with respect to the diffusion rate, the following parabolic–elliptic system of equations has to be solved:

$$\frac{\partial c}{\partial t} + \nabla \cdot M(c) \nabla \Big(\frac{\epsilon^2}{2} \Delta c - \mu(c) - \nabla \cdot W_c(c, \boldsymbol{\varepsilon}(\boldsymbol{u})) \Big) = 0, \tag{6.1}$$

$$\nabla \cdot W_{\boldsymbol{\varepsilon}}(c, \boldsymbol{\varepsilon}(\boldsymbol{u})) = \mathbf{0}. \tag{6.2}$$

Here W_c and $W_{\boldsymbol{\varepsilon}}$ denote the derivatives of $W(c, \boldsymbol{\varepsilon}(\boldsymbol{u}))$ with respect to c and $\boldsymbol{\varepsilon}$, respectively. Cahn–Hilliard equations incorporating elasticity are discussed in [Gar03, Gar05, GW05, LLJ98, Mir00], whereas viscoelastic contributions are presented in [PZ08a]. In contrast, nonstationary elasticity has to be assumed when relaxation occurs on diffusion time scales which leads to the parabolic–hyperbolic system of equations

$$\frac{\partial c}{\partial t} + \nabla \cdot M(c) \nabla \Big(\frac{\epsilon^2}{2} \Delta c - \mu(c) - W_c(c, \boldsymbol{\varepsilon}(\boldsymbol{u})) \Big) = 0, \tag{6.3}$$

$$\frac{\partial^2 \boldsymbol{u}}{\partial t^2} - \nabla \cdot W_{\boldsymbol{\varepsilon}}(c, \boldsymbol{\varepsilon}(\boldsymbol{u})) = \boldsymbol{f}, \tag{6.4}$$

where $\boldsymbol{f}$ denotes an external force density. Such systems are of Cahn–Hilliard–Gurtin type [BP05, Mir01, PZ08b].

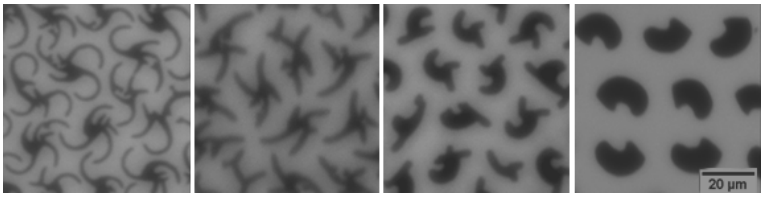

Figure 6.2: Temporal relaxation of lipids domains in a lipid monolayer on a Langmuir-Blodgett trough provided by T. Franke.

6.2 Fluidics and Electric Charges

Experiments investigating droplet coalescence of lipid domains suggest fluidic properties of lipid membranes [KG07, MRMDN01, ALG$^+$05]. In addition, the existence of concentration driven velocity fields is proposed in [Lei08]. Once more, the presented model has to be modified in order to incorporate such velocity fields to the phase field model presented in section 2.1. A Cahn–Hilliard equation combined with fluid dynamics was first described in [HH77]. The Cahn–Hilliard equation consequently has to be extended by an advection term $\boldsymbol{v} \cdot \nabla c$. Therefore, mass transfer or transfer of concentration is included which is driven by a velocity field v. The velocity field is described by a Navier–Stokes equation. An additional force term $\mu(c)\nabla c$ arising from the concentration and the chemical potential is added to the right-hand side of the fluidic equation and the resulting Cahn–Hilliard–Navier-Stokes system is given by

$$\frac{\partial \boldsymbol{v}}{\partial t} - \nabla \cdot (\nu(c) T(\boldsymbol{v})) + \nabla p = \mu(c) \nabla c, \tag{6.5}$$

$$\nabla \cdot \boldsymbol{v} = 0, \tag{6.6}$$

$$\frac{\partial c}{\partial t} + \boldsymbol{v} \cdot \nabla c - \nabla \cdot M(c) \nabla \mu(c) = 0, \tag{6.7}$$

where $T(\boldsymbol{v})$ denotes the velocity strain tensor and $\nu(c)$ the viscosity with respect to the phase concentration. Promising numerical investigations of this system were performed within a master thesis [Rei13] co-supervised by the author.

So far, the influence of charged lipids, e.g. DPPG, has been neglected. This holds true up to certain concentrations, for example, charged lipids used for GUV production as described in section 5.3. Higher rates of charged lipids induce electric forces and thus further phenomena. From a theoretical point of view, hexagonal alignment of lipid structures has been predicted, forced by an elastic coupling to the membrane [KSA06]. This has been verified in experiments [BHW03a, RKG05]. However, [Lei08] suggests hexagonal alignments of lipid domains to be of pure electrostatic origin in systems with electric charged lipids. Validation by simulations using an appropriate model could support this experimental finding. Therefore, electrostatic

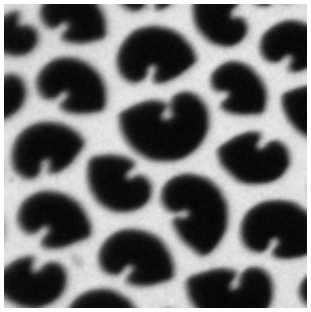

Figure 6.3: Experimental images showing chiral lipid domains forming kidney like shapes provided by S. Burger.

forces have to be coupled to the previously presented Cahn–Hilliard–Stokes system (6.5) – (6.7). Following [EFG+07, FGJ11, CFGK12], forces of electrostatic nature are added as additional term $\rho(c)\nabla V$ to the right-hand side of the Stokes equation (6.5). Here, V denotes the electric potential which is computed by the Poisson equation

$$-\epsilon_d \Delta V = \rho(c), \tag{6.8}$$

where ϵ_d denotes the dielectric constant and $\rho(c)$ the charge density. In doing so, the charges are fixed to the lipids. The concentration is then directly related to the charge density ρ. Finally, the coupled system is given by

$$\frac{\partial \boldsymbol{v}}{\partial t} - \nabla \cdot (\nu(c) T(\boldsymbol{v})) + \nabla p = \mu(c)\nabla c - \rho(c)\nabla(V), \tag{6.9}$$

$$\nabla \cdot \boldsymbol{v} = 0, \tag{6.10}$$

$$\frac{\partial c}{\partial t} + \boldsymbol{v} \cdot \nabla c - \nabla \cdot M(c)\nabla\mu(c) = 0, \tag{6.11}$$

$$-\nabla \cdot (\epsilon_d \nabla V) = \rho(c), \tag{6.12}$$

where $T(v)$ denotes the velocity strain tensor, $M(c)$ denotes the mobility and $\nu(c)$ the viscosity depending on the concentration. Numerical studies performed by [Rei13] so far have not shown the mentioned hexagonal alignment. But the results give first evidence for even more complex lipid domains. Electrostatic forces have already been discussed as the origin of complex lipid structures [KL96, KL00]. The understanding of the electrostatic influences would give new insights, for example, on the formation of chiral lipid domains as shown in [MW84, WM85] and Figure 6.3. Such formations motivate the following second part of this thesis.

Part II

Enantiomer Separation

Chapter 7

Introduction

The second part of this thesis investigates separation of chiral objects (enantiomers) by *surface acoustic wave* (SAW) generated fluid vorticity patterns. The problem can be formulated as a fluid–structure interaction problem for which we use the *fictitious domain Lagrange multiplier* (FDLM) method. In section 7.1 we expose our field of research, and motivate it by examples of application. In section 7.2 we present the experimental setup for which the possibility of enantiomer separation shall be discussed. In section 7.3 we finally give the outline of this second part.

7.1 Separation of Chiral Objects

According to the Oxford Dictionary a *chiral* object is *asymmetric in such a way that the structure and its mirror image are not superimposable*. In a mathematical sense a chiral object cannot be *mapped to its mirror image by rotations and translations*. The word *chiral* is derived from Greek and means *hand*. The left and right human hand are indeed chiral objects and thus define left- and right-handedness as shown in Figure 7.1. We use these simplified terms and avoid other technical naming conventions. This is sufficient for our purpose. Nevertheless we introduce *enantiomers*, another word derived from Greek which denotes *objects of opposite form*. Our left and right hand, for instance, are chiral objects of opposite form and therefore enantiomers. A compound consisting of one sort of enantiomers, i.e. objects of the same chirality, is said to be enantiopure or unichiral; other compounds are called racemic.

Looking beyond the scope of human hands, enantiomers on even smaller scales exist in nature. Louis Pasteur first demonstrated the existence of chiral molecules in 1848. Later Joseph Le Bel and Jacobus Van't Hoff achieved major advances in stereochemistry published in 1874. The period that followed this discovery vividly influenced physics and inspired, among other things, the concept of parity.

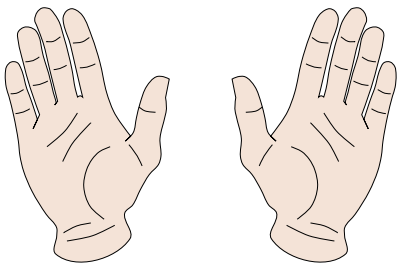

Figure 7.1: Human hands illustrating chirality.

In order to investigate the significance of enantiomers in applications we repeat our argumentation in [BFH+15] and look at molecular scales. Here enantiomers or chiral molecules show different physical, chemical and biological properties, depending on their handedness. Enantiomers show the same chemical makeup, i.e. the molecules consist of identical chemicals, but show different shapes. Often this difference is crucial to the molecule properties, e.g. in being a substance tasty or disgusting, medicative or toxic. Realizing that chemical fabrication often results in racemic compounds, it is clear that enantiomer separation is a decisive technique for agrochemical, electronical, pharmaceutical, food, flavor, and fragrance industries [Bes03, CSCe93, CSCe98, FLe06, KMe98]. So far, enantiomer separation is performed using gas or high pressure liquid chromatography [BBe06, Wel09], capillary electrophoresis [Scr08], and nuclear magnetic resonance [Wen07]. These techniques are slow, cost-intensive or both.

The afore-mentioned drawbacks of existing techniques suggest the development of new ones. A new technology is based on SAW generated vorticity patterns. Enantiomers get separated on the surface of a fluid using counter-rotating vortices. The resulting method is expected to be fast and cost-effective. From a theoretical point of view it has already been shown that enantiomers exhibit different propagation properties in microflows due to their chirality [KSTH06, BBe06, Li06, RFPS09]. In addition to this, preliminary experiments performed by [Kon08] showed left- and right-handed L-shaped objects to be attracted by vortices rotating clockwise and counterclockwise, respectively.

7.2 Experimental Setup

In what follows we give a brief description of the major components of the experimental setup adapted to our purposes; for a comprehensive version including technical details of the setup and the particle fabrication we refer to [Bur13]. Further details about the relevant processes are provided in later

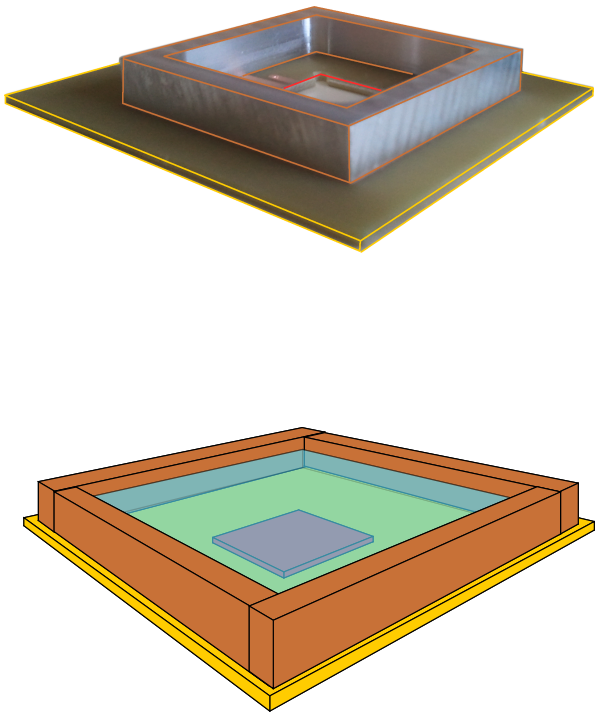

Figure 7.2: Side-view of the experimental setting (top), together with its illustration (bottom). The setup is mounted on a circuit board (yellow) consisting of the fluid container (brown), the water bulk (blue) and the IDT with substrate layer (red) in the middle on the bottom of the water bulk.

chapters.

The experimental setup is mounted on a circuit board illustrated in Figure 7.2. Its core consists of an *interdigital transducer* (IDT) which is placed on top of a substrate layer. This setup is placed in the bottom middle of a fluid container filled with water.

When we apply a radio frequency signal to the IDT, the electronic signal is converted into acoustic waves, exploiting the piezoelectric effect of the underlying substrate layer. These *surface acoustic waves* (SAWs) spread out in a certain direction on the substrate layer. The energy of the waves couples into the fluid and causes pressure waves on a time scale of nanoseconds ($\sim 10^{-9}$ s). These pressure waves induce fluid streaming which generates a stationary flow field within milliseconds ($\sim 10^{-3}$ s). The multiscale process in time leads to pairwise counter-rotating vortices on top of the water surface as shown in Figure 7.3.

Geometric objects like circles, squares, and L-shaped enantiomers are placed on top of the water surface into the SAW generated vorticity pattern

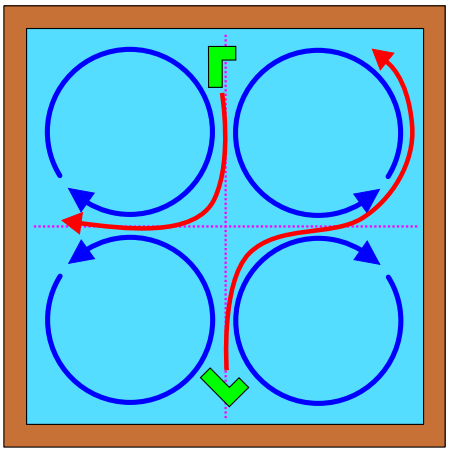

Figure 7.3: SAW induced vorticity pattern (top view) with propagating L-shaped enantiomers.

as shown in Figure 7.3. The thin particles float on top of the water surface undergoing translation and rotation. Their depth of penetration of the water bulk is negligible compared to their size. Both properties are guaranteed by a hydrophobic coating. After placement, the particles mainly follow the streamlines of the vorticity pattern which is related to the flow field on top of the fluid volume. In experiment the particles show characteristic properties of propagation related to their shape which can be recorded.

7.3 Resulting Problems and Outline

In the beginning we mentioned the fluid–structure interaction problem to be solved by a FDLM method. However the computation of the previously described fluid-structure interaction problem in total would exceed the numerical resources available, in particular the update of the fluid volume. Consequently we reduce the numerical complexity by decoupling the computation of the SAW generated vorticity pattern on top of the water bulk from the fluid–structure interaction problem.

In chapter 8 the SAW actuated fluid flow inside the fluid volume is modeled by the compressible Navier–Stokes equations. We further exploit the multiscale nature of the problem in time and apply a homogenization approach which was originally developed by [Bra96]. Thereby we separate the propagation of the pressure waves into the fluid which takes place on time scales of nanoseconds, and the fluid streaming occurring on time scales of milliseconds. The simulation results using this method correspond well with experimental data, as shown in [GHK$^+$07, Kös07]. However, the simulations conducted so far were either on 2D domains or 3D domains of low spatial

resolution. In contrast to this we perform 3D computations which allows us to simulate a reduced setup and compare the results with experimental data. Thus we gain information of the internal flow field of the setup which has not yet been measured in experiments.

In chapter 9 we present a FDLM method for particles in fluid flows. The method was proposed in [GPH$^+$01] and has been successfully applied to problems of sedimentation [PJG05] and rheology of red blood cells in microvessels [WPXG09]. The fact that the particles float on top of the water volume with minimal depth of penetration allows us to model the fluid–structure interaction problem as a single 2D problem. Thereby the fluid flow in the top layer of the water volume is now taken as a stationary velocity field of the resulting domain. Here, we use the fluid vorticity pattern suggested by [KSTH06] for which enantiomer separation was predicted at least from a theoretical point of view. We make out differences of the vorticity patterns and compare again simulation results to experimental data and show specific cases of enantiomer separation.

In chapter 10 we draw a final conclusion for this second part and show possibilities for future research.

Chapter 8

Surface Acoustic Waves

We give a short introduction to *surface acoustic wave* (SAW) driven microfluidics in section 8.1. Further, we present a model for this problem in section 8.2 and its implementation in section 8.3 following [Kös06, GHK+07]. Using this implementation we perform reduced numerical simulations for experimental settings in section 8.4. This way we investigate the SAW induced flow field and compare the computed vorticity pattern to experimental data.

8.1 Surface Acoustic Wave driven Microfluidics

In this section, we describe the basic physical background of surface acoustic wave driven microfluidics. Further detailed physical insights have been provided by T. Frommelt [Fro07] and S. Burger [Bur13], collaboration partners related to *surface acoustic waves* (SAWs) experiments conducted at the Chair of *Experimental Physics I* at the University of Augsburg. The specific experimental setting is described in detail in [Bur13].

SAWs were first predicted by Lord Rayleigh in 1885 [Ray85]. Using a model incorporating longitudinal and shear waves, he was able to explain the propagation of earthquakes. Mechanical waves travel along the surface of a solid material and decrease exponentially in amplitude. These waves are now called Rayleigh waves. Another ingredient was the discovery of piezoelectricity by the brothers Pierre and Paul-Jacques Curie in 1880. They described the mechanical deformation of materials like quartz crystals using electromagnetic fields. The first device producing surface acoustic waves was invented by White and Voltmer in 1965 [WV65]. Since then such electronic devices show a wide spectrum of applications, for example as actuators in common rail diesel engines.

A core component of such devices is the *interdigital transducer* (IDT) consisting of a series of interleaved electrodes placed on a substrate layer as shown in Figure 8.1. The electrodes are coated by conducting metals and the substrate layer is made from piezoelectric materials like quartz, lithium

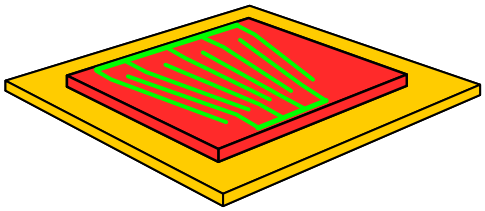

Figure 8.1: Illustration of a tapered IDT on a substrate layer.

niobate, or zinc oxide. The width of the electrodes determines the optimal radio frequency signal at which maximal conversion of an electrical to a mechanical signal is guaranteed. The optimal frequency is then called the center or synchronous frequency of the device. Typical frequencies range from 10^6 Hz to 10^9 Hz, i.e. from MHz to GHz. The substrate layer in the relevant experimental setting consists of lithium niobate and the IDT performs at frequencies about $1.0 \cdot 10^8$ Hz . The resulting electromagnetic field of the electrodes couples into the substrate layer and induces a mechanical displacement. The displacement propagates like sinusoidal waves of a given amplitude, wavelength and decay as described by [GHK$^+$07]. The mechanical displacement is about 1 nm, i.e. 10 Å. The waves propagate in the lithium niobate substrate layer with signal sound speed about $c_s = 3.9 \cdot 10^3$ m/s (we use temperature dependent material constants at 25 °C in this part). Consequently, the resulting wavelength λ is given by $\lambda = c_s/f \approx 3.9 \cdot 10^{-5}$ m. The displacement is therefore small compared to wavelength and we can neglect the displacement in our model.

The spatial propagation of the surface acoustic waves in the substrate layer is determined by the geometry of the interleaved electrodes of the IDT and its position on the substrate layer. A schematic illustration of the propagated waves in our setting is shown in Figure 8.2. Here, a tapered IDT on a 128° rot Y-Cut substrate layer is used and the waves propagate in X direction of the crystal, see [Fro07]. Resonance effects inside the tapered IDT determine the waves to admit a constant width about $\lambda/2$, i.e. ≈ 15 μm. After emission, the waves decay exponentially. Here, we are especially interested in the $1/e$ decay length of the amplitude, the distance at which the original amplitude is reduced by a factor of $1/e$. This value is computed by means of formula (4.41) given in [Fro07]. Using the fluid and substrate densities $\rho_f = 1.0$ g/cm^3 and $\rho_s = 2.4$ g/cm^3 in combination with the signal sound speed in the fluid $c_f = 1.5 \cdot 10^3$ m/s and in the substrate

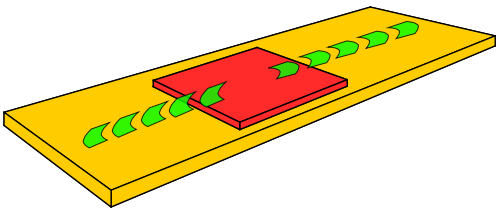

Figure 8.2: Propagation of the SAWs on the substrate layer.

$c_s = 3.9 \cdot 10^3$ m/s, the $1/e$ decay length of the intensity is given by

$$l_{e,I} = 0.45 \frac{\rho_s c_s}{\rho_f c_f} \lambda = 1.1 \cdot 10^{-4} \text{m}. \tag{8.1}$$

Consequently the $1/e$ decay length of the intensity is about 110μm. The $1/e$ decay length of the amplitude is twice as long, because $I \propto A^2$, and we get

$$I = I_0 e^{-\frac{x}{l_{e,I}}} \Rightarrow A = \sqrt{I_0 e^{-\frac{x}{l_{e,I}}}} = \sqrt{I_0} e^{-\frac{x}{2l_{e,I}}}. \tag{8.2}$$

Thus, the $1/e$ decay length of the amplitude is given by $l_{e,A} = 2.2 \cdot 10^{-4}$ m, i.e. about 220 μm. When we compare experiments and simulations, it would be helpful to directly connect the input signal, measured in dB, to the amplitude. However, this is only possible in a relative sense, because there is no information about the energetic losses on the distance between the power supply and the substrate layer.

The prescribed acoustic waves on the substrate layer further couple into the fluid. This process is highly efficient, because most of the wave energy is located within a depth about one wavelength of the substrate layer. Therefore, almost the complete wave energy is available for this purpose. There further exists a characteristic angle of radiation θ which determines how the pressure waves are sent into the fluid as shown in Figure 8.3. This angle is determined by different signal sound speeds of the fluid $c_f = 1.5 \cdot 10^3$ m/s and the substrate layer $c_s = 3.9 \cdot 10^3$ m/s. The Snellius law of refraction gives

$$\sin\theta = \frac{c_f}{c_s} \approx 22.6°. \tag{8.3}$$

After short relaxation times of up to 10^{-8} s a stationary pressure field establishes. This stationary pressure field induces acoustic streaming or

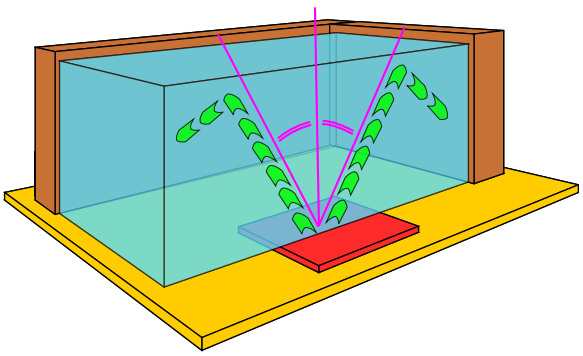

Figure 8.3: Pressure waves (green) propagating inside the water bulk with predicted angle of radiation (magenta)

Rayleigh streaming. Thus a fluid velocity field is excited by the stationary pressure field as shown in Figure 8.4. The relaxation time for such velocity fields is about 10^{-3} s. Hence, we see two processes in our setting occurring on different time scales which need to be reflected in our model for simulation. In addition to this we make out influencing parameters of the problem despite physical constants. The position and the frequency of the IDT together with the shape and the size of the fluid container influences the resulting velocity field and ultimately the setting. Concerning existing experimental data for this setting, varying fluid heights and signal powers are relevant.

8.2 Modeling the Fluidics Problem

In this section, we present a model for the problem described in section 8.1 which was originally developed in [Bra96].

Let $\Omega \subset \mathbb{R}^3$ be a bounded three-dimensional domain corresponding to the water volume inside the container presented before with boundary $\Gamma := \partial\Omega$. Further, we introduce X-, Y- and Z-direction such that a spatial point $x \in \mathbb{R}^3$ is defined by

$$x := (x_X, x_Y, x_Z) = (x_1, x_2, x_3). \tag{8.4}$$

We further use this convention of directions and numeration for different variables without explicit definition. For a given length l_X, width l_Y, and height l_Z the domain Ω reads as follows

$$\Omega := (-\frac{l_X}{2}, +\frac{l_X}{2}) \times (-\frac{l_Y}{2}, +\frac{l_Y}{2}) \times (0, l_Z). \tag{8.5}$$

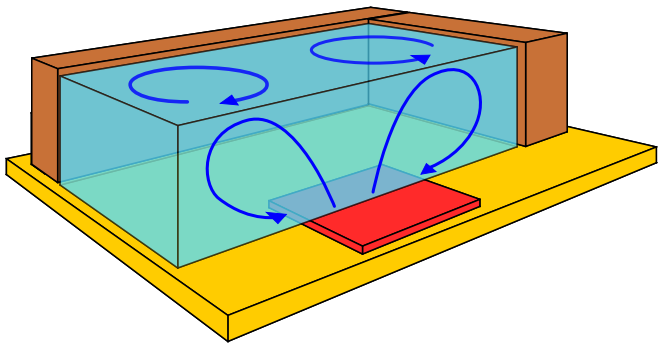

Figure 8.4: SAWs-induced streaming (blue) in the water bulk.

We assume the center of the IDT on top of the substrate layer to be at the origin $(0, 0, 0)$ of our setting. Thus the IDT related boundary region Γ_u is defined by

$$\Gamma_u := [-\frac{l_X}{2}, +\frac{l_X}{2}] \times [-w, +w] \times \{0\}, \tag{8.6}$$

where $w \in \mathbb{R}^+$, $w \ll l_Y$, denotes the width of the emitted pressure wave on the substrate layer. The condition at this boundary is prescribed later. Before, we define the top boundary of the domain by

$$\Gamma_s := [-\frac{l_X}{2}, +\frac{l_X}{2}] \times [-\frac{l_Y}{2}, +\frac{l_Y}{2}] \times \{l_Z\}. \tag{8.7}$$

At this boundary free flow is possible in X- and Y- but not in Z-direction, this means no mass transfer out of the domain is possible. Thus, we assume zero normal components of the velocity here. Later this choice allows us to compare simulated vorticity patterns at the upper boundary to experimental data. At this point we should mention that we introduced a geometric simplification of the boundary Γ_s by the definition of our domain Ω. Experimental observations suggest minimum curvature of the boundary near the point of maximum velocity of the vorticity pattern. This issue will be discussed later in section 8.4 using simulation results and experimental data. Finally, the remaining surfaces of the fluid are given by

$$\Gamma_n := \Gamma \setminus \{\Gamma_u \cup \Gamma_s\}. \tag{8.8}$$

Here, we naturally assume no-slip boundary conditions. The resulting setup and different boundaries are summarized in Figure 8.5.

Let us now consider the boundary condition on Γ_u. We have to look for a mathematical formulation of the mechanical displacement induced by

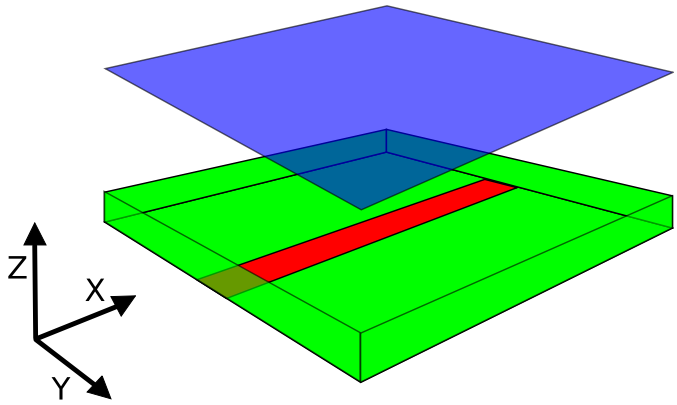

Figure 8.5: Computational domain Ω with boundary regions Γ_u (red), Γ_n (green) and Γ_s (blue).

the surface acoustic waves. There are linearized equations of piezoelectricity described in [GHK+07]. However, we use the simplified excitation from [FHLW11] showing good results. In particular, we define the function $\boldsymbol{u}(x,t) : \mathbb{R}^3 \times \mathbb{R}^+ \to \mathbb{R}^3$,

$$\boldsymbol{u}(x,t) := (u_1(x,t), u_2(x,t), u_3(x,t))^T \tag{8.9}$$

where $u_i(x,t) : \mathbb{R}^3 \times \mathbb{R}^+ \to \mathbb{R}$, $1 \leq i \leq 3$, is defined by

$$u_1(x,t) := 0.6\ u_0 \exp(-C_d x_1)\ \sin(2\pi(-kx_1 + ft)), \tag{8.10}$$

$$u_2(x,t) := 0, \tag{8.11}$$

$$u_3(x,t) := -\ u_0 \exp(-C_d x_1)\ \cos(2\pi(-kx_1 + ft)), \tag{8.12}$$

with maximum displacement u_0 from equilibrium, damping parameter $C_d = (l_{e,A})^{-1} = 4.5 \cdot 10^3\ \mathrm{m}^{-1}$, IDT frequency f, and wavenumber $k = f/c_s$ where c_s denotes the small signal sound speed inside the substrate layer.

We already mentioned the pressure waves occurring on a short time scale. In order to capture the associated compressible effects in a mathematical sense we have to choose the compressible Navier–Stokes equations. Let ρ denote the density, η the dynamic viscosity, and ξ the bulk viscosity of the fluid. We introduce the stress tensor $\boldsymbol{\sigma}$ depending on the velocity $\boldsymbol{v}(x,t) : \mathbb{R}^3 \times \mathbb{R}^+ \to \mathbb{R}^3$, the pressure $p(x,t) : \mathbb{R}^3 \times \mathbb{R}^+ \to \mathbb{R}$, and the density $\rho(x,t) : \mathbb{R}^3 \times \mathbb{R}^+ \to \mathbb{R}$ of the fluid. By $\boldsymbol{n}$ we denote the exterior normal unit vector and by $\boldsymbol{\tau}_i$, $1 \leq i \leq 2$, the unit tangential vectors on $\Gamma = \partial\Omega$. The computational domain Ω is actually time dependent, i.e. we have $\Omega(t)$ due to the time dependent boundary

$$\Gamma_u(t) := \{y \in \mathbb{R}^3 \mid y = x + \boldsymbol{u}(x,t), x \in \Gamma_u\}. \tag{8.13}$$

The boundary condition on Γ_u for the velocity of the fluid is given by

$$\boldsymbol{v}(x+\boldsymbol{u}(x,t),t) = \frac{\partial \boldsymbol{u}}{\partial t}(\cdot,t), \qquad \text{on } \Gamma_u(t),\ t\in(0,T),\ T\in\mathbb{R}^+. \tag{8.14}$$

The compressible Navier–Stokes equations are to find a triple of velocity, pressure, and density (v,p,ρ) such that

$$\rho\Big(\frac{\partial \boldsymbol{v}}{\partial t} + \boldsymbol{v}\cdot\nabla\boldsymbol{v}\Big) - \nabla\cdot\boldsymbol{\sigma}(\boldsymbol{v},p) = \boldsymbol{0} \qquad \text{in } \Omega, \tag{8.15}$$

$$\frac{\partial \rho}{\partial t} + \nabla\cdot(\rho\boldsymbol{v}) = 0 \qquad \text{in } \Omega, \tag{8.16}$$

$$p(\cdot,t) = c_f^2\rho(\cdot,t) \qquad \text{in } \Omega, \tag{8.17}$$

$$\boldsymbol{v}(x+\boldsymbol{u}(x,t),t) = \frac{\partial \boldsymbol{u}}{\partial t}(\cdot,t) \qquad \text{on } \Gamma_u(t), \tag{8.18}$$

$$\boldsymbol{v}(\cdot,t) = \boldsymbol{0} \qquad \text{on } \Gamma_n, \tag{8.19}$$

$$\boldsymbol{v}(\cdot,t)\cdot\boldsymbol{n} = 0 \qquad \text{on } \Gamma_s, \tag{8.20}$$

$$\boldsymbol{n}\cdot\boldsymbol{\sigma}(\boldsymbol{v},p)\boldsymbol{\tau}_i = 0,\ 1\le i\le 2, \qquad \text{on } \Gamma_s, \tag{8.21}$$

$$\boldsymbol{v}(\cdot,0) = \boldsymbol{0}, \qquad p(\cdot,0) = 0 \qquad \text{in } \Omega, \tag{8.22}$$

where the constitutive equation for the stress tensor $\boldsymbol{\sigma}(\boldsymbol{v},p) = \big(\boldsymbol{\sigma}(\boldsymbol{v},p)_{ij}\big)_{i,j=1}^3$ is given by

$$\boldsymbol{\sigma}_{ij}(\boldsymbol{v},p) := -p\ \delta_{ij} + 2\eta\boldsymbol{D}_{ij}(\boldsymbol{v}) + \delta_{ij}(\xi - 2\eta/3)\nabla\cdot\boldsymbol{v}. \tag{8.23}$$

Here, $\boldsymbol{D}(\boldsymbol{v})$ denotes the rate of deformation tensor $\boldsymbol{D}(\boldsymbol{v}) := (\nabla\boldsymbol{v}+(\nabla\boldsymbol{v})^T)/2$. The relation between pressure and density is established by the physical property $p = c_f^2\rho$, where c_f denotes the small signal sound speed inside the fluid.

We already mentioned the multiscale character of this problem in section 8.1. Thus we separate our problem into an acoustic subproblem at a short time scale (nanoseconds, $\sim 10^{-3}$ s) and a streaming subproblem at a longer time scale (milliseconds, $\sim 10^{-3}$ s). This homogenization approach is used for example in [AGH$^+$08, AGH$^+$10] and was first suggested in [Bra96]. The method is based on an asymptotic expansion in time with scale parameter $\varepsilon\in\mathbb{R}$, $0<\varepsilon\ll 1$. A natural choice is $\varepsilon\approx u_0/c_s$ to reflect the appropriate time scales of the problem. The resulting physical dimension of the order parameter ε is [s]. This dimension makes perfectly sense when we look at the resulting expansion for the density ρ, the velocity v, and the pressure p, given by

$$\rho = \rho^{(0)} + \varepsilon\rho' + \varepsilon^2\rho'' + \mathcal{O}(\varepsilon^3), \tag{8.24}$$

$$\boldsymbol{v} = \boldsymbol{v}^{(0)} + \varepsilon\boldsymbol{v}' + \varepsilon^2\boldsymbol{v}'' + \mathcal{O}(\varepsilon^3), \tag{8.25}$$

$$p = p^{(0)} + \varepsilon p' + \varepsilon^2 p'' + \mathcal{O}(\varepsilon^3), \tag{8.26}$$

where the prime $'$ denotes the temporal derivative and $\rho^{(0)}$, $\boldsymbol{v}^{(0)}$, $p^{(0)}$ the initial equilibrium states of the density, the velocity, and the pressure. The scale parameter conserves the dimensions. Further, it allows us to separate contributions on different time scales because the order parameter is much less than one as we see in the following lines. At first we collect terms of the same order. The first order terms, this means $\mathcal{O}(\varepsilon)$,

$$\rho^{(1)} := \varepsilon\rho', \quad \boldsymbol{v}^{(1)} := \varepsilon\boldsymbol{v}', \quad \boldsymbol{p}^{(1)} := \varepsilon p', \tag{8.27}$$

are relevant on the short time scale up to relaxation. Furthermore, the terms of second order, or $\mathcal{O}(\varepsilon^2)$,

$$\rho^{(2)} := \varepsilon^2\rho'', \quad \boldsymbol{v}^{(2)} := \varepsilon^2\boldsymbol{v}'', \quad \boldsymbol{p}^{(2)} := \varepsilon^2 p'', \tag{8.28}$$

are relevant on the longer time scale.

Now, we want to adapt the expansion to the Navier–Stokes system (8.15) – (8.22). For this purpose we apply Taylor expansion to the left-hand side of the boundary condition on Γ_u which gives

$$\boldsymbol{v}(x+\boldsymbol{u},t) = \underbrace{\boldsymbol{v}(x,t)}_{\mathcal{O}(\varepsilon)} + \underbrace{(\nabla\boldsymbol{v})\boldsymbol{u}}_{\mathcal{O}(\varepsilon^2)} + \mathcal{O}(\varepsilon^3). \tag{8.29}$$

The order of the terms is motivated by the choice of the initial equilibrium state of the velocity $\boldsymbol{v}^{(0)}$ which vanishes, i.e. $\boldsymbol{v}^{(0)} \equiv 0$. Consequently, the nonvanishing velocity $\boldsymbol{v}(x,t)$ has to be of first order and thus $(\nabla\boldsymbol{v})\boldsymbol{u}$ of second order. This is in accordance with the argumentation in [Bra96]. We further assume the initial equilibrium of the velocity $\boldsymbol{u}^{(0)}$ to vanish, i.e. $\boldsymbol{u}^{(0)} \equiv 0$. Then the Taylor expansion applied on the right-hand side of the boundary condition on Γ_u is given by

$$\boldsymbol{u}(t) = \underbrace{\boldsymbol{u}^{(0)}}_{\equiv 0} + \underbrace{\frac{\partial\boldsymbol{u}}{\partial t}}_{\mathcal{O}(\varepsilon)} + \mathcal{O}(\varepsilon^2). \tag{8.30}$$

Thus the first order approximation of the boundary condition on Γ_u is given by

$$\boldsymbol{v}^{(1)} = \frac{\partial\boldsymbol{u}}{\partial t}. \tag{8.31}$$

In doing so we neglect the deflection of Γ_u and return to a time independent domain Ω. This is an appropriate simplification because the deflection at length scales of nanometers ($\sim 10^{-9}$ m) is very small compared to the length scales of millimeters ($\sim 10^{-3}$ m) of the domain.

Finally, collecting all terms of first order of the Navier–Stokes system (8.15) – (8.22), results in the time-periodic compressible Stokes equations

$$\rho^{(0)}\frac{\partial \boldsymbol{v}^{(1)}}{\partial t} - \nabla\cdot\boldsymbol{\sigma}(\boldsymbol{v}^{(1)},p^{(1)}) = \boldsymbol{f}_{\boldsymbol{v}}^{(1)}, \qquad \text{in } \Omega, \tag{8.32}$$

$$\frac{\partial \rho^{(1)}}{\partial t} + \rho^{(0)}\nabla\cdot\boldsymbol{v}^{(1)} = f_p^{(1)}, \qquad \text{in } \Omega, \tag{8.33}$$

$$p^{(1)}(\cdot,t) = c_f^2\rho^{(1)}(\cdot,t) \qquad \text{in } \Omega, \tag{8.34}$$

$$\boldsymbol{v}^{(1)}(\cdot,t) = \boldsymbol{g}^{(1)}(\cdot,t), \qquad \text{on } \Gamma_u. \tag{8.35}$$

$$\boldsymbol{v}^{(1)}(\cdot,t) = \boldsymbol{0}, \qquad \text{on } \Gamma_n, \tag{8.36}$$

$$\boldsymbol{v}^{(1)}(\cdot,t)\cdot\boldsymbol{n} = 0 \qquad \text{on } \Gamma_s, \tag{8.37}$$

$$\boldsymbol{n}\cdot\boldsymbol{\sigma}(\boldsymbol{v}^{(1)},p^{(1)})\boldsymbol{\tau}_i = 0,\ 1\le i\le 2, \qquad \text{on } \Gamma_s, \tag{8.38}$$

$$\boldsymbol{v}^{(1)}(\cdot,0) = \boldsymbol{v}^{(1)}(\cdot,T_f), \quad p^{(1)}(\cdot,0) = p^{(1)}(\cdot,T_f) \qquad \text{in } \Omega, \tag{8.39}$$

with periodicity $T_f := 1/f$, where f denotes the IDT frequency, and

$$\boldsymbol{f}_{\boldsymbol{v}}^{(1)} = \boldsymbol{0}, \qquad f_p^{(1)} = 0, \qquad \boldsymbol{g}^{(1)}(\cdot,t) = \frac{\partial \boldsymbol{u}}{\partial t}(\cdot,t). \tag{8.40}$$

This system is called acoustic subproblem and incorporates IDT actuated effects on a short time scale. The corresponding initial value problem quickly reaches a quasi-equilibrium solution due to the harmonic surface acoustic wave oscillation which is modeled at the boundary Γ_u using the time periodic function $\boldsymbol{u}$. Therefore, in practice it is convenient to start with zero initial condition, i.e.

$$\boldsymbol{v}^{(1)}(\cdot,0) = \boldsymbol{0}, \quad p^{(1)}(\cdot,0) = 0 \qquad \text{in } \Omega, \tag{8.41}$$

and to propagate in time until relaxation sets in which means the equilibrium solution is nearly reached. A measure for relaxation at a given time t_r is the averaged difference between the current and the prior pressure field over one period T_f. The simulation stops when the difference is below a given tolerance $\epsilon_{\text{tol}} \in \mathbb{R}$, $\epsilon_{\text{tol}} > 0$, such that

$$\frac{1}{T_f\|p^{(1)}(T_f)\|_{0,\Omega}}\Big(\int_{t_r-T_f}^{t_r}\left(p^{(1)}(t)-p^{(1)}(t-T_f)\right)^2\,\mathrm{d}t\Big)^{1/2} \le \epsilon_{\text{tol}}. \tag{8.42}$$

We refer to [Kös06] for more details concerning this procedure.

After relaxation of the acoustic subproblem (8.32) – (8.39) at time t_r we use the resulting first order terms to derive the known terms at second order which serve as right-hand side of the system of equations related to the second order terms. For this purpose, we define the averaging operator

$$\langle\cdot\rangle := T_f^{-1}\int_{t_r-T_f}^{t_r}\cdot\,\mathrm{d}t, \tag{8.43}$$

such that

$$\begin{aligned} \boldsymbol{f}_{\boldsymbol{v}}^{(2)} &= \Big\langle -\rho^{(1)} \frac{\partial \boldsymbol{v}^{(1)}}{\partial t} - \rho^{(0)} (\nabla \boldsymbol{v}^{(1)}) \boldsymbol{v}^{(1)} \Big\rangle \\ &= \Big\langle + \frac{\partial \rho^{(1)}}{\partial t} \boldsymbol{v}^{(1)} - \rho^{(0)} (\nabla \boldsymbol{v}^{(1)}) \boldsymbol{v}^{(1)} \Big\rangle \\ &= \Big\langle -\rho^{(0)} (\nabla \cdot \boldsymbol{v}^{(1)}) \boldsymbol{v}^{(1)} - \rho^{(0)} (\nabla \boldsymbol{v}^{(1)}) \boldsymbol{v}^{(1)} \Big\rangle, \end{aligned} \tag{8.44}$$

$$f_p^{(2)} = \Big\langle -\nabla \cdot (\rho^{(1)} \boldsymbol{v}^{(1)}) \Big\rangle, \tag{8.45}$$

$$\boldsymbol{g}^{(2)} = \Big\langle -(\nabla \boldsymbol{v}^{(1)}) \boldsymbol{u} \Big\rangle. \tag{8.46}$$

As a next step we collect all unknown terms of second order of the Navier–Stokes system (8.15) – (8.22) which are relevant for long time effects, the acoustic streaming. The resulting instationary compressible Stokes equations which are called streaming subproblem, reads

$$\rho^{(0)} \frac{\partial \boldsymbol{v}^{(2)}}{\partial t} - \nabla \cdot \boldsymbol{\sigma}(\boldsymbol{v}^{(2)}, p^{(2)}) = \boldsymbol{f}_{\boldsymbol{v}}^{(2)} \qquad \text{in } \Omega, \tag{8.47}$$

$$\frac{\partial \rho^{(2)}}{\partial t} + \rho^{(0)} \nabla \cdot \boldsymbol{v}^{(2)} = f_p^{(2)} \qquad \text{in } \Omega, \tag{8.48}$$

$$p^{(2)}(\cdot, t) = c_f^2 \rho^{(2)}(\cdot, t) \qquad \text{in } \Omega, \tag{8.49}$$

$$\boldsymbol{v}^{(2)}(\cdot, t) = \boldsymbol{g}^{(2)}(\cdot, t) \qquad \text{on } \Gamma_u, \tag{8.50}$$

$$\boldsymbol{v}^{(2)}(\cdot, t) = \boldsymbol{0} \qquad \text{on } \Gamma_n, \tag{8.51}$$

$$\boldsymbol{v}^{(2)}(\cdot, t) \cdot \boldsymbol{n} = 0 \qquad \text{on } \Gamma_s, \tag{8.52}$$

$$\boldsymbol{n} \cdot \boldsymbol{\sigma}(\boldsymbol{v}^{(2)}, p^{(2)}) \boldsymbol{\tau}_i = 0,\ 1 \le i \le 2, \qquad \text{on } \Gamma_s, \tag{8.53}$$

$$\boldsymbol{v}^{(2)}(\cdot, 0) = \boldsymbol{0}, \qquad p^{(2)}(\cdot, 0) = 0, \qquad \text{in } \Omega. \tag{8.54}$$

Concerning existence and uniqueness, we refer to [Kös07] and focus on the details of the implementation in the following section.

8.3 Implementation Issues

In the following lines we present details of implementation for the previously presented fluid model in section 8.2. For simplicity, we skip the initial conditions and the slip, respectively no-slip boundary conditions on Γ_s and Γ_n for the moment. The acoustic subproblem (8.32) – (8.39) and the streaming subproblem (8.32) – (8.39) is to find a velocity and pressure pair $(\boldsymbol{v}^{(i)}, p^{(i)})$

such that

$$\rho^{(0)}\frac{\partial \boldsymbol{v}^{(i)}}{\partial t} - \nabla\cdot\boldsymbol{\sigma}(\boldsymbol{v}^{(i)},p^{(i)}) = \boldsymbol{f}_{\boldsymbol{v}}^{(i)} \qquad \text{in } \Omega, \tag{8.55}$$

$$\frac{1}{c_f^2}\frac{\partial p^{(i)}}{\partial t} + \rho^{(0)}\nabla\cdot\boldsymbol{v}^{(i)} = f_p^{(i)} \qquad \text{in } \Omega, \tag{8.56}$$

$$\boldsymbol{v}^{(i)}(\cdot,t) = \boldsymbol{g}^{(i)} \qquad \text{on } \Gamma_u, \tag{8.57}$$

for $1 \le i \le 2$, where we used $p^{(i)} = c_f^2\rho^{(i)}$ (cf. (8.34) and (8.49)). Further, we resolve the stress tensor $\boldsymbol{\sigma}$,

$$\nabla\cdot\boldsymbol{\sigma}(\boldsymbol{v}^{(i)},p^{(i)}) = \eta\nabla^2\boldsymbol{v}^{(i)} + (\xi - 2\eta/3)\nabla(\nabla\cdot\boldsymbol{v}^{(i)}) - \nabla p, \tag{8.58}$$

and use the kinematic viscosities $\nu_1 := \eta/\rho^{(0)}$, $\nu_2 := (\xi - 2\eta/3)/\rho^{(0)}$. Applying the relative pressure $\tilde{p}^{(i)} := p^{(i)}/\rho^{(0)}$ to (8.55) – (8.57) we have to compute $(\boldsymbol{v}^{(i)},\tilde{p}^{(i)})$ such that

$$\frac{\partial \boldsymbol{v}^{(i)}}{\partial t} - \nu_1\nabla^2\boldsymbol{v}^{(i)} - \nu_2\nabla(\nabla\cdot\boldsymbol{v}^{(i)}) + \nabla\tilde{p}^{(i)} = \frac{1}{\rho^{(0)}}\boldsymbol{f}_{\boldsymbol{v}}^{(i)} \qquad \text{in } \Omega, \tag{8.59}$$

$$\frac{1}{c_f^2}\frac{\partial \tilde{p}^{(i)}}{\partial t} + \nabla\cdot\boldsymbol{v}^{(i)} = \frac{1}{\rho^{(0)}}f_p^{(i)} \qquad \text{in } \Omega, \tag{8.60}$$

$$\boldsymbol{v}^{(i)}(\cdot,t) = \boldsymbol{g}^{(i)} \qquad \text{on } \Gamma_u, \tag{8.61}$$

for $1 \le i \le 2$, where the appropriate right-hand sides are given by

$$\frac{1}{\rho^{(0)}}\boldsymbol{f}_{\boldsymbol{v}}^{(1)} = \boldsymbol{0}, \qquad \frac{1}{\rho^{(0)}}f_p^{(1)} = 0, \qquad \boldsymbol{g}^{(1)} = \frac{\partial \boldsymbol{u}}{\partial t}(\cdot,t), \tag{8.62}$$

and

$$\frac{1}{\rho^{(0)}}\boldsymbol{f}_{\boldsymbol{v}}^{(2)} = \Big\langle -(\nabla\cdot\boldsymbol{v}^{(1)})\boldsymbol{v}^{(1)} - (\nabla\boldsymbol{v}^{(1)})\boldsymbol{v}^{(1)}\Big\rangle, \tag{8.63}$$

$$\frac{1}{\rho^{(0)}}f_p^{(2)} = \Big\langle -\frac{1}{c_f^2}\nabla\cdot(\tilde{p}^{(1)}\boldsymbol{v}^{(1)})\Big\rangle, \tag{8.64}$$

$$\boldsymbol{g}^{(2)} = \Big\langle -(\nabla\boldsymbol{v}^{(1)})\boldsymbol{u}\Big\rangle. \tag{8.65}$$

For reasons of stability we further use a dimensionless formulation suggested in [Kös07] and introduce scaling dimensions for space and time, L and T. The procedure was deferred to this section because it is closely connected to the numerical stability of the resulting system of equations rather than the method itself. This allowed us to reduce the technical complexity in the previous section. Consequently, we introduce dimensionless coordinates in space and time such that

$$x \to L\hat{x}, \quad t \to T\hat{t}, \tag{8.66}$$

and we thus get the dimensionless operators and variables

$$\nabla = \frac{1}{L}\hat{\nabla}, \quad \frac{\partial}{\partial t} = \frac{1}{T}\frac{\partial}{\partial \hat{t}}, \quad \tilde{p} = \frac{L^2}{T^2}\hat{p}, \quad \boldsymbol{u} = L\hat{\boldsymbol{u}}. \tag{8.67}$$

Furthermore, we define $V := L/T$ which is important to preserve the dimensions, and introduce the dimensionless velocity

$$\boldsymbol{v} \to V\hat{\boldsymbol{v}}. \tag{8.68}$$

Subsequently, our simplified acoustic subproblem is to find a dimensionless velocity and pressure pair $(\hat{\boldsymbol{v}}^{(1)}, \hat{p}^{(1)})$ such that

$$\frac{VT}{L}\frac{\partial \hat{\boldsymbol{v}}^{(1)}}{\partial t} - \frac{VT^2}{L^3}\Big(\nu_1\hat{\nabla}^2\hat{\boldsymbol{v}}^{(1)} + \nu_2\hat{\nabla}(\hat{\nabla}\cdot\hat{\boldsymbol{v}}^{(1)})\Big) + \hat{\nabla}\hat{p}^{(1)} = \boldsymbol{0} \quad \text{in } \Omega, \tag{8.69}$$

$$\frac{L^3}{c_f^2 VT^3}\frac{\partial \hat{p}^{(1)}}{\partial t} + \hat{\nabla}\cdot\hat{\boldsymbol{v}}^{(1)} = 0 \quad \text{in } \Omega, \tag{8.70}$$

$$\frac{VT}{L}\hat{\boldsymbol{v}}^{(1)}(\cdot,t) = \frac{\partial \hat{\boldsymbol{u}}}{\partial \hat{t}} \quad \text{on } \Gamma_u. \tag{8.71}$$

Analogously, our simplified acoustic subproblem is to find a pair $(\hat{\boldsymbol{v}}^{(2)}, \hat{p}^{(2)})$ such that

$$\begin{aligned}\frac{VT}{L}\frac{\partial \hat{\boldsymbol{v}}^{(2)}}{\partial t} - \frac{VT^2}{L^3}\Big(\nu_1\hat{\nabla}^2\hat{\boldsymbol{v}}^{(2)} + \nu_2\hat{\nabla}(\hat{\nabla}\cdot\hat{\boldsymbol{v}}^{(2)})\Big) + \hat{\nabla}\hat{p}^{(2)} = \\ \frac{T^2V^2}{L^2}\Big\langle -(\hat{\nabla}\cdot\boldsymbol{v}^{(1)})\boldsymbol{v}^{(1)} - (\hat{\nabla}\boldsymbol{v}^{(1)})\boldsymbol{v}^{(1)}\Big\rangle \quad \text{in } \Omega,\end{aligned} \tag{8.72}$$

$$\frac{L^3}{c_f^2 VT^3}\frac{\partial \hat{p}^{(2)}}{\partial t} + \hat{\nabla}\cdot\hat{\boldsymbol{v}}^{(2)} = \frac{L^2}{c_f^2T^2}\Big\langle -\hat{\nabla}\cdot(\hat{p}^{(1)}\hat{\boldsymbol{v}}^{(1)})\Big\rangle \quad \text{in } \Omega, \tag{8.73}$$

$$\hat{\boldsymbol{v}}^{(2)}(\cdot,t) = \Big\langle -(\hat{\nabla}\hat{\boldsymbol{v}}^{(1)})\hat{\boldsymbol{u}}\Big\rangle \quad \text{on } \Gamma_u. \tag{8.74}$$

For both subproblems we use the dimensionless deflection function $\hat{\boldsymbol{u}}(x,t) : \mathbb{R}^3 \times \mathbb{R}^+ \to \mathbb{R}^3$,

$$\hat{\boldsymbol{u}}(\hat{x},\hat{t}) := (\hat{u}_1(\hat{x},\hat{t}), (\hat{u}_2(\hat{x},\hat{t}), (\hat{u}_3(\hat{x},\hat{t}))^T, \tag{8.75}$$

with $\hat{u}_i(\hat{x},\hat{t}) : \mathbb{R}^3 \times \mathbb{R}^+ \to \mathbb{R}$,

$$\hat{u}_1(\hat{x},\hat{t}) := 0.6\ \hat{u}_0 \exp(-LC_d\hat{x}_1)\ \sin\big(2\pi(-Lk\hat{x}_1 + Tf\hat{t}\ )\big), \tag{8.76}$$

$$\hat{u}_2(\hat{x},\hat{t}) := 0, \tag{8.77}$$

$$\hat{u}_3(\hat{x},\hat{t}) := -\hat{u}_0 \exp(-LC_d\hat{x}_1)\ \cos\big(2\pi(-Lk\hat{x}_1 + Tf\hat{t}\ )\big) \tag{8.78}$$

with dimensionless deflection parameter $\hat{u}_0 = u_0/L$ and wavenumber $k = f/c_s$.

The problems are discretized using Taylor-Hood P2/P1 elements [BF91]. Let $\mathcal{T}_h(\Omega)$ be a conforming simplicial triangulation of Ω. Then, the finite element spaces $\boldsymbol{V}_h$ for the velocity and Q_h for the pressure are given by

$$\boldsymbol{V}_h := \{\boldsymbol{v}_h \in \boldsymbol{C}(\bar{\Omega}) \mid \boldsymbol{v}_h|_K \in P_2(K)^2, K \in \mathcal{T}_h(\Omega),\ \boldsymbol{v}_h|_{\Gamma_n} = \boldsymbol{0}\}, \tag{8.79}$$

$$Q_h := \{q_h \in C(\bar{\Omega}) \mid q_h|_K \in P_1(K), K \in \mathcal{T}_h(\Omega),\ \int_\Omega q_h \,\mathrm{d}x = 0\}, \tag{8.80}$$

where $P_k(K)$, $k \in \mathbb{N}$, denotes the set of polynomials of degree less or equal k for elements $K \in \mathcal{T}_h(\Omega)$. Using these definitions the semi-discrete weak formulation of the Stokes equations (8.55) – (8.57) at time $t \in (0, T)$, $T \in \mathbb{R}^+$, is to find a pair $(\boldsymbol{v}_h^{(i)}, p_h^{(i)}) \in \boldsymbol{V}_h \times Q_h$, $1 \leq i \leq 2$, such that there holds

$$\begin{aligned} &\rho^{(0)} \int_\Omega \frac{\partial \boldsymbol{v}_h^{(i)}}{\partial t} \boldsymbol{w}_h \,\mathrm{d}x + \nu_1 \int_\Omega \nabla \boldsymbol{v}_h^{(i)} : \nabla \boldsymbol{w}_h \,\mathrm{d}x \\ &+\nu_2 \int_\Omega \nabla \cdot \boldsymbol{v}_h^{(i)} \nabla \cdot \boldsymbol{w}_h \,\mathrm{d}x - \int_\Omega p_h \,\nabla \cdot \boldsymbol{w}_h \,\mathrm{d}x = \int_\Omega \boldsymbol{f}_v^{(i)} \boldsymbol{w}_h \,\mathrm{d}x, \quad \boldsymbol{w}_h \in \boldsymbol{V}_h, \end{aligned} \tag{8.81}$$

$$\frac{1}{c_f^2} \int_\Omega \frac{\partial p_h^{(i)}}{\partial t} q_h \,\mathrm{d}x + \rho^{(0)} \int_\Omega \nabla \cdot \boldsymbol{v}_h^{(i)} q_h \,\mathrm{d}x = \int_\Omega f_p^{(i)} q_h \,\mathrm{d}x, \quad q_h \in Q_h, \tag{8.82}$$

where we omitted the boundary conditions on $\boldsymbol{v}_h^{(i)}$ for simplicity. The system is further discretized in time using the backward Euler or Crank–Nicolson scheme.

The resulting algebraic system is solved by a *generalized minimal residual* (GMRES) method supported by the *Portable, Extensible Toolkit for Scientific computation* (PETSc), where we used the provided *algebraic multigrid* (AMG) preconditioner.

Here, we have to mention the decisive role of the triangulation. We observed that the pressure wave radiation angle described in section 8.1 depends on the triangulation of our domain, e.g. [Lin14]. The usage of unstructured meshes, so-called jiggled meshes, see Figure 8.6, solves this problem. In this case the fineness of the triangulation $\mathcal{T}_h(\Omega)$ is specified by the maximum length $h_{\max}$, such that for all edges ∂K of an element $K \in \mathcal{T}_h(\Omega)$, there holds $\partial K \leq h_{\max}$.

We implemented the method using the programming language *Python* [vRdB91] and different libraries, particularly the mathematical libraries *NumPy* and *SciPy* [Oli07], and the finite element library *FEniCS* [LMWea12]. The resulting data was further analyzed and visualized using *ParaView* [Hen12]. Additional development of the code, e.g. enabling large scale computations for large domains on parallel systems, was performed by Felix Linder [Lin14].

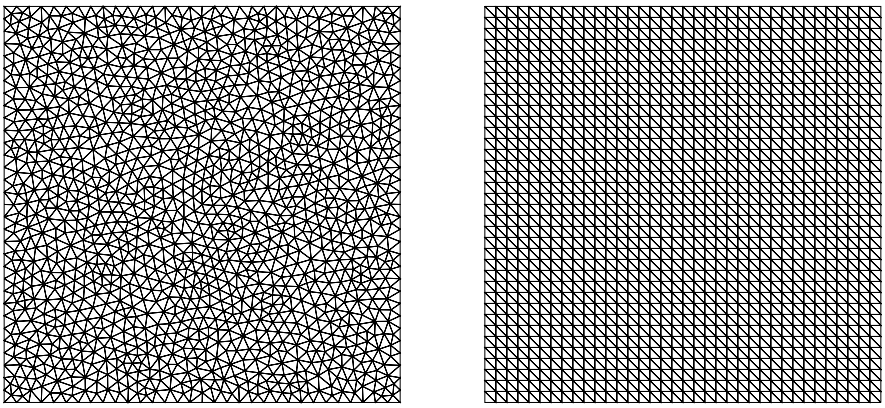

Figure 8.6: Jiggled mesh (left) and structured mesh (right) of a unit square domain using a comparable number of vortices and cells.

8.4 Simulation Results

A major advantage using the *FEniCS* library is that the resulting code is dimension-independent, i.e. it can be used for two- or three-dimensional simulations only depending on the given geometry of the problem. This allows us to validate the implementation with existing two-dimensional results from [Kös07], see [Lin14]. The code was originally developed for two-dimensional problems by the present author. Based on this version the implementation for parallel systems and the computation of three-dimensional setups was the topic of a master thesis [Lin14] co-supervised by the present author. The current code is a maintained and extended version developed by the present author.

We performed three-dimensional simulations using the constants and parameters given in table 8.1 for simulation. The resolution of the surface acoustic waves demands dense meshes, and thus requires large amounts of physical memory for the necessary degrees of freedom. Consequently we show results for a geometric setting with reduced proportions. A possible resort is to compute the acoustic subproblem on a subdomain with a fine mesh which is given by the direction of the pressure waves and the damping parameter. The resulting force field can be used for the acoustic streaming on a larger domain with a coarse mesh.

The numerical results of the three-dimensional acoustic subproblem and the acoustic streaming are illustrated in Figure 8.7. As we previously described in Figure 8.3 and Figure 8.4 the pressure waves propagate into the water bulk and the acoustic streaming causes fluid flow which leads to two mirrored circular vortices. These transport fluid from above the IDT to the water surface and vice versa. Here, the fluid flow is determined by the

Category/Name	Symbol	Unit	Value
Scaling			
Space	L	m	$1.0 \cdot 10^{-7}$
Time	T	s	$1.0 \cdot 10^{-8}$
Velocity	V	m/s	$1.0 \cdot 10^{-1}$
Discretization			
Maximum Grid Size	$h_{\max}$	m	$7.4 \cdot 10^{-6}$
Time Step Sizes			
acoustic subproblem	Δt_a	s	$6.1 \cdot 10^{-10}$
streaming subproblem	Δt_s	s	$1.0 \cdot 10^{-4}$
Domain			
Length	l_X	m	$1.0 \cdot 10^{-4}$
Width	l_Y	m	$1.0 \cdot 10^{-4}$
Height	l_Z	m	$3.0 \cdot 10^{-5}$
IDT/Substrate Layer			
Deflection	u_0	m	$1.0 \cdot 10^{-9}$
Signal Sound Speed	c_s	m/s	$3.8 \cdot 10^{+3}$
Damping ($\frac{1}{e}$)	C_d	1/m	$4.5 \cdot 10^{+3}$
Emission Width	w	m	$1.5 \cdot 10^{-5}$
Frequency	f	Hz	$1.0 \cdot 10^{+8}$
Wavenumber	k	1/m	$2.6 \cdot 10^{+4}$
Fluid (Water 25°C)			
Density	$\rho^{(0)}$	kg/m^3	$1.0 \cdot 10^{+3}$
Signal Sound Speed	c_f	m/s	$1.5 \cdot 10^{+3}$
Dynamic Viscosity	η	Pa · s	$1.0 \cdot 10^{-3}$
Bulk Viscosity	ξ	Pa · s	$2.5 \cdot 10^{-3}$
Kinematic Viscosities	ν_1	m^2/s	$1.0 \cdot 10^{-6}$
	ν_2	m^2/s	$1.8 \cdot 10^{-6}$

Table 8.1: Constants and parameters for SAW-generated fluid flow.

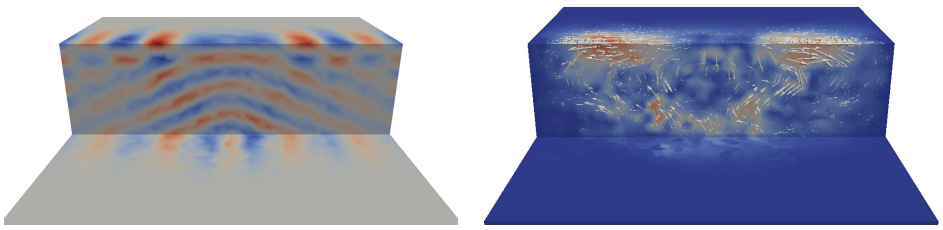

Figure 8.7: Stationary pressure wave pattern of the acoustic subproblem (left) and stationary velocity field of the acoustic streaming (right). The water bulk is cut in the X-Z-plane, see section 8.2, incorporating the origin of the domain. [Lin14]

direction of propagation of the pressure waves.

The main interest of the numerical investigation is dedicated to the vorticity pattern on top of the water bulk which was previously defined as Γ_s in section 8.2. The numerical results are illustrated in Figure 8.9 together with experimental data which was obtained by S. Burger [Bur13]. Both experiment and simulation show four counter-rotating vortices which qualitatively match in orientation and the out-going streamlines show the highest velocity flow whereas the in-going streamlines are much slower. Besides this qualitative matching the experimental vortices are more elliptic compared to the simulated streamlines. This difference may be caused by the afore-mentioned reduced computational setting. However, the qualitative agreement suggests that the model and the implementation can be used for further investigations.

A question arising from experiments is whether the experimental velocity field is divergence-free. This property cannot be computed directly using the experimental data. The available data was measured using a lipid monolayer on top of the water bulk. The idea was to use the lipid domains inside the monolayer as velocity tracers but a disadvantage of this method is that the monolayer shades properties of the underlying fluid flow field. However, knowledge about the divergence of the vorticity pattern of the fluid flow field in the absence of a lipid monolayer is relevant for the understanding why particles propagate towards the center of a vortex while rotating in it. Consequently we analyzed the numerical results because the direct measurement of the inner flow field in experiments is a demanding, work-intensive task. Thereby we revealed indeed that fluid is transported at the center of the vortices to the ground of the water bulk and back to the IDT again, see Figure 8.8. Once it has arrived at the bottom the fluid is lifted to the top again following the pressure waves. On the basis of this information we have to expect the same phenomena in the experimental setup. This explains the experimentally observed minimal deflection at the water surface in this region. Consequently the SAW-generated vorticity pattern on top

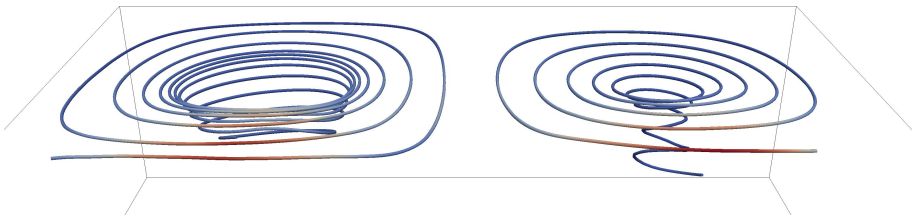

Figure 8.8: Trajectories starting on top of the water bulk and descending to the ground while rotating closer to the center of the vortices. [Lin14].

of the water bulk is not divergence free. In the following chapter 9 we assume the two-dimensional velocity field at the water surface to be divergence free for the fictitious domain Lagrange multiplier method. Thus, we cannot simply use the experimental and simulated velocity field for this purpose. Consequently, we take a different approach using a velocity field generated by a quadrupolar force density described later in subsection 9.4.2. On one hand, the resulting vorticity pattern reflects the characteristic streamlines of the experimental velocity field. On the other hand, enantiomer separation is predicted for such patterns from a theoretical point of view, see [KSTH06]. These properties makes the quadrupolar force density look like a promising candidate for the following investigation of enantiomer separation.

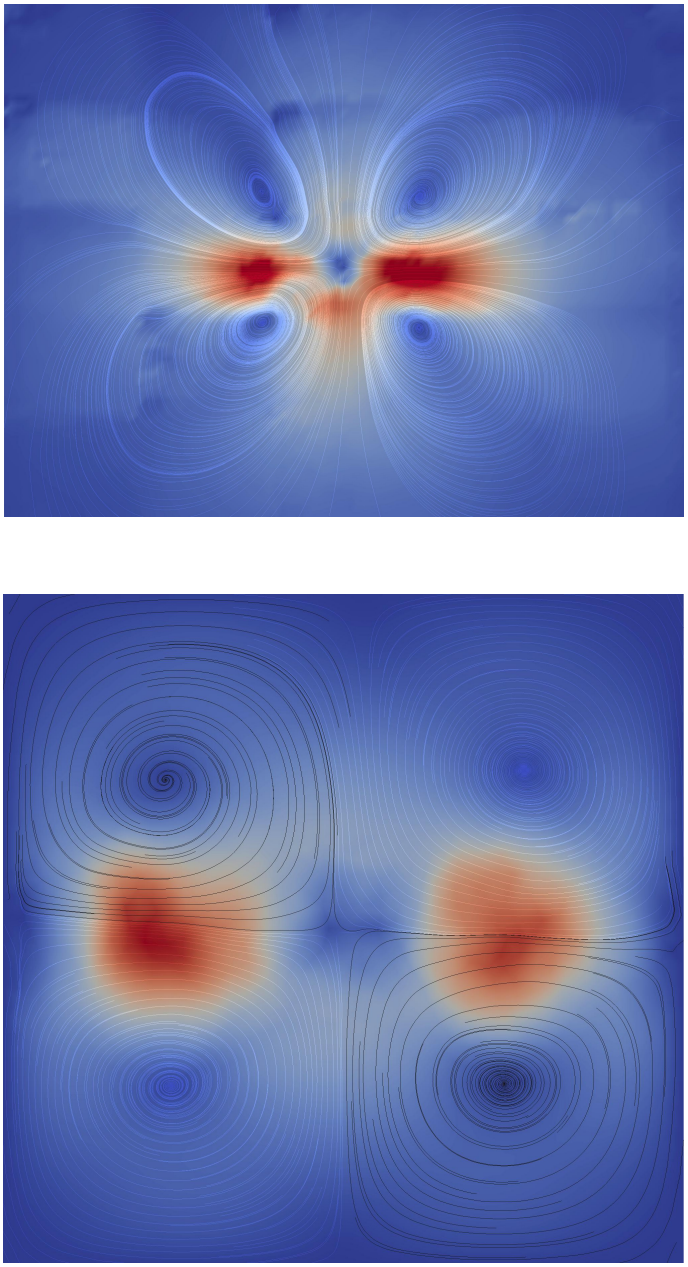

Figure 8.9: Vorticity pattern on top of the water bulk in experiment [Bur13] (top) and simulation [Lin14] (bottom).

Chapter 9

Fictitious Domain Lagrange Multiplier Method

Fictitious domain (FD) methods have been known for quite a while and we give a brief introduction to this concept in section 9.1. Subsequently, we present the *fictitious domain Lagrange multiplier* (FDLM) method described in [GPH+01] for rigid body motion in fluids. The model is derived in section 9.2 and the resulting numerical method is presented in section 9.3. Afterwards we perform numerical simulations of particle propagation in fluid microflows in section 9.4, discuss the influence of different vorticity patterns and compare the simulation results to experimental data. Thereby our special focus lies on the separation of enantiomers.

9.1 Fictitious Domains

Let us first give a brief historical introduction to *fictitious domains* (FD) inspired by [GPHJ99]. A FD method was first proposed in [Hym52] for *"... numerical solution of boundary-value problems ... applicable to arbitrary regions ..."*. The term itself was introduced in [Sau63]. The method was motivated to solve a problem on geometrically complex or even time-dependent domains on larger and much simpler fictitious domains. Thus, the method is also called domain embedding method. The idea was to use existing fast solution methods on regular meshes or to use fixed meshes for time-dependent domains. Consequently, mesh generation is simplified and even remeshing and reassembling of matrices is avoided for time-dependent domains. However, the boundary conditions of the original problem have to be enforced, for example using Lagrangian multipliers.

We derive a fictitious domain Lagrangian multiplier method for the Poisson equation. The example is taken from [GPP94] and serves as an outline for the problem described in the following section. It demonstrates the basic ingredients of the method without getting lost in technical details. Let

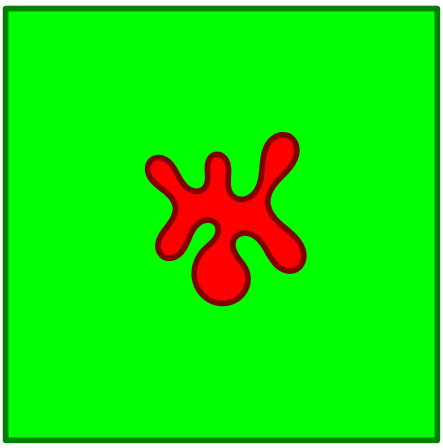

Figure 9.1: Fictitious domain Ω (green) with boundary Γ (dark green) and embedded domain ω (red) with boundary γ (dark red).

$\omega \subset \mathbb{R}^2$ be a bounded domain with Lipschitz-continuous boundary $\gamma := \partial\omega$. For $f \in L^2(\omega)$ and $g \in H^{\frac{1}{2}}(\gamma)$ the Dirichlet problem is finding a solution u, such that

$$-\Delta u = f \qquad \text{in } \omega, \tag{9.1}$$

$$u = g \qquad \text{on } \gamma. \tag{9.2}$$

There exists a unique solution $u \in V_g := \{v \in H^1(\omega) \mid v = g \text{ on } \gamma\}$ of the resulting variational formulation

$$\int_\omega \nabla u \, \nabla v \;\; \mathrm{d}x = \int_\omega f v \;\; \mathrm{d}x, \qquad \forall v \in H_0^1(\omega). \tag{9.3}$$

We further introduce a surrounding fictitious domain $\Omega \subset \mathbb{R}^2$ of simple regular geometry, e.g. a square, such that $\omega \subset\subset \Omega$. An example of such a setting is given in Figure 9.1. Let $\tilde{f} \subset L^2(\Omega)$ be an arbitrary extension of f such that $\tilde{f}|_\omega = f$. We define the Lagrangian functional $\mathcal{L} : H_0^1(\Omega) \times H^{-\frac{1}{2}}(\gamma) \to \mathbb{R}$,

$$\mathcal{L}(v, \lambda) = \frac{1}{2} \int_\Omega |\nabla v|^2 \, \mathrm{d}x - \int_\Omega \tilde{f} v \, \mathrm{d}x - \int_\gamma \lambda (v - g) \, \mathrm{d}s. \tag{9.4}$$

Using this functional we observe that the variational problem (9.3) is equivalent to finding a solution $(\tilde{u}, \lambda) \in H_0^1(\Omega) \times H^{-\frac{1}{2}}(\gamma)$ of the following saddle-point problem:

$$\int_\Omega \nabla \tilde{u} \, \nabla v \, \mathrm{d}x = \int_\Omega \tilde{f} v \, \mathrm{d}x + \int_\gamma \lambda v \, \mathrm{d}s, \qquad \forall v \in H_0^1(\Omega), \tag{9.5}$$

$$\int_\gamma \mu (\tilde{u} - g) \, \mathrm{d}s = 0, \qquad \forall \mu \in H^{-\frac{1}{2}}(\gamma). \tag{9.6}$$

The resulting solution fulfills $\tilde{u}|_\omega = u$ in ω and $u = g$ on γ. We solve the resulting saddle-point problem by a general conjugate gradient algorithm described in [GLT89]. We start with an arbitrary initial Lagrangian $\lambda^0 \in L^2(\gamma)$ and arrive at an initial solution $\tilde{u}^0 \in H_0^1(\Omega)$ such that

$$\int_\Omega \nabla\tilde{u}^0 \, \nabla v \, \mathrm{d}x = \int_\Omega \tilde{f} v \, \mathrm{d}x + \int_\gamma \lambda^0 v \, \mathrm{d}s, \qquad \forall v \in H_0^1(\Omega). \tag{9.7}$$

Subsequently, we have to find $g^0 \in L^2(\gamma)$ such that

$$\int_\gamma g^0 \mu \, \mathrm{d}s = \int_\gamma (u^0 - g)\mu \, \mathrm{d}s, \qquad \forall \mu \in L^2(\gamma). \tag{9.8}$$

Finally, we set $w^0 = g^0$ and begin with the iteration. Now, for $n \geq 0$ we proceed with the step $n \to n+1$. First, we solve for $\bar{u}^n \in H_0^1(\Omega)$

$$\int_\Omega \nabla\bar{u}^n \, \nabla v \, \mathrm{d}x = \int_\gamma w^n v \, \mathrm{d}s, \tag{9.9}$$

and compute ρ^n according to

$$\rho^n = \frac{\int_\gamma |g^n|^2 \, \mathrm{d}s}{\int_\gamma \bar{u}^n w^n \, \mathrm{d}s}. \tag{9.10}$$

We thus get the iterates

$$\lambda^{n+1} = \lambda^n - \rho^n w^n, \tag{9.11}$$

$$\tilde{u}^{n+1} = u^n - \rho^n \bar{u}^n, \tag{9.12}$$

and further have to find $g^{n+1} \in L^2(\gamma)$ such that

$$\int_\gamma g^{n+1}\mu \, \mathrm{d}s = \int_\gamma g^n \mu \, \mathrm{d}s - \rho^n \int_\gamma \bar{u}^n \mu \, \mathrm{d}s, \qquad \forall \mu \in L^2(\gamma). \tag{9.13}$$

If for a given tolerance $\epsilon \in \mathbb{R}^+$

$$\|g^{n+1}\|_{L^2(\gamma)} / \|g^0\|_{L^2(\gamma)} \leq \epsilon, \tag{9.14}$$

we stop the iteration with the solution $\lambda = \lambda^n$ and $\tilde{u} = \tilde{u}^n$. If not, we compute

$$\gamma^n = \frac{\|g^{n+1}\|^2_{L^2(\gamma)}}{\|g^n\|^2_{L^2(\gamma)}}, \tag{9.15}$$

$$w^{n+1} = g^{n+1} + \gamma^n w^n, \tag{9.16}$$

and start above, proceeding with $n \to n+1$.

A straightforward discretization is given in [GLT89]. We basically see how the FDLM method is applied to a simple problem using a CG algorithm. In the following section, we apply this method to a more complex setting, i.e. the problem of fluid–particle interaction presented in section 7.2.

9.2 Modeling Rigid Body Motion in Fluids

Fictitious domain methods for incompressible viscous unsteady flow around moving rigid particles have been developed in a series of papers in the 90s, for example [GPP98, GPHJ99]. These methods allow the efficient simulation of large numbers of particles in fluid flow, like in case of sedimentation. We have already considered some major advantages of this method in the previous section. It allows us computations on a fixed mesh by imposing the particle properties to the fluid using distributed Lagrange multipliers. However, we have to mention the existence of other methods for this purpose. The *immersed boundary* (IB) method for the simulation of deformable, viscoelastic objects in incompressible viscous flow was introduced by [Pes77]. Thereby the fluid motion is prescribed by the incompressible Navier–Stokes equations using an Eulerian coordinate system. By contrast the material elasticity equations related to the deformable object inside the fluid and its change of total elastic energy is written in a Lagrangian coordinate system. A third equation couples the afore-mentioned Eulerian and Lagrangian quantities. This method was successfully applied to the motion of red blood cells in microfluidic flows [FHL$^+$11]. However, the IB method has not been developed for rigid body motion. A comparison between the IB and FDLM method for particle motion inside quadrupolar vorticity patterns is given by [Hac14]. For detailed historical information and comparison to other methods of direct simulations, i.e. front tracking methods, and methods based on moving unstructured grids, such as arbitrary Lagrangian–Eulerian moving mesh techniques, we refer to [GPHJ99].

The fluid/particle interaction problem is formulated on the previously defined two-dimensional domain

$$\Gamma_s := [-\frac{l_X}{2}, +\frac{l_X}{2}] \times [-\frac{l_Y}{2}, +\frac{l_Y}{2}] \times \{l_Z\}, \tag{9.17}$$

where l_X and l_Y denote the length of the domain in X- and Y-direction. This domain represents the surface of the water in the experimental setting described in section 7.2. We neglect its possible curvature as described in section 8.2.

Let us apply the fictitious domain Lagrange multiplier method presented in [GPH$^+$01] as we suggested in [BFH$^+$15]. We consider $N \in \mathbb{N}$ rigid bodies, covering distinct subdomains $B_j(t) \subset \Gamma_s, 1 \leq j \leq N$, $t \in [0, T]$, where T denotes the end of the computational time, such that

$$B_j(t) \cap B_k(t) = \emptyset, \qquad 1 \leq j \neq k \leq N. \tag{9.18}$$

The motion within the fluid-filled domain Γ_s of each particle is described by the Newton–Euler equations. The motion of the j-th particle, $1 \leq j \leq N$, is described by its density ρ_j, mass M_j, center of mass c_j, velocity $\boldsymbol{v}_j$, angle Θ_j, angular velocity $\boldsymbol{\omega}_j$, and the inertia tensor $\boldsymbol{I}_j$, hydrodynamic force $\boldsymbol{F}_j^H$,

repulsive forces $\boldsymbol{F}_j^R$, and the resulting torque $\boldsymbol{T}_j^H$ of the hydrodynamic forces acting on it. Then the Newton–Euler equations determining the motion of the j-th particle, $1 \leq j \leq N$, read as follows

$$M_j \frac{\mathrm{d}\boldsymbol{v}_j}{\mathrm{d}t} = \boldsymbol{F}_j^H + \boldsymbol{F}_j^R, \quad \frac{\mathrm{d}c_j}{\mathrm{d}t} = \boldsymbol{v}_j(t), \quad \frac{\mathrm{d}\Theta_j}{\mathrm{d}t} = \frac{\mathrm{d}\boldsymbol{\omega}_j}{\mathrm{d}t}, \tag{9.19}$$

$$\boldsymbol{I}_j \frac{\mathrm{d}\boldsymbol{\omega}_j}{\mathrm{d}t} = \boldsymbol{T}_j^H + \overrightarrow{c_j x} \times \boldsymbol{F}_j^R, \tag{9.20}$$

with initial conditions

$$\boldsymbol{v}_j(0) = \boldsymbol{v}_j^0, \quad \boldsymbol{\omega}_j(0) = \boldsymbol{\omega}_j^0, \quad c_j(0) = c_j^0. \tag{9.21}$$

We have to note, that in the original work from [GPH+01], an artificial repulsive force is defined which guarantees smooth repulsion of spherically shaped objects. However, this does not cover real life problems where hard collision in water of arbitrarily shaped particles take place. As a first step, we improved the particle-particle and particle-boundary repulsion model which allows arbitrary shaped particles as described below. For this purpose P^j and $P^{\partial\Gamma_s}$ denote the sets of repulsion points $p_i \in P_j$ belonging to the j-th particle and the domain boundary. The repulsion points are uniformly distributed over the boundary of the particle with special respect to the reentrant and salient corners, rising out of the regular shape. In our case, the combined repulsive force $\boldsymbol{F}_j^R(p_i)$ acting on the repulsion point p_i of the j-th particle, $1 \leq j \leq N$, is given by

$$\boldsymbol{F}_j^R(p_i) = \boldsymbol{F}_j^{\partial\Gamma_s}(p_i) + \sum_{k \neq j} \boldsymbol{F}_j^{P_k}(p_i), \tag{9.22}$$

where $\boldsymbol{F}_j^{P_k}$ is the repulsive force between the j-th particle and the k-th particle and $\boldsymbol{F}_j^{\partial\Gamma_s}$ is the repulsive force between the j-th particle and the boundary $\partial\Gamma_s$ defined by

$$\boldsymbol{F}_j^{\partial\Gamma_s}(p_i) := \sum_{p_l \in P^{\partial\Gamma_s}} \boldsymbol{F}^R(p_i, p_l), \tag{9.23}$$

$$\boldsymbol{F}_j^{P_k}(p_i) := \sum_{p_l \in P_k} \boldsymbol{F}^R(p_i, p_l). \tag{9.24}$$

The basic repulsive force $\boldsymbol{F}^R$ is given by

$$\boldsymbol{F}^R(p_i, p_l) := \begin{cases} 0, & \|p_i - p_l\| \geq r, \\ \varepsilon^{-1}(p_i - p_l)/\|p_i - p_l\|, & \|p_i - p_l\| < r. \end{cases} \tag{9.25}$$

We use the scaling factor ε and the repulsion length $r > 0$. The repulsion length r is defined with respect to the finite element discretization of our domain Γ_s described in section 9.3. A practical value is one half of the uniform

mesh width. Based on the presented implementation, further improvements have been suggested in the master thesis [Hac14].

In chapter 8 we discussed the nature of the compressible effects of the surface acoustic waves acting at short time scales of nanoseconds (10^{-9} s). By contrast, the particles propagate at time scales of seconds where the compressible effects of the surface acoustic waves can be neglected. In addition to this the particles show steady flow allowing the fluid to relax at this time scale. Consequently, the fluid inside the time-dependent domain $\Gamma_s(t) := \Gamma_s \backslash \bigcup_{j=1}^{N} \overline{B_j(t)}$, $t \in (0,T)$, is modeled by the incompressible Navier–Stokes equations such that for a given fluid density ρ_f, dynamic viscosity η, stress tensor $\boldsymbol{\sigma}$, force field $\boldsymbol{f}_s$, and initial velocity field $\boldsymbol{v}_s$ there holds

$$\rho_f\Big(\frac{\partial \boldsymbol{v}}{\partial t} + (\boldsymbol{v}\cdot\nabla)\boldsymbol{v}\Big) - \nabla\cdot\boldsymbol{\sigma}(\boldsymbol{v}) = \boldsymbol{f}_s \quad \text{in } \Gamma_s(t), \tag{9.26}$$

$$\nabla\cdot\boldsymbol{v} = 0 \quad \text{in } \Gamma_s(t), \tag{9.27}$$

with boundary conditions

$$\boldsymbol{v}(x,t) = \begin{cases} \boldsymbol{v}_s(x) & , \quad x \in \partial\Gamma_s(t), \\ \boldsymbol{v}_j(t) + \boldsymbol{\omega}_j(t) \times \overrightarrow{c_j(t)x} & , \quad x \in \partial B_j(t), \end{cases} \tag{9.28}$$

and initial condition

$$\boldsymbol{v}(x,0) = \boldsymbol{v}_s(x), \quad x \in \Gamma_s(0). \tag{9.29}$$

where the expression $\overrightarrow{c_j(t)x}$ in (9.28) denotes the vector joining $c_j(t)$ and x. The subscripts of the initial velocity field $\boldsymbol{v}_s$ and the force field $\boldsymbol{f}_s$ are motivated by the relation

$$(\boldsymbol{v}_s\cdot\nabla)\boldsymbol{v}_s - \nabla\cdot\boldsymbol{\sigma}(\boldsymbol{v}_s) = \boldsymbol{f}_s. \tag{9.30}$$

This means the force field $\boldsymbol{f}_s$ is derived from a given stationary velocity field $\boldsymbol{v}_s$. Thus, it makes perfect sense that the initial and boundary conditions are defined with respect to the stationary velocity field. A concrete example using the quadupolar force density suggested by [KSTH06] is given in subsection 9.4.2 .

Now, we introduce a combined weak formulation of fluid and particle motion using distributed Lagrange multipliers $\boldsymbol{\lambda}_j(t) \in \boldsymbol{\Lambda}_j(t)$, with

$$\boldsymbol{\Lambda}_j(t) := \boldsymbol{H}^1(B_j(t)), \quad 1 \le j \le N. \tag{9.31}$$

The FDLM method is then to find $\boldsymbol{v}(t) \in \boldsymbol{V}$,

$$\boldsymbol{V} := \{\boldsymbol{H}^1(\Gamma_s) \mid \boldsymbol{v}|_{\partial\Gamma_s} = \boldsymbol{v}_s\}, \tag{9.32}$$

$p(t) \in L^2_0(\Gamma_s)$, $\boldsymbol{v}_j(t), c_j(t) \in \mathbb{R}^2$, $\boldsymbol{\omega}_j(t) \in \mathbb{R}$, $\boldsymbol{\lambda}_j(t) \in \boldsymbol{\Lambda}_j(t)$, $1 \le j \le N$, such that for all $\boldsymbol{w} \in \boldsymbol{H}^1_0(\Gamma_s)$, $q \in L^2_0(\Gamma_s)$, $\boldsymbol{Y} \in \mathbb{R}^2$, $\boldsymbol{\tau} \in \mathbb{R}$, $\boldsymbol{\mu}_j \in \boldsymbol{\Lambda}_j(t)$, $1 \le j \le N$, there holds

$$
\begin{aligned}
&\rho_f \int_{\Gamma_s} \Big(\frac{\partial \boldsymbol{v}}{\partial t} + (\boldsymbol{v} \cdot \nabla)\boldsymbol{v} \Big) \cdot \boldsymbol{w} \, \mathrm{d}x - \int_{\Gamma_s} p \nabla \cdot \boldsymbol{w} \, \mathrm{d}x \\
&+\eta \int_{\Gamma_s} \nabla \boldsymbol{v} : \nabla \boldsymbol{w} \, \mathrm{d}x + \sum_{j=1}^{N} (1 - \frac{\rho_f}{\rho_j}) \Big(M_j \frac{\mathrm{d}\boldsymbol{v}_j}{\mathrm{d}t} \cdot \boldsymbol{Y} + \boldsymbol{I}_j \frac{\mathrm{d}\boldsymbol{\omega}_j}{\mathrm{d}t} \cdot \boldsymbol{\tau} \Big) \\
&= \sum_{j=1}^{N} \int_{B_j(t)} \boldsymbol{\lambda}_j \cdot (\boldsymbol{w} - \boldsymbol{Y} - \boldsymbol{\tau} \times \overrightarrow{c_j x}) \, \mathrm{d}x + \int_{\Gamma_s} \boldsymbol{f} \cdot \boldsymbol{w} \, \mathrm{d}x \\
&+ \sum_{j=1}^{N} \Big(\sum_{p_i \in P_j} \boldsymbol{F}^R_j(p_i) \cdot \boldsymbol{Y} + \sum_{p_i \in P_j} (\overrightarrow{c_j p_i} \times \boldsymbol{F}^R_j(p_i)) \cdot \boldsymbol{\tau} \Big),
\end{aligned}
\tag{9.33}
$$

$$
\int_{\Gamma_s} q \nabla \cdot \boldsymbol{v} \, \mathrm{d}x = 0, \tag{9.34}
$$

$$
\int_{B_j(t)} \Big(\boldsymbol{\mu}_j \cdot (\boldsymbol{v} - \boldsymbol{v}_j - \boldsymbol{\omega}_j \times \overrightarrow{c_j x}) \Big) \, \mathrm{d}x = 0, \tag{9.35}
$$

for a.e. t with initial conditions

$$
\boldsymbol{v}(x,0) = \begin{cases} \boldsymbol{v}_s, & x \in \Gamma_s(0) \setminus \overline{B_j(0)}, \\ \boldsymbol{v}_j^0 + \boldsymbol{\omega}_j^0 \times \overrightarrow{c_j^0 x}, & x \in \overline{B_j(0)}, \end{cases} \tag{9.36}
$$

$$
\boldsymbol{v}_j(0) = \boldsymbol{v}_j^0, \qquad c_j(0) = c_j^0, \qquad \boldsymbol{\omega}_j(0) = \boldsymbol{\omega}_j^0. \tag{9.37}
$$

Despite the scalar nature of the angular velocity $\boldsymbol{\omega}_j(t) \in \mathbb{R}$ we use bold notation due to its vectorial roots. The term $\boldsymbol{\omega}_j \times \overrightarrow{c_j x}$ in equation (9.35) is well defined in $\mathbb{R}^3$. For this purpose $\boldsymbol{\omega}_j$ and $\overrightarrow{c_j x}$ are appropriately extended by zero components such that

$$
\boldsymbol{\omega}_j \times \overrightarrow{c_j x} = \begin{pmatrix} 0 \\ 0 \\ \boldsymbol{\omega}_j \end{pmatrix} \times \begin{pmatrix} (\overrightarrow{c_j x})_1 \\ (\overrightarrow{c_j x})_2 \\ 0 \end{pmatrix} = \begin{pmatrix} -\boldsymbol{\omega}_j (\overrightarrow{c_j x})_2 \\ \boldsymbol{\omega}_j (\overrightarrow{c_j x})_1 \\ 0 \end{pmatrix}, \tag{9.38}
$$

where we used $\overrightarrow{c_j x} := \big((\overrightarrow{c_j x})_1, (\overrightarrow{c_j x})_2 \big)^T$.

Finally we motivate the presented combined weak formulation of the FDLM method from a physical point of view. The extension of the fluid domain $\Gamma_s(t) := \Gamma_s \setminus \bigcup_{j=1}^{N} \overline{B_j(t)}$, $t \in (0,T)$, can be interpreted as filling the particle domains with fluid. In doing so the rigid body motion in the particle domains and the no-slip particle boundary conditions are imposed using distributed Lagrange multipliers.

9.3 Numerical Methods

Following [GPH+01] and [BFH+15], we discretize the FDLM method (9.33) – (9.37) in space and time. In order to do so, we introduce a uniform simplicial triangulation $\mathcal{T}_h(\Gamma_s)$ of Γ_s. The incompressible Navier–Stokes equations are discretized using standard Taylor–Hood P2/P1 elements [BF91]. For implementations using adaptive grids at particle boundaries we refer to [Hac14]. Next, the finite element spaces $\boldsymbol{V}_h$ for the velocity and Q_h for the pressure are given by

$$\boldsymbol{V}_h := \{\boldsymbol{v}_h \in \boldsymbol{C}(\bar{\Gamma}_s) \mid \boldsymbol{v}_h|_K \in P_2(K)^2, K \in \mathcal{T}_h(\Gamma_s), \boldsymbol{v}_h|_{\partial\Gamma_s} = \boldsymbol{v}_{s,h}\}, \tag{9.39}$$

$$Q_h := \{q_h \in C(\bar{\Gamma}_s) \mid q_h|_K \in P_1(K), K \in \mathcal{T}_h(\Gamma_s), \int_{\Gamma_s} q_h \, \mathrm{d}x = 0\}, \tag{9.40}$$

where $P_k(K), k \in \mathbb{N}$, denotes the set of polynomials of degree less or equal k for elements $K \in \mathcal{T}_h(\Gamma_s)$ and $\boldsymbol{v}_{s,h}$ denotes the $\boldsymbol{L}^2$-projection of the initial velocity $\boldsymbol{v}_s$ onto the space of piecewise polynomials of degree 2 on $\partial\Gamma_s$. The velocity test space $\boldsymbol{V}_{0,h}$ is further defined by

$$\boldsymbol{V}_{0,h} := \{\boldsymbol{v}_h \in \boldsymbol{C}(\bar{\Gamma}_s) \mid \boldsymbol{v}_h|_K \in P_2(K)^2, K \in \mathcal{T}_h(\Gamma_s), \boldsymbol{v}_h|_{\partial\Gamma_s} = \boldsymbol{0}\}. \tag{9.41}$$

We already mentioned that there is no need to define triangulations $\mathcal{T}_h(B_j(t))$ of the domains occupied by the particles, $1 \leq j \leq N$. Instead we define the finite element spaces $\boldsymbol{\Lambda}_{j,h}(t)$ for the distributed Lagrange multiplier of the j-th particle based on the existing triangulation $\mathcal{T}_h(\Gamma_s)$, such that

$$\boldsymbol{\Lambda}_{j,h}(t) := \{\boldsymbol{\lambda}_h \in \boldsymbol{C}(B_{j,h}(t)) \mid \boldsymbol{\lambda}_h|_K \in P_2(K)^2, K \in B_{j,h}(t)\}, \tag{9.42}$$

for $1 \leq j \leq N$, where the discrete particle domain $B_{j,h}(t)$ is defined by

$$B_{j,h}(t) := \{K \in \mathcal{T}_h(\Gamma_s) \mid K \subset B_j(t)\}. \tag{9.43}$$

Then the discretized version in space of the FDLM method (9.33) – (9.37) is to find $\boldsymbol{v}_h(t) \in \boldsymbol{V}_h$, $p_h(t) \in Q_h$, $\boldsymbol{v}_j(t) \in \mathbb{R}^2$, $c_j(t) \in \mathbb{R}^2$, $\boldsymbol{\omega}_j(t) \in \mathbb{R}$, $\boldsymbol{\lambda}_{j,h}(t) \in \boldsymbol{\Lambda}_{j,h}(t)$, such that for all $\boldsymbol{w}_h \in \boldsymbol{V}_{0,h}$, $q_h \in Q_h$, $\boldsymbol{Y} \in \mathbb{R}^2$, $\tau \in \mathbb{R}$, $\boldsymbol{\mu}_{j,h} \in \boldsymbol{\Lambda}_{j,h}(t)$, there holds

$$\begin{aligned}
&\rho_f \int_{\Gamma_s} \Big(\frac{\partial \boldsymbol{v}_h}{\partial t} + (\boldsymbol{v}_h \cdot \nabla)\boldsymbol{v}_h\Big) \cdot \boldsymbol{w}_h \, \mathrm{d}x - \int_{\Gamma_s} p \nabla \cdot \boldsymbol{w}_h \, \mathrm{d}x \\
&+\eta \int_{\Gamma_s} \nabla \boldsymbol{v}_h : \nabla \boldsymbol{w}_h \, \mathrm{d}x + \sum_{j=1}^{N} (1 - \frac{\rho_f}{\rho_j}) \Big(M_j \frac{d\boldsymbol{v}_j}{dt} \cdot \boldsymbol{Y} + \boldsymbol{I}_j \frac{d\boldsymbol{\omega}_{j,h}}{dt} \cdot \boldsymbol{\tau}\Big) \\
&= \sum_{j=1}^{N} \int_{B_{j,h}(t)} \boldsymbol{\lambda}_{h,j} \cdot (\boldsymbol{w}_h - \boldsymbol{Y} - \boldsymbol{\tau} \times \overrightarrow{c_j x}) \, \mathrm{d}x + \int_{\Gamma_s} \boldsymbol{f} \cdot \boldsymbol{w}_h \, \mathrm{d}x \\
&\quad + \sum_{j=1}^{N} \Big(\sum_{p_i \in P_j} \boldsymbol{F}_j^R(p_i) \cdot \boldsymbol{Y} + \sum_{p_i \in P_j} (\overrightarrow{c_j p_i} \times \boldsymbol{F}_j^R(p_i)) \cdot \boldsymbol{\tau} \Big),
\end{aligned} \tag{9.44}$$

$$\int_{\Gamma_s} q_h \nabla \cdot \boldsymbol{v}_h \, \mathrm{d}x = 0, \tag{9.45}$$

$$\int_{B_{j,h}(t)} \left(\boldsymbol{\mu}_{j,h} \cdot (\boldsymbol{v}_h - \boldsymbol{v}_j - \boldsymbol{\omega}_j \times \overrightarrow{c_j x}) \right) \mathrm{d}x = 0, \tag{9.46}$$

for a.e. t and $1 \leq j \leq N$, with initial conditions

$$\boldsymbol{v}_h(x,0) = \begin{cases} \boldsymbol{v}_{s,h}, & x \in \Gamma_s(0) \setminus \overline{B_{j,h}(0)}, \\ \boldsymbol{v}_j^0 + \boldsymbol{\omega}_j^0 \times \overrightarrow{c_j^0 x}, & x \in \overline{B_{j,h}(0)}, \end{cases} \tag{9.47}$$

$$\boldsymbol{v}_j(0) = \boldsymbol{v}_j^0, \quad c_j(0) = c_j^0, \quad \boldsymbol{\omega}_j(0) = \boldsymbol{\omega}_j^0, \tag{9.48}$$

where $\boldsymbol{v}_{s,h}$ denotes the $\boldsymbol{L}^2$-projection of the initial velocity $\boldsymbol{v}_s$ onto $\boldsymbol{V}_h$. We remark that in the discretized version we distinguish between the actual particle domain $B_j(t)$ which is updated at every time step, and the mesh dependent particle domain $B_{j,h}(t)$ which is derived from $B_j(t)$ according to the definition (9.43).

The temporal discretization is performed by a Yanenko–Marchuk fractional step method [Mar90] as suggested in [GPH+01]. This way we get a series of different subproblems which can be solved separately. Let us introduce the uniform discretization of the time interval $[0,T]$ using the time step size $\Delta t := T/N_T$, $N_T \in \mathbb{N}$, and denote for example by $\boldsymbol{v}^n$ an approximation of $\boldsymbol{v}$ at time t_n, with $t_n := n\Delta t$, $n \in \mathbb{N}$, $0 \leq n \leq N_T$.

When we proceed in time from t_{n-1} to t_n we begin solving the fluid motion of the discretized FDLM method (9.44) – (9.48). For this purpose, we use the splitting method proposed by Chorin and Temam [Cho97, Tem68]. This is done by computing an auxiliary velocity $\tilde{\boldsymbol{v}}_h \in \boldsymbol{V}_h$ such that for all $\boldsymbol{w}_h \in \boldsymbol{V}_{0,h}$ there holds

$$\begin{aligned} \rho_f \int_{\Gamma_s} \frac{\tilde{\boldsymbol{v}}_h - \boldsymbol{v}_h^{n-1}}{\Delta t_n} \cdot \boldsymbol{w}_h \, \mathrm{d}x + \rho_f \int_{\Gamma_s} (\nabla \boldsymbol{v}_h^{n-1} \cdot \boldsymbol{v}_h^{n-1}) \boldsymbol{w}_h \, \mathrm{d}x \\ + \eta \int_{\Gamma_s} \nabla \boldsymbol{v}_h^{n-1} \cdot \nabla \boldsymbol{w}_h \, \mathrm{d}x = \int_{\Gamma_s} \boldsymbol{f} \cdot \boldsymbol{w}_h \, \mathrm{d}x. \end{aligned} \tag{9.49}$$

In order to get an intermediate solution $\boldsymbol{v}_h^{n-1/2} \in \boldsymbol{V}_h$ and pressure $p_h^n \in Q_h$, we finalize this step by projecting the previously computed velocity $\tilde{\boldsymbol{v}}_h$ onto the space of divergence free vector fields by solving the equations

$$\Delta t \int_{\Gamma_s} \nabla p_h^n \cdot \nabla q_h \, \mathrm{d}x = -\int_{\Gamma_s} (\nabla \cdot \tilde{\boldsymbol{v}} \; q_h), \tag{9.50}$$

$$\int_{\Gamma_s} \boldsymbol{v}_h^{n-1/2} \boldsymbol{w}_h \, \mathrm{d}x = \int_{\Gamma_s} \tilde{\boldsymbol{v}}_h \cdot \boldsymbol{w}_h \, \mathrm{d}x - \Delta t \int_{\Gamma_s} \nabla p_h^n \cdot \boldsymbol{w}_h \, \mathrm{d}x, \tag{9.51}$$

for all $\boldsymbol{w}_h \in \boldsymbol{V}_{0,h}$ and $q_h \in Q_h$.

As the second step of the Yanenko–Marchuk fractional step method, we solve the fluid–particle interaction subproblem of the discretized FDLM method (9.44) – (9.48) which is finding $\boldsymbol{v}_h(t) \in \boldsymbol{V}_h$, $\boldsymbol{v}_j(t) \in \mathbb{R}^2$, $\boldsymbol{\omega}_j(t) \in \mathbb{R}$, $\boldsymbol{\lambda}_{j,h}(t) \in \boldsymbol{\Lambda}_{j,h}(t)$ such that for all $\boldsymbol{w}_h \in \boldsymbol{V}_{0,h}$, $\boldsymbol{Y} \in \mathbb{R}^2$, $\boldsymbol{\tau} \in \mathbb{R}$, $\boldsymbol{\mu}_{j,h} \in \boldsymbol{\Lambda}_{j,h}(t)$ there holds

$$\begin{aligned} \rho_f \int\limits_{\Gamma_s} \frac{\partial \boldsymbol{v}_h}{\partial t}\ \mathrm{d}x + \sum_{j=1}^{N} (1 - \frac{\rho_f}{\rho_j}) \Big(M_j \frac{\mathrm{d}\boldsymbol{v}_j}{\mathrm{d}t} \cdot \boldsymbol{Y} + \boldsymbol{I}_j \frac{\mathrm{d}\boldsymbol{\omega}_j}{\mathrm{d}t} \cdot \boldsymbol{\tau} \Big) = \\ = \sum_{j=1}^{N} \int\limits_{B_{j,h}(t)} \boldsymbol{\lambda}_{j,h} \cdot (\boldsymbol{w}_h - \boldsymbol{Y} - \boldsymbol{\tau} \times \overrightarrow{c_j x})\ \mathrm{d}x, \end{aligned} \tag{9.52}$$

$$\int\limits_{B_{j,h}(t)} \boldsymbol{\mu_{j,h}} \cdot (\boldsymbol{v}_h - \boldsymbol{v}_j - \boldsymbol{\omega}_j \times \overrightarrow{c_j x})\ \mathrm{d}x = 0, \tag{9.53}$$

for a.e. $t \in [t_{n-1}, t_n]$ and $1 \le j \le N$. This task is performed using a conjugate gradient algorithm proposed in [GPH+01], where subscripts in brackets refer to the conjugate gradient step. The initial step $k = 0$ is finding the initial variables $\boldsymbol{v}_h^{(0)} \in \boldsymbol{V}_h$, $\boldsymbol{v}_j^{(0)} \in \mathbb{R}^2$, $\boldsymbol{\omega}_j^{(0)} \in \mathbb{R}$, $1 \le j \le N$, for given initial Lagrangians $\boldsymbol{\lambda}_{h,j}^{(0)} \in \boldsymbol{\Lambda}_{j,h}^{n-1}$, such that for all $\boldsymbol{w}_h \in \boldsymbol{V}_{0,h}$, $\boldsymbol{Y} \in \mathbb{R}^2$, $\boldsymbol{\tau} \in \mathbb{R}$ there holds

$$\rho_f \int\limits_{\Gamma_s} \frac{\boldsymbol{v}_h^{(0)} - \boldsymbol{v}_h^{n-1/2}}{\Delta t} \cdot \boldsymbol{w}_h\ \mathrm{d}x = \sum_{j=1}^{N} \int\limits_{B_{j,h}^{n-1}} \boldsymbol{\lambda}_{j,h}^{(0)} \cdot \boldsymbol{w}_h\ \mathrm{d}x, \tag{9.54}$$

$$(1 - \frac{\rho_f}{\rho_j}) M_j \frac{\boldsymbol{v}_j^{(0)} - \boldsymbol{v}_j^{n-1}}{\Delta t} \cdot \boldsymbol{Y} = - \int\limits_{B_{j,h}^{n-1}} \boldsymbol{\lambda}_{j,h}^{(0)} \cdot \boldsymbol{Y}\ \mathrm{d}x, \tag{9.55}$$

$$(1 - \frac{\rho_f}{\rho_j}) \boldsymbol{I}_j \frac{\boldsymbol{\omega}_j^{(0)} - \boldsymbol{\omega}_j^{n-1}}{\Delta t} \cdot \boldsymbol{\tau} = - \int\limits_{B_{j,h}^{n-1}} \boldsymbol{\lambda}_{j,h}^{(0)} \cdot \boldsymbol{\tau} \times \overrightarrow{c_j^{n-1} x}\ \mathrm{d}x, \tag{9.56}$$

and we further compute the initial variables $\boldsymbol{g}_{j,h}^{(0)} \in \boldsymbol{\Lambda}_{j,h}^{n-1}$, $1 \le j \le N$, such that for all $\boldsymbol{\mu}_{j,h} \in \boldsymbol{\Lambda}_{j,h}^{n-1}$ there holds

$$\int\limits_{B_{j,h}^{n-1}} \boldsymbol{\mu}_{j,h} \cdot \boldsymbol{g}_{j,h}^{(0)}\ \mathrm{d}x = \int\limits_{B_{j,h}^{n-1}} \boldsymbol{\mu}_{j,h} \cdot (\boldsymbol{v}_h^{(0)} - \boldsymbol{v}_j^{(0)} - \boldsymbol{\omega}_j^{(0)} \times \overrightarrow{c_j^{n-1} x})\ \mathrm{d}x, \tag{9.57}$$

and we finally set $\boldsymbol{z}_{j,h}^{(0)} = \boldsymbol{g}_{j,h}^{(0)}$. Now, the step $k - 1 \to k$, $k \in \mathbb{N}$, $k \ge 1$, is given by the computation of the auxiliary descent variables $\boldsymbol{v}_h^d \in \boldsymbol{V}_h$,

$\boldsymbol{v}_j^d \in \mathbb{R}^2$, $\boldsymbol{\omega}_j^d \in \mathbb{R}$, $1 \le j \le N$, such that for all $\boldsymbol{w}_h \in \boldsymbol{V}_{0,h}$, $\boldsymbol{Y} \in \mathbb{R}^2$, $\boldsymbol{\tau} \in \mathbb{R}$ there holds

$$\rho_f \int_{\Gamma_s} \frac{\boldsymbol{v}_h^d}{\Delta t} \cdot \boldsymbol{w}_h \, \mathrm{d}x = \sum_{j=1}^{N} \int_{B_{j,h}^{n-1}} \boldsymbol{z}_{j,h}^{(k-1)} \cdot \boldsymbol{w}_h \, \mathrm{d}x, \tag{9.58}$$

$$(1 - \frac{\rho_f}{\rho_j}) M_j \frac{\boldsymbol{v}_j^d}{\Delta t} \cdot \boldsymbol{Y} = - \int_{B_{j,h}^{n-1}} \boldsymbol{z}_{j,h}^{(k-1)} \cdot \boldsymbol{Y} \, \mathrm{d}x, \tag{9.59}$$

$$(1 - \frac{\rho_f}{\rho_j}) \boldsymbol{I}_j \frac{\boldsymbol{\omega}_j^d}{\Delta t} \cdot \boldsymbol{\tau} = - \int_{B_{j,h}^{n-1}} \boldsymbol{z}_{j,h}^{(k-1)} \cdot \boldsymbol{\tau} \times \overrightarrow{c_j^{n-1} x} \, \mathrm{d}x, \tag{9.60}$$

and we further compute the auxiliary descent variables $\boldsymbol{g}_{j,h}^d \in \boldsymbol{\Lambda}_{j,h}^{n-1}$, $1 \le j \le N$, such that for all $\boldsymbol{\mu}_{j,h} \in \boldsymbol{\Lambda}_{j,h}^{n-1}$ there holds

$$\int_{B_{j,h}^{n-1}} \boldsymbol{\mu}_{j,h} \cdot \boldsymbol{g}_{j,h}^d \, \mathrm{d}x = \int_{B_{j,h}^{n-1}} \boldsymbol{\mu}_{j,h} \cdot (\boldsymbol{v}_h^d - \boldsymbol{v}_j^d - \boldsymbol{\omega}_j^d \times \overrightarrow{c_j^{n-1} x}) \, \mathrm{d}x. \tag{9.61}$$

For $1 \le j \le N$, we compute the steplengths

$$\rho_j^{(k-1)} = \frac{\int_{B_{j,h}^{n-1}} \boldsymbol{g}_{j,h}^{(k-1)} \cdot \boldsymbol{g}_{j,h}^{(k-1)} \, \mathrm{d}x}{\int_{B_{j,h}^{n-1}} \boldsymbol{z}_{j,h}^{(k-1)} \cdot (\boldsymbol{v}_h^d - \boldsymbol{v}_j^d - \boldsymbol{\omega}_j^d \times \overrightarrow{c_j^{n-1} x}) \, \mathrm{d}x} \tag{9.62}$$

which are used to get the updated variables

$$\boldsymbol{\lambda}_{j,h}^{(k)} = \boldsymbol{\lambda}_{j,h}^{(k-1)} - \rho_j^{(k-1)} \boldsymbol{z}_{j,h}^{(k-1)}, \tag{9.63}$$

$$\boldsymbol{v}_h^{(k)} = \boldsymbol{v}_h^{(k-1)} - \rho_j^{(k-1)} \boldsymbol{v}_h^d, \tag{9.64}$$

$$\boldsymbol{v}_j^{(k)} = \boldsymbol{v}_j^{(k-1)} - \rho_j^{(k-1)} \boldsymbol{v}_j^d, \tag{9.65}$$

$$\boldsymbol{\omega}_j^{(k)} = \boldsymbol{\omega}_j^{(k-1)} - \rho_j^{(k-1)} \boldsymbol{\omega}_j^d, \tag{9.66}$$

$$\boldsymbol{g}_{j,h}^{(k)} = \boldsymbol{g}_{j,h}^{(k-1)} - \rho_j^{(k-1)} \boldsymbol{g}_{j,h}^d, \tag{9.67}$$

$$\boldsymbol{z}_{j,h}^{(k)} = \boldsymbol{g}_j^{(k-1)} - \gamma_j^{(k-1)} \boldsymbol{z}_{j,h}^{(k-1)}, \tag{9.68}$$

with

$$\gamma_j^{(k-1)} = \frac{\int_{B_{j,h}^{n-1}} \boldsymbol{g}_{j,h}^{(k)}, \boldsymbol{g}_{j,h}^{(k)} \, \mathrm{d}x}{\int_{B_{j,h}^{n-1}} \boldsymbol{g}_{j,h}^{(k-1)}, \boldsymbol{g}_{j,h}^{(k-1)} \, \mathrm{d}x}. \tag{9.69}$$

Now, if for a given tolerance $\epsilon_{\text{tol}} \in \mathbb{R}$, $\epsilon_{\text{tol}} > 0$, there holds

$$\frac{\int\limits_{B_{j,h}^{n-1}} \boldsymbol{g}_{j,h}^{(k)}, \boldsymbol{g}_{j,h}^{(k)} \, \mathrm{d}x}{\int\limits_{B_{j,h}^{n-1}} \boldsymbol{g}_{j,h}^{d}, \boldsymbol{g}_{j,h}^{d} \, \mathrm{d}x} \leq \epsilon_{\text{tol}}, \quad 1 \leq j \leq N, \tag{9.70}$$

we stop the conjugate gradient algorithm and set for $1 \leq j \leq N$

$$\boldsymbol{\lambda}_{j,h}^{n} = \boldsymbol{\lambda}_{j,h}^{(k)}, \tag{9.71}$$

$$\boldsymbol{v}_{h}^{n} = \boldsymbol{v}_{h}^{(k)}, \tag{9.72}$$

$$\boldsymbol{v}_{j}^{n-1/2} = \boldsymbol{v}_{j}^{(k)}, \tag{9.73}$$

$$\boldsymbol{\omega}_{j}^{n-1/2} = \boldsymbol{\omega}_{j}^{(k)}. \tag{9.74}$$

Otherwise, we proceed with $k \to k+1$.

The third and last step of the Yanenko-Marchuk fractional step method to proceed in time from t_{n-1} to t_n is updating the remaining particle properties such that for $1 \leq j \leq N$

$$c_j^n = c_j^{n-1} + \Delta t \; \boldsymbol{v}_j^n, \tag{9.75}$$

$$\Theta_j^n = \Theta_j^{n-1} + \Delta t \; \boldsymbol{\omega}_j^n, \tag{9.76}$$

$$\boldsymbol{v}_j^n = \boldsymbol{v}_j^{n-1/2} + \Delta t \; M_j^{-1} \sum_{p_i \in P_j} \boldsymbol{F}_j^R(p_i), \tag{9.77}$$

$$\boldsymbol{\omega}_j^n = \boldsymbol{\omega}_j^{n-1/2} + \Delta t \; \boldsymbol{I}_j^{-1} \sum_{p_i \in P_j} (\overrightarrow{c_j p_i} \times \boldsymbol{F}_j^R(p_i)). \tag{9.78}$$

9.4 Simulation Results

9.4.1 Implementation Issues

We implemented the discretized FDLM method presented in the previous section 9.3 using the programming language *Python* [vRdB91] and different libraries, particularly the mathematical libraries *NumPy* and *SciPy* [Oli07], the finite element library *FEniCS* [LMWea12], and the plotting library *matplotlib* [Hun07].

In simulation, we use the square domain $\Gamma_s \subset \mathbb{R}^2$ defined by

$$\Gamma_s := (-\frac{l_{\Gamma_s}}{2}, +\frac{l_{\Gamma_s}}{2})^2, \tag{9.79}$$

for a given length l_{Γ_s}. This domain is further discretized by the uniform, simplicial triangulation $\mathcal{T}_h(\Gamma_s)$ with grid size h. Relevant parameters for a set of implemented particles are described in Figure 9.2. These parameters

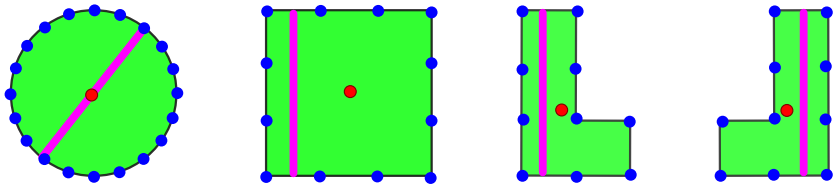

Figure 9.2: Definition of length (magenta), center of mass (red), and repulsion points (blue) for a set of particles showing zero angle of rotation.

are further used to specify the subsequent simulation together with the fluid and particle constants contained in the FDLM method (9.33) – (9.37).

For the set of parameters the method proved to be stable and we did not introduce a dimensionless formulation. However, for particle densities close to the fluid density, the presented conjugate gradient algorithm tends to diverge before the given tolerance ϵ_{tol} is reached.

9.4.2 Quadrupolar Force Density

Here, we present simulation results from [BFL$^+$13], showing enantiomer separation using quadrupolar force densities. From a theoretical point of view, enantiomer separation has been predicted for particles of simplicial shape in [KSTH06] using a quadrupolar vorticity pattern. This pattern consists of pairwise counter-rotating vortices, such that for $x = (x_1, x_2) \in \Gamma_s$ the velocity $\boldsymbol{v}_Q$ is defined by

$$\boldsymbol{v}_Q(x) := \Big(\frac{\partial \boldsymbol{\psi}(x)}{\partial x_1}, -\frac{\partial \boldsymbol{\psi}(x)}{\partial x_2}\Big)^T, \tag{9.80}$$

with a stream function $\boldsymbol{\psi}(x_1, x_2)$ given by

$$\boldsymbol{\psi}(x_1, x_2) := v_{\max} \frac{l_{\Gamma_s}\sqrt{3}}{\pi} \frac{\sin(\pi x_1/l_{\Gamma_s})\sin(\pi x_2/l_{\Gamma_s})}{(2-\cos(\pi x_1/l_{\Gamma_s}))(2-\cos(\pi x_2/l_{\Gamma_s}))}, \tag{9.81}$$

where $v_{\max} \in \mathbb{R}$, $v_{\max} > 0$, denotes the maximum velocity. The corresponding right-hand side $\boldsymbol{f_Q}$ which is called quadrupolar force density, of the discretized FDLM method (9.44) – (9.48) is then given by

$$\begin{aligned} \int_{\Gamma_s} \boldsymbol{f}_Q \cdot \boldsymbol{w} \, \mathrm{d}x = \rho_f \int_{\Gamma_s} (\boldsymbol{v}_Q \cdot \nabla)\boldsymbol{v}_Q \cdot \boldsymbol{w} \, \mathrm{d}x \\ + \eta \int_{\Gamma_s} \nabla \boldsymbol{v}_Q : \nabla \boldsymbol{w} \, \mathrm{d}x, \qquad \boldsymbol{w}_h \in \boldsymbol{V}_{0,h}. \end{aligned} \tag{9.82}$$

Consequently, we set the initial and boundary velocity $\boldsymbol{v}_s = \boldsymbol{v}_Q$.

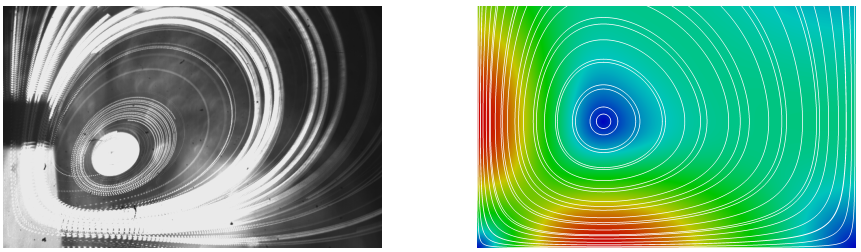

Figure 9.3: Experimental vorticity pattern (left) and quadrupolar vorticity pattern (right). [BFL$^+$13]

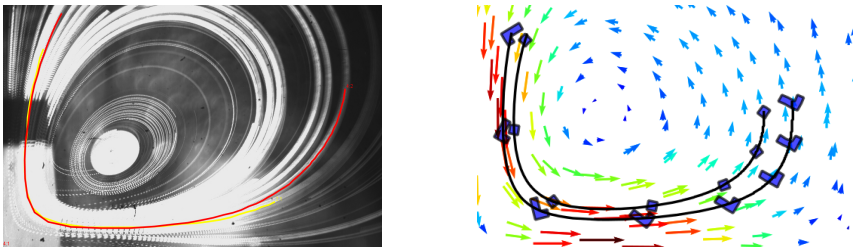

Figure 9.4: Experimental (left) and computational (right) trajectories. [BFL$^+$13]

The quadrupolar vorticity pattern qualitatively matches the vorticity patterns occurring in the experiments, as can be see in Figure 9.3. Nevertheless we have to adapt the size and the maximum velocity of the quadrupolar vorticity pattern to the experimental setup for validation. We therefore used the parameters and constants given in Table 9.1. Again the qualitative comparison of particle trajectories in simulation and experiments in figure 9.4 shows good agreement. In addition to this, we compared the angle of rotation of a given particle in experiment and simulation in a quantitative manner, and the resulting plot shows virtually perfect agreement as shown in Figure 9.5. Consequently, the quadrupolar vorticity pattern is a good approximation for the SAW-actuated vorticity pattern.

The question is now whether the theoretically predicted enantiomer separation is possible in experiment using SAW-actuated velocity fields. Experimental measurements indeed suggest the existence of such effects for L-shaped enantiomers [Kon08]. Once dropped onto the fluid surface, right-handed and left-handed L-shaped particles show trajectories leading to vortices rotating clockwise and counterclockwise. We performed simulations using the quadrupolar velocity field together with the parameters and constants given in Table 9.2 and found two characteristic phenomena of separation for L-shaped enantiomers which reflect the experiments regarding the sorting. In Figure 9.6 we see the separation at the end of the outgoing velocity stream for particles placed slightly next to the central incoming stream-

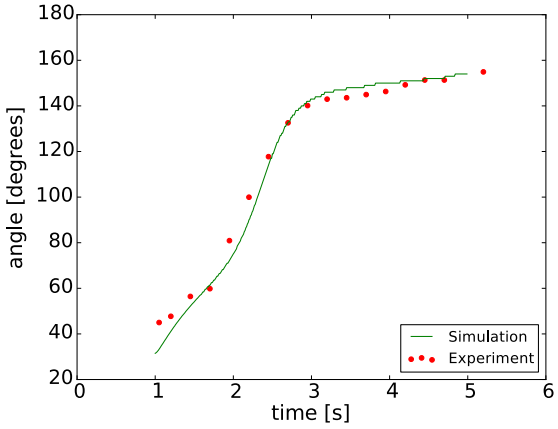

Figure 9.5: Angle of rotation of the particles as a function of time in experiment (red) and simulation (green). [BFL+13]

Category/Name	Symbol	Unit	Value
Domain and Discretization			
Length	l_{Γ_s}	m	$8.4 \cdot 10^{-3}$
Grid Size	h	m	$2.1 \cdot 10^{-5}$
Time Step Size	Δ t	s	$1.0 \cdot 10^{-2}$
Fluid (Water 25°C)			
Density	ρ	kg/m^3	$1.0 \cdot 10^{+3}$
Dynamic Viscosity	η	Pa $\cdot$ s	$1.0 \cdot 10^{-3}$
Maximum Velocity	$\boldsymbol{v}_{\max}$	m/s	$2.0 \cdot 10^{-3}$
Square Particle			
Length	l_S	m	$1.0 \cdot 10^{-4}$
Density	ρ_S	kg/m^3	$2.0 \cdot 10^{+3}$
Center of Mass	c_S	m	$(8.6, 2.8)^T \cdot 10^{-4}$
Velocity	$\boldsymbol{v}_S$	m/s	$(-1.8, -3.5)^T \cdot 10^{-4}$
Angle of Rotation	Θ_S	rad	2.0
Angular Velocity	$\boldsymbol{\omega}_S$	rad/s	0.0
L-Shaped Particle			
Length	l_L	m	$2.3 \cdot 10^{-4}$
Density	ρ_L	kg/m^3	$2.0 \cdot 10^{+3}$
Center of Mass	c_L	m	$(4.0, 2.3)^T \cdot 10^{-4}$
Velocity	$\boldsymbol{v}_L$	m/s	$(-1.3, -4.4)^T \cdot 10^{-4}$
Angle of Rotation	Θ_L	rad	5.3
Angular Velocity	$\boldsymbol{\omega}_L$	rad/s	0.0

Table 9.1: Domain, discretization, fluid and particle related constants and parameters for simulations validating the quadrupolar force density.

Category/Name	Symbol	Unit	Value
Domain and Discretization			
Length	l_{Γ_s}	m	2.0
Grid Size	h	m	$1.1 \cdot 10^{-2}$
Time Step Size	Δ t	s	$1.0 \cdot 10^{-2}$
Fluid (Water 25°C)			
Density	ρ	kg/m^3	$1.0 \cdot 10^{+3}$
Dynamic Viscosity	η	Pa $\cdot$ s	$1.0 \cdot 10^{-3}$
Maximum Velocity	$\boldsymbol{v}_{\max}$	m/s	$9.1 \cdot 10^{-1}$
L-Shaped Enantiomers			
Length	$l_{L_{L/R}}$	m	$1.2 \cdot 10^{-1}$
Density	$\rho_{L_{L/R}}$	kg/m^3	$2.0 \cdot 10^{+3}$
Center of Mass			
Figure 9.6	$c_{L_{L/R}}$	m	$(-0.5, -6.0)^T \cdot 10^{-1}$
Figure 9.7	$c_{L_{L/R}}$	m	$(0.0, -0.7)^T$
Velocity	$\boldsymbol{v}_{L_{L/R}}$	ms	$(0.0, 0.0)^T$
Angle of Rotation	$\Theta_{L_{L/R}}$	rad	0.0
Angular Velocity	$\boldsymbol{\omega}_{L_{L/R}}$	rad/s	0.0

Table 9.2: Domain, discretization, fluid and particle related constants and parameters for simulations showing enantiomer separation using the quadrupolar force density.

lines. Furthermore, the enantiomers are separated at the center when the particles are placed in the center of the incoming vorticity stream, as shown in Figure 9.7. In both cases the L-shaped enantiomers follow streamlines to the experimentally predicted vortex, see [Kon08]. The finite element immersed boundary method shows comparable results for slightly deformable L-shaped enantiomers [FHLBM15].

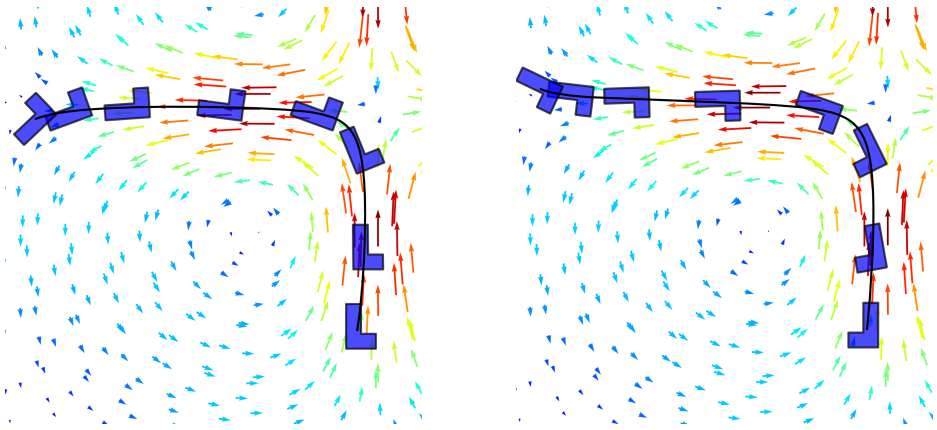

Figure 9.6: Enantiomer separation of a right-handed (left) and left-handed (right) L-shaped enantiomer at the outgoing velocity streamlines. The right-handed L-shaped particle follows the vortex rotating counterclockwise in the lower left quadrant whereas the left-handed L-shaped particle follows the vortex rotating clockwise in the upper left quadrant. [BFL$^+$13]

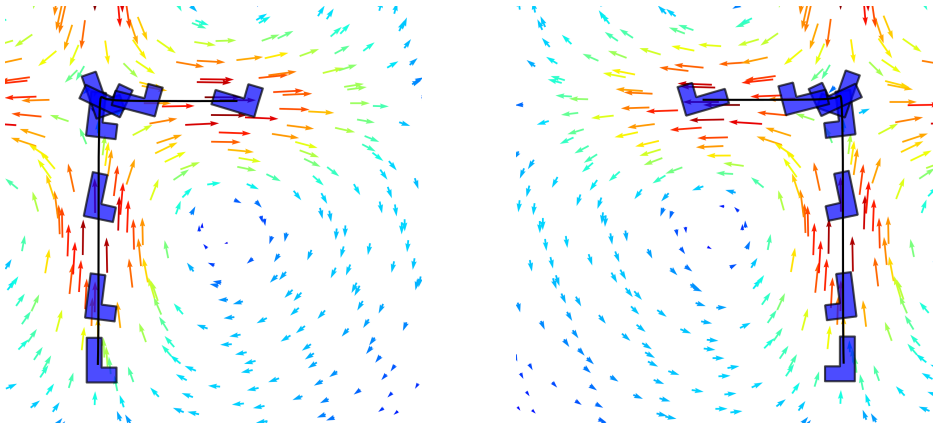

Figure 9.7: Enantiomer separation of a right-handed (left) and left-handed (right) L-shaped enantiomer at the central streamlines. The right-handed L-shaped particle follows the vortex rotating counterclockwise in the upper right quadrant whereas the left-handed L-shaped particle follows the vortex rotating clockwise in the upper left quadrant. [BFL$^+$13]

Chapter 10

Conclusion and Outlook

In the beginning of this second part we presented a model for surface acoustic wave-generated fluid flow in three-dimensional domains. The validated implementation of this model shows good qualitative agreement to experimental data even for the simulation of a setup with reduced spatial dimensions. Using these numerical results we further showed that the vorticity pattern occurring at the top of the water bulk is not divergence-free at the center of the vortices which was not yet possible to measure in experiments but conjectured. The implemented version of the code is able to take advantage of parallel systems with large amounts of physical memory. This allows us to simulate complete setups in the near future and to compare the simulations with experimental data also in a quantitative manner.

Regarding enantiomer separation we implemented a fictitious domain Lagrange multiplier method to simulate the motion of rigid bodies in two-dimensional fluids. The mentioned non-divergence free velocity fields obtained in experiment and simulation forced us to look for alternatives. Thus, we decided to use the quadrupolar force density proposed by [KSTH06] which resembles an idealized surface acoustic wave-generated vorticity pattern on top of the water bulk. For the former, enantiomer separation was predicted from a theoretical point of view. Indeed, we found possible settings for enantiomer separation of L-shaped particles which confirms the theoretically predicted separation for simple chiral particles in [KSTH06]. Furthermore, we were able to reproduce in simulation specific properties of particle propagation observed in experiments [Kon08], in particular we showed left- and right-handed L-shaped objects to be attracted by vortices rotating clockwise and counterclockwise, respectively. However, enantiomer separation has not been reproduced in experiments with the previously described setup so far [Bur13]. Here, numerical simulations may help to find possible conditions for enantiomer separation which would considerably reduce the number of necessary experiments. For example, from the current point of view, it is not clear whether an optimal ratio of the particle size

to the vortex size exists for which separation takes place. In this context we also have to consider refined force densities with respect to the experimental vorticity pattern. Finally, a detailed understanding of the current experimental setup is an essential step towards enantiomer separation on a molecular level relevant in industrial applications.

Bibliography

[ABCM02] D. Arnold, F. Brezzi, B. Cockburn, and L. Marini, *Unified analysis of discontinuous Galerkin methods for elliptic problems*, SIAM Journal on Numerical Analysis **39** (2002), no. 5, 1749–1779.

[AFS68] J. H. Argyris, I. Fried, and D. W. Scharpf, *The TUBA family of plate elements for the matrix displacement method*, Aero. J. Roy. Aero. Soc. **72** (1968), 701–709.

[AGH+08] H. Antil, A. Gantner, R. H. W. Hoppe, D. Köster, K. Siebert, and A. Wixforth, *Modeling and simulation of piezoelectrically agitated acoustic streaming on microfluidic biochips*, Domain Decomposition Methods in Science and Engineering XVII (U. Langer, M. Discacciati, D. E. Keyes, O. B. Widlund, and W. Zulehner, eds.), Lecture Notes in Computational Science and Engineering, vol. 60, Springer Berlin Heidelberg, 2008, pp. 305–312.

[AGH+10] H. Antil, R. Glowinski, R. H. W. Hoppe, C. Linsenmann, T.-W. Pan, and A. Wixforth, *Modeling, simulation, and optimization of surface acoustic wave driven microfluidic biochips*, Journal of Computational Mathematics **28** (2010), no. 2, 149–169.

[ALG+05] D. Aarts, H. N. Lekkerkerker, H. Guo, G. H. Wegdam, and D. Bonn, *Hydrodynamics of droplet coalescence*, PRL **95** (2005), 164503.

[AO00] M. Ainsworth and J. T. Oden, *A posteriori error estimation in finite element analysis*, Wiley, Chichester, 2000.

[ASM+92] M. I. Angelova, S. Soléau, P. Méléard, F. Faucon, and P. Bothorel, *Preparation of giant vesicles by external AC electric fields. Kinetics and applications*, Trends in Colloid and Interface Science VI (C. Helm, M. Lösche, and H. Möhwald, eds.), Progress in Colloid and Polymer Science, vol. 89, Springer Berlin / Heidelberg, 1992, pp. 127–131.

[Bak77] G. Baker, *Finite element methods for elliptic equations using nonconforming elements*, Math. Comp. **31** (1977), 45–89.

[BBe06] K.W. Busch and M.A. Busch (eds.), *Chiral analysis*, Elsevier, Amsterdam, 2006.

[BEG07] A. Bertozzi, S. Esedoglu, and A. Gillette, *Inpainting of binary images using the Cahn–Hilliard equation*, IEEE Trans. Image Process. **16** (2007), 285–291.

[Bes03] K. Bester, *Chiral analysis for environmental applications*, Analytical and Bioanalytical Chemistry **376** (2003), no. 3, 302–304.

[BF91] F. Brezzi and M. Fortin, *Mixed and hybrid finite element methods*, Springer, Berlin-Heidelberg-New York, 1991.

[BFH+15] S. Burger, T. Fraunholz, R. H. W. Hoppe, A. Wixforth, M. A. Peter, and T. Franke, *Numerical simulation of surface acoustic wave actuated separation of rigid enantiomers by the fictitious domain Lagrange multiplier method*, Comput. Meth. Appl. Math. (2015), in press.

[BFL+13] S. Burger, T. Fraunholz, C. Leirer, R. H. W. Hoppe, A. Wixforth, M. A. Peter, and T. Franke, *Comparative study of the dynamics of lipid membrane phase decomposition in experiment and simulation*, Langmuir **29** (2013), no. 25, 7565–7570.

[BFS65] F. K. Bogner, R. L. Fox, and L. A. Schmit, *The generation of interelement compatible stiffness and mass matrices by the use of interpolation formulas*, Proceedings Conference on Matrix Methods in Structural Mechanics (1965), 397–444.

[BG00] L. A. Bagatolli and E. Gratton, *Two photon fluorescence microscopy of coexisting lipid domains in giant unilamellar vesicles of binary phospholipid mixtures*, Biophysical Journal **78** (2000), no. 1, 290–305.

[BGS10] S. C. Brenner, T. Gudi, and L. Sung, *An a posteriori error estimator for a quadratic C^0-interior penalty method for the biharmonic problem*, IMA Journal of Numerical Analysis **30** (2010), no. 3, 777–798.

[BH95] W. L. Briggs and V. H. Henson, *The DFT*, SIAM, Philadelphia, 1995.

[BHW03a] T. Baumgart, S. Hess, and W. Webb, *Imaging coexisting fluid domains in biomembrane models coupling curvature and line tension*, Nature **425** (2003), 821–824.

[BHW03b] T. Baumgart, S. T. Hess, and W. W. Webb, *Imaging coexisting fluid domains in biomembrane models coupling curvature and line tension*, Nature **425** (2003), 821–824.

[BMVBT13] S. Baoukina, E. Mendez-Villuendas, W. F. D. Bennett, and D. P. Tieleman, *Computer simulations of the phase separation in model membranes*, Faraday Discussions **161** (2013), 63–75.

[BN10] A. Bonito and R. H. Nochetto, *Quasi-optimal convergence rate of an adaptive discontinuous Galerkin method*, SIAM Journal on Numerical Analysis **48** (2010), no. 2, 734–771.

[BP05] L. Bartkowiak and I. Pawlow, *The Cahn–Hilliard–Gurtin system coupled with elasticity*, Control and Cybernetics **34** (2005), 1005–1043.

[BR03] W. Bangerth and R. Rannacher, *Adaptive finite element methods for differential equations*, Lectures in Mathematics, ETH-Zürich, Birkhäuser, Basel, 2003.

[Bra96] C. E. Bradley, *Acoustic streaming field structure: The influence of the radiator*, J. Acoust. Soc. Am. **100** (1996), no. 3, 1399–1408.

[BS01] I. Babuška and T. Strouboulis, *The finite element method and its reliability*, Clarendon Press, Oxford, 2001.

[BS05] S. C. Brenner and L. Sung, *C^0 interior penalty methods for fourth order elliptic boundary value problems on polygonal domains*, Journal of Scientific Computing **22-23** (2005), no. 1-3, 83–118.

[BS08] S. C. Brenner and L. R. Scott, *The mathematical theory of finite element methods.*, Springer, 2008.

[Bur13] S. Burger, *Separation von Mikropartikeln unterschiedlicher Geometrie in 2-Dim Flussfeldern*, Master's thesis, University of Augsburg, 2013.

[BZ73] I. Babuška and M. Zlámal, *Nonconforming elements in the finite element method with penalty*, SIAM Journal on Numerical Analysis **10** (1973), no. 5, pp. 863–875.

[Cah59] J. W. Cahn, *Free energy of a nonuniform system. II. Thermodynamic basis*, Journal of Chemical Physics **30** (1959), 1121–1124.

[Cah61] ———, *On spinodal decomposition*, Acta Met. **9** (1961), 795–801.

[CFGK12] E. Campillo-Funollet, G. Grün, and F. Klingbeil, *On modeling and simulation of electrokinetic phenomena in two-phase flow with general mass densities*, SIAM Journal on Applied Mathematics **72** (2012), no. 6, 1899–1925.

[CH58] J. W. Cahn and J. E. Hilliard, *Free energy of a nonuniform system. I. Interfacial free energy*, J. Chem. Phys **28** (1958), 258–267.

[CH06] C. Carstensen and R. H. W. Hoppe, *Convergence analysis of an adaptive nonconforming finite element method*, Numerische Mathematik **103** (2006), no. 2, 251–266.

[Che02] L. Q. Chen, *Phase-field models for microstructural evolution*, Ann. Rev. Mater. Res. **32** (2002), 113–140.

[Cho97] A. J. Chorin, *A numerical method for solving incompressible viscous flow problems*, Journal of Computational Physics **135** (1997), no. 2, 118–125.

[CHSW11] C. Carstensen, R. H. W. Hoppe, N. Sharma, and T. Warburton, *Adaptive hybridized interior penalty discontinuous Galerkin methods for H(curl)-elliptic problems*, Numer. Math. Theor. Meth. Appl. **4** (2011), 13–37.

[CKNS08] J. M. Cascon, C. Kreuzer, R. H. Nochetto, and K. G. Siebert, *Quasi-optimal rate of convergence of adaptive finite element methods*, SIAM Journal on Numerical Analysis **46** (2008), 2524–2550.

[CSCe93] A. N. Collins, G. N. Sheldrake, and J. Crosby (eds.), *Chirality in industry: The commercial manufacture and applications of optically active compounds*, Wiley, Chichester, 1993.

[CSCe98] ———, *Chirality in industry II: The commercial manufacture and applications of optically active compunds*, Wiley, Chichester, 1998.

[DBV+01] C. Dietrich, L. A. Bagatolli, Z. N. Volovyk, N. L. Thompson, M. Levi, K. Jacobson, and E. Gratton, *Lipid rafts reconstituted in model membranes*, Biophysical Journal **80** (2001), 1417–1428.

[DJDPS79] J. Douglas Jr., T. Dupont, P. Percell, and R. Scott, *A family of C^1 finite elements with optimal approximation properties for various Galerkin methods for 2nd and 4th order problems*, R.A.I.R.O. Model. Math. Anal. (1979), no. 13, 227–255.

[DLP02] J. P. Deans, H. Li, and M. J. Polyak, *CD20-mediated apoptosis: Signalling through lipid rafts*, Immunology **107** (2002), 176 – 182.

[Dör96] W. Dörfler, *A convergent adaptive algorithm for Poisson's equation*, SIAM Journal on Numerical Analysis **33** (1996), no. 3, 1106–1124.

[Edi03] M. Edidin, *The state of lipid rafts: From model membranes to cells.*, Annual review of biophysics and biomolecular structure **32** (2003), 257–283.

[EEHJ95] K. Eriksson, D. Estep, P. Hansbo, and C. Johnson, *Computational differential equations*, Cambridge University Press, Cambridge, 1995.

[EF89] C. M. Elliott and D. A. French, *A non-conforming finite element method for the two-dimensional Cahn–Hilliard equation*, SIAM Journal on Numerical Analysis **26** (1989), no. 4, 884–903.

[EFG+07] C. Eck, M. Fontelos, G. Grün, F. Klingbeil, and O. Vantzos, *A phase field model in electrowetting and related phenomena*, PAMM **7** (2007), no. 1, 1151205–1151206.

[EG96] C. M. Elliott and H. Garcke, *On the Cahn–Hilliard equation with degenerate mobility*, SIAM Journal on Numerical Analysis **27** (1996), 404–423.

[EGH+02] G. Engel, K. Garikipati, T. J. R. Hughes, M. G. Larson, L. Mazzei, and R. L. Taylor, *Continuous/discontinuous finite element approximations of fourth-order elliptic problems in structural and continuum mechanics with applications to thin beams and plates, and strain gradient elasticity*, Computer Methods in Applied Mechanics and Engineering **191** (2002), no. 34, 3669–3750.

[Ell89] C. M. Elliot, *The Cahn–Hilliard model for the kinetics of phase separation*, Mathematical Models for Phase Change Problems (J.F. Rodrigues, ed.), International Series on Numerical Mathematics, vol. 88, Birkhauser Publishing, New York, 1989.

[EZ86] C. M. Elliott and S. Zheng, *On the Cahn–Hilliard equation*, Archive for Rational Mechanics and Analysis **96** (1986), no. 4, 339–357.

[FGJ11] M. Fontelos, G. Grün, and S. Jörres, *On a phase-field model for electrowetting and other electrokinetic phenomena*, SIAM Journal on Mathematical Analysis **43** (2011), no. 1, 527–563.

[FHH10] J. Fan, T. Han, and M. Haataja, *Hydrodynamic effects on spinodal decomposition kinetics in planar lipid bilayer membranes*, The Journal of Chemical Physics **133** (2010), 235101.

[FHL+11] T. Franke, R. H. W. Hoppe, C. Linsenmann, L. Schmid, C. Willbold, and A. Wixforth, *Numerical simulation of the motion of red blood cells and vesicles in microfluidic flows*, Computing and Visualization in Science **14** (2011), no. 4, 167–180.

[FHLBM15] T. Franke, R. H. W. Hoppe, C. Linsenmann, and K. Beleke-Maxwell, *Numerical simulation of surface acoustic wave actuated enantiomer separation by the finite element immersed boundary method*, Computers and Fluids **112** (2015), 50–60.

[FHLW11] T. Franke, R. H. W. Hoppe, C. Linsenmann, and A. Wixforth, *Projection based model reduction for optimal design of the time-dependent Stokes system*, International Series of Numerical Mathematics **160** (2011), 61–84.

[FHP14] T. Fraunholz, R. H. W. Hoppe, and M. A. Peter, *Convergence analysis of an adaptive interior penalty discontinuous Galerkin method for the biharmonic problem*, Journal of Numerical Mathematics (2014), in press.

[FLe06] E. Francotte and W. Lindner (eds.), *Chirality in drug research*, Wiley-VCH, Weinheim, 2006.

[FOL04] A. Filippov, G. Orädd, and G. Lindblom, *Lipid lateral diffusion in ordered and disordered phases in raft mixtures*, Biophysical Journal **86** (2004), 891–896.

[For05] L. Foret, *A simple mechanism of raft formation in two-component fluid membranes*, Europhysics Letters **71** (2005), no. 3, 508.

[Fro07] T. Frommelt, *Mischen und Sortieren mit SAW-Fluidik in Simulation und Experiment*, Ph.d. thesis, University of Augsburg, 2007.

[Gar03] H. Garcke, *On Cahn–Hilliard systems with elasticity*, Proc. Roy. Soc. Edinburgh Sect. A **133** (2003), 307–331.

[Gar05] H. Garcke, *On a Cahn–Hilliard model for phase separation with elastic misfit*, Annales de l'Institut Henri Poincaré Analyse non linéaire **22** (2005), 165–185.

[GH09] E. H. Georgoulis and P. Houston, *Discontinuous Galerkin methods for the biharmonic problem*, IMA Journal of Numerical Analysis **29** (2009), 573–594.

[GHK+07] A. Gantner, R. H. W. Hoppe, D. Köster, K. Siebert, and A. Wixforth, *Numerical simulation of piezoelectrically agitated surface acoustic waves on microfluidic biochips*, Computing and Visualization in Science **10** (2007), no. 3, 145 – 161.

[GHV11] E. H. Georgoulis, P. Houston, and J. Virtanen, *An a posteriori error indicator for discontinuous Galerkin approximations of fourth order elliptic problems*, IMA Journal of Numerical Analysis **31** (2011), 281–298.

[GLT89] R. Glowinski and P. Le Tallec, *Augmented lagrangian and operator-splitting methods in nonlinear mechanics*, Society for Industrial and Applied Mathematics, 1989.

[GPH+01] R. Glowinski, T.-W. Pan, T.I. Hesla, D.D. Joseph, and J. Périaux, *A fictitious domain approach to the direct numerical simulation of incompressible viscous flow past moving rigid bodies: Application to particulate flow*, Journal of Computational Physics **169** (2001), no. 2, 363–426.

[GPHJ99] R. Glowinski, T.-W. Pan, T. I. Hesla, and D. D. Joseph, *A distributed Lagrange multiplier/fictitious domain method for particulate flows*, International Journal of Multiphase Flow **25** (1999), 755–794.

[GPP94] R. Glowinski, T.-W. Pan, and J. Periaux, *A fictitious domain method for Dirichlet problem and applications*, Computer Methods in Applied Mechanics and Engineering **111** (1994), 283–303.

[GPP98] ———, *Distributed Lagrange multiplier methods for incompressible viscous flow around moving rigid bodies*, Comp. Methods Appl. Mech. Engrg. **151** (1998), 181–194.

[Gui63] A. Guinier, *X-ray diffraction: In crystals, imperfect crystals, and amorphous bodies*, W. H. Freeman and Co., 1963.

[GW05] H. Garcke and U. Weikard, *Numerical approximation of the Cahn–Larché equation*, Numerische Matehmatik **100** (2005), 639–662.

[Hac14] S. Hachfeld, *Numerische Simulation von Enantiomer Separation*, Master's thesis, University of Augsburg, 2014.

[Hel67] K. Hellen, *Analysis of elastic plates in flexure by a simplified finite element method*, Tech. Report C146, Acta Polytechnica Scandinavica, Civil Engineering Series, 1967.

[Hen12] A. Henderson, *The ParaView guide: A parallel visualization application*, Kitware Inc., 2012.

[Her67] L. Herrmann, *Finite element bending analysis for plates*, J. of Mech., Div. ASCE, a3, EM 5 93 (1967), 49–83.

[HH77] P. C. Hohenberg and B. I. Halperin, *Theory of dynamic critical phenomena*, Rev. Mod. Phys. **49** (1977), 435–479.

[HKW09] R. H. W. Hoppe, G. Kanschat, and T. Warburton, *Convergence analysis of an adaptive interior penalty discontinuous Galerkin method*, SIAM Journal on Numerical Analysis **47** (2009), 534–550.

[HL12] R. H. W. Hoppe and C. Linsenmann, *An adaptive Newton continuation strategy for the fully implicit finite element immersed boundary method*, Journal of Computational Physics **231** (2012), no. 14, 4676–4693.

[HSW04] P. Houston, D. Schötzau, and T. P. Wihler, *Mixed hp-discontinuous Galerkin finite element methods for the Stokes problem in polygons*, Numerical Mathematics and Advanced Applications (M. Feistauer, V. Dolejší, P. Knobloch, and K. Najzar, eds.), Springer Berlin Heidelberg, 2004, pp. 493–501.

[HSW07] P. Houston, D. Schötzau, and T. Wihler, *Energy norm a posteriori error estimation of hp-adaptive discontinuous Galerkin methods for elliptic problems*, Math. Models Methods Appl. Sci. **17** (2007), 33–62.

[Hun07] J. D. Hunter, *Matplotlib: A 2D graphics environment*, Computing In Science & Engineering **9** (2007), no. 3, 90–95.

[Hym52] M. A. Hyman, *Non-iterative numerical solution of boundary-value problems*, Applied Scientific Research, Section B **2** (1952), no. 1, 325–351.

[JM95] K. Jørgensen and O. G. Mouritsen, *Phase separation dynamics and lateral organization of two-component lipid membranes*, Biophysical Journal **95** (1995), 942–954.

[JMA07] K. Jacobson, O. G. Mouritsen, and R. G. W. Anderson, *Lipid rafts: At a crossroad between cell biology and physics*, Nature Cell Biology **9** (2007), no. 1, 7–14.

[Joh73] C. Johnson, *On the convergence of a mixed finite-element method for plate bending problems*, Numer. Math. **21** (1973), 43–62.

[KG07] N. Kapur and P. Gaskell, *Morphology and dynamics of droplet coalescence on a surface*, Phys. Rev. E **75** (2007), 056315.

[KL96] R. Kam and H. Levine, *Phase-field model of spiral dendritic growth*, Phys. Rev. E **54** (1996), no. 3, 2797–2801.

[KL00] P. Krüger and M. Lösche, *Molecular chirality and domain shapes in lipid monolayers on aqueous surfaces*, Phys. Rev. E **62** (2000), no. 5, 7031–7043.

[KMe98] N. Kurihara and J. Miyamoto (eds.), *Chirality in agrochemicals*, Wiley, 1998.

[Kon08] M. Konrad, *Trennung chiraler Objekte in Mikroströmung*, Ph.d. thesis, University of Augsburg, 2008.

[Kös06] D. Köster, *Numerical simulation of acoustic streaming on SAW-driven biochips*, Ph.d. thesis, University of Augsburg, 2006.

[Kös07] ———, *Numerical simulation of acoustic streaming on surface acoustic wave-driven biochips*, SIAM Journal on Scientific Computing **29** (2007), no. 6, 2352–2380.

[KP07] O. Karakashian and F. Pascal, *Convergence of adaptive discontinuous Galerkin approximations of second-order elliptic problems*, SIAM Journal on Numerical Analysis **45** (2007), 641–665.

[KS99] G. E. Karniadakis and S. J. Sherwin, *Spectral/hp methods for cfd*, Oxford University Press, 1999.

[KS06] N. Kahya and P. Schwille, *Fluorescence correlation studies of lipid domains in model membranes (review)*, Molecular Membrane Biology **23** (2006), 29–39.

[KSA06] S. Komura, N. Shimokawa, and D. Andelman, *Tension-induced morphological transition in mixed lipid bilayers*, Langmuir **22** (2006), 6771–6774.

[KSB+03] N. Kahya, D. Scherfeld, K. Bacia, B. Poolman, and P. Schwille, *Probing lipid mobility of raft-exhibiting model membranes by fluorescence correlation spectroscopy*, The Journal of Biological Chemistry **278** (2003), 28109–28115.

[KSTH06] M. Kostur, M. Schindler, P. Talkner, and P. Hänggi, *Chiral separation in microflows*, Phys. Rev. Lett. **96** (2006), 014502.

[Lei08] C. T. Leirer, *Dynamik und Struktur in der Phasenkoexistenz von Lipidmembranen*, Ph.d. thesis, University of Augsburg, 2008.

[Li06] P. C. H. Li, *Microfluidic lab-on-a-chip for chemical and biological analysis and discovery*, CRC Press, 2006.

[Lin14] F. Linder, *Simulation von akustisch angeregten Strömungen auf parallelen Systemen*, Master's thesis, University of Augsburg, 2014.

[LLJ98] P. H. Leo, J. S. Lowengrub, and H. J. Jou, *A diffuse interface model for microstructural evolution in elastically stressed solids*, Acta Materialia **46** (1998), 2113–2130.

[LMWea12] A. Logg, K.-A. Mardal, and G. N. Wells et al., *Automated solution of differential equations by the finite element method: The FEniCS book*, Springer, 2012.

[Mar90] G. I. Marchuk, *Splitting and alternating direction methods. Handbook of numerical analysis, vol. 1 (P. G. Ciarlet and J. L. Lions; eds.)*, 1990, pp. 197–462.

[Mir00] A. Miranville, *Some generalizations of Cahn–Hilliard equation*, Asymptotic Analysis **22** (2000), 235–259.

[Mir01] ———, *Long-time behavior of some models of Cahn–Hilliard equations in deformable continua*, Nonlinear Analysis: Real World Applications **2** (2001), 273–304.

[MM88] H. M. McConnell and V. T. Moy, *Shapes of finite two-dimensional lipid domains*, Journal of Physical Chemistry **92** (1988), 4520–4525.

[Möh95] H. Möhwald, *Phospholipid monolayers*, Handbook of Biological Physics, Lipowsky, R and Sackmann, E, 1995.

[Moi11] L. Moisan, *Periodic plus smooth image decomposition*, Journal of Mathematical Imaging and Vision **39** (2011), 161–179.

[MP96] S. Maier-Paape, *The Cahn–Hilliard equation: Lecture script*, Universität Augsburg, 1996.

[MRMDN01] A. Menchaca-Rocha, A. Martinez-Davalos, and R. Nunez, *Coalescence of liquid drops by surface tension*, Phys. Rev. E **63** (2001), 046309.

[MV97] M. A. Mayer and T. K. Vanderlick, *Monte Carlo simulation of the shapes of domains in phospholipid monolayers*, Physical Review E **55** (1997), no. 1, 1106–1119.

[MW84] H. M. McConnell and R. M. Weis, *Two-dimensional chiral crystals of phospholipid*, Nature **310** (1984), 47–49.

[NC98] A. Novick-Cohen, *The Cahn–Hilliard equation: Mathematical and modeling perspectives*, Adv. Math. Sci. Appl. **8** (1998), no. 2, 965–985.

[NR04] P. Neittaanmäki and S. Repin, *Reliable methods for mathematical modelling. error control and a posteriori estimates*, Elsevier, New York, 2004.

[Oli07] Travis E. Oliphant, *Python for scientific computing*, Computing in Science and Engineering **9** (2007), no. 3, 10–20.

[OWL05] G. Orädd, P. W. Westerman, and G. Lindblom, *Lateral diffusion coefficients of separate lipid species in a ternary raft-forming bilayer: A Pfg-NMR multinuclear study*, Biophysical Journal **89** (2005), no. 1, 315–320.

[Pes77] C. S. Peskin, *Numerical analysis of blood flow in the heart*, Journal of Computational Physics **25** (1977), no. 3, 220–252.

[Pik03] L. J. Pike, *Lipid rafts: Bringing order to chaos*, J. Lipid Res **44** (2003), 655–667.

[PJG05] T.-W. Pan, D. D. Joseph, and R. Glowinski, *Simulating the dynamics of fluid-ellipsoid interactions*, Comput. Struct. **83** (2005), no. 6-7, 463–478.

[PZ08a] I. Pawlow and W. M. Zajaczkowski, *Global regular solutions to Cahn–Hilliard system coupled with viscoelasticity*, Math. Meth. Appl. Sci. **32** (2008), 2197–2242.

[PZ08b] ———, *Strong solvability of 3D Cahn–Hilliard system in elastic solids*, Math. Meth. in the Appl. Sci. **31** (2008), 879–914.

[Ray85] J. W. S Rayleigh, *On waves propagated along the plane surface of an elastic solid*, Proceedings of the London Mathematical Society **17** (1885), no. 1, 4–11.

[Rei13] L. Reischmann, *Numerische Simulation und Vergleich verschiedener Modelle für fluide Entmischungsprozesse in Lipidmembranen*, Master's thesis, University of Augsburg, 2013.

[RFPS09] M. Rigol, H. C. Fu, T. R. Powers, and R. Stocker, *Separation of microscale chiral objects by shear flow*, Phys. Rev. Lett. **102** (2009), 158103.

[RH73] W. H. Reed and T. R. Hill, *Triangular mesh methods for the neutron transport equation*, Technical Report LA-UR-73-479, Los Alamos Scientific Laboratory, 1973.

[RKG05] S. Rozovsky, Y. Kaizuka, and J. T. Groves, *Formation and spatio-temporal evolution of periodic structures in lipid bilayers*, J Am Chem Soc **127** (2005), 36–37.

[RW82] J.S. Rowlinson and B. Widom, *Molecular theory of capillarity*, Clarendon Press, Oxford, UK, 1982.

[Sau63] V. K. Saul'ev, *On solving boundary value problems with high performance computers by a fictitious domain method*, Sib. Math. J. **4** (1963), 912–925.

[Scr08] G. K. E. V. Scriba, *Cyclodextrins in capillary electrophoresis enantioseparations — recent developments and applications*, Journal of Separation Science **31** (2008), no. 11, 1991–2011.

[SI97] K. Simons and E. Ikonen, *Functional rafts in cell membranes*, Nature **387** (1997), 569–572.

[SMC01] A. V. Samsonov, I. Mihalyov, and F. C. Cohen, *Characterization of cholesterol-sphingomyelin domains and their dynamics in bilayer membranes*, Biophys. J. **81** (2001), 1486–1500.

[Ste09] M. Stepanova, *Reversible formation of nanodomains in monolayers of DPPC studied by kinetic modeling*, Biophysical Journal **96** (2009), 4896–4905.

[Tar07] L. Tartar, *Introduction to Sobolev spaces and interpolation theory*, Springer, Berlin-Heidelberg-New York, 2007.

[Tem68] R. Temam, *Une méthode d'approximation de la solution des équations de Navier-Stokes*, Bulletin de la Société Mathématique de France **96** (1968), 115–152.

[TPEMJ03] B. A. Tsui-Pierchala, M. Encinas, J. Milbrandt, and E. M Johnson, *Lipid rafts in neuronal signaling and function*, Trends in neurosciences **25** (2003), 412 – 417.

[Tre03] S. Tremaine, *On the origin of irregular structure in Saturn's rings*, Astronomical Journal **125** (2003), 894–901.

[Ver96] R. Verfürth, *A review of a posteriori estimation and adaptive mesh-refinement techniques*, Wiley-Teubner, New York, Stuttgart, 1996.

[Vis69] W. Visser, *A refined mixed type plate bending element*, A.I.A.A. Journal **7** (1969), no. 9, 1801–1803.

[VK02] S. L. Veatch and S. L. Keller, *Organization in lipid membranes containing cholesterol*, Phys. Rev. Lett. **89** (2002), 268101.

[VK03] ———, *Separation of liquid phases in giant vesicles of ternary mixtures of phospholipids and cholesterol*, Biophysical Journal **85** (2003), 3074–3083.

[VK05] ———, *Seeing spots: Complex phase behavior in simple membranes*, Biochimica et Biophysica Acta **1746** (2005), 172–185.

[vRdB91] G. van Rossum and J. de Boer, *Interactively testing remote servers using the Python programming language*, CWI Quarterly **4** (1991), 283–303.

[Wel09] C. J. Welch, *Microscale chiral HPLC in support of pharmaceutical process research*, Chirality **21** (2009), no. 1, 114–118.

[Wen07] T. J. Wenzel, *Discrimination of chiral compounds using NMR spectroscopy*, Wiley, Chichester, 2007.

[WGM04] G. N. Wells, K. Garikipati, and L. Molari, *A discontinuous Galerkin formulation for a strain gradient dependent damage model*, Comput. Methods Appl. Mech. Eng. **193** (2004), 3633–3645.

[WKG06] G. N. Wells, E. Kuhl, and K. Garikipati, *A discontinuous Galerkin method for the Cahn–Hilliard equation*, Journal of Computational Physics **218** (2006), no. 2, 860–877.

[WM85] R. M. Weis and H. M. McConnell, *Cholesterol stabilizes the crystal-liquid interface in phospholipid monolayers*, The Journal of Physical Chemistry **89** (1985), no. 21, 4453–4459.

[WPXG09] T. Wang, T.-W. Pan, Z. W. Xing, and R. Glowinski, *Numerical simulation of rheology of red blood cell rouleaux in microchannels*, Phys. Rev. E **79** (2009), 041916.

[WV65] R. M. White and F. W. Voltmer, *Direct piezoelectric coupling to surface electric waves*, Applied Physics Letters **7** (1965), 314–316.

Curriculum Vitae

Personal Information

Name	Thomas Fraunholz
Address	Universität Augsburg – Institut für Mathematik – Universitätsstr. 14 86159 Augsburg Germany

Publications

[1] T. Fraunholz, R. H. W. Hoppe, and M. A. Peter. *Convergence analysis of an adaptive interior penalty discontinuous Galerkin method for the biharmonic problem.* Journal of Numerical Mathematics 2014, in press

[2] D. Braess, T. Fraunholz, and R. H. W. Hoppe. *An equilibrated a posteriori error estimator for the interior penalty discontinuous Galerkin method.* SIAM Journal on Numerical Analysis **52** (2014), 2121–2136.

[3] S. Burger, T. Fraunholz, C. Leirer, R. H. W. Hoppe, A.Wixforth, M. A. Peter, and T. Franke. *Comparative study of the dynamics of lipid membrane phase decomposition in experiment and simulation.* Langmuir **29** (2013), no. 25, 7565–7570.

[4] S. Burger, T. Fraunholz, R. H. W. Hoppe, A. Wixforth, M. A. Peter, and T. Franke. *Numerical simulation of surface acoustic wave actuated separation of rigid enantiomers by the fictitious domain Lagrange multiplier method.* Comput. Meth. Appl. Math. 2015, in press